

**Three-dimensional finite-element modelling
of the influence of erosion and sediment deposition
on the slip behaviour of faults**

Von der Naturwissenschaftlichen Fakultät der
Gottfried Wilhelm Leibniz Universität Hannover
zur Erlangung des Grades

Doktorin der Naturwissenschaften

Dr. rer. nat.

genehmigte Dissertation

von

M.Sc. Heidi Anneli Turpeinen

geboren am 10.02.1978 in Vantaa (Finnland)

2013

Referentin: Prof. Dr. Andrea Hampel

Korreferent: Prof. Dr. Ulrich Heimhofer

Tag der Promotion: 2.10.2013

Abstract

The landscape on the Earth's surface has been continuously modified, which is obvious from evolving topography. Both mass redistribution on the surface due to erosion and sedimentation as well as tectonic deformation contribute to landscape evolution. To investigate the potential feedbacks between tectonics and surface processes in different tectonic settings, the experiments for this thesis are computed by using a subroutine called CASQUS that calculates and links the surface processes with a three-dimensional finite element model including discrete planar faults constructed with Abaqus Finite Element Analysis (FEA). Both the landscape evolution tool and the geomechanical model are fully coupled throughout the model run up to millions of years of model time. The series of experiments starts with an extensional tectonic regime considering a single normal fault and is then extended to arrays of normal faults. To investigate the impact of surface processes alone, the regional extension is stopped after a certain amount of model time but surface processes remain active. Finally, the interaction between surface processes and the evolution of blind thrust faults in a regime experiencing shortening is investigated. Experiments on model runs with different parameters such as diffusive hillslope processes, fluvial erosion as well as fault length indicate that surface processes affect the fault slip evolution in extensional regions where a fault reaches the surface. The amount of additional fault slip, erosion and sedimentation vary for different parameters, whereas the diffusion constant as well as fault length and dip have the strongest impact on the fault slip and subsequent landscape evolution. Thus the faults accumulate up to 200 m more displacement if erosion and sedimentation are applied on the model surface. The erosion and sedimentation rates both vary between 30 and 80 m/Ma. When the far-field extension ceases, surface processes may lead to prolonged fault slip of up to several million years. The additional fault slip after cessation of regional extension reaches up to 160 m. A correlation between fault slip evolution, mass redistribution and differential stress is also observed. Irrespectively of the depth of the fault top edge applied in this study, blind thrusts are not affected by surface processes but the propagation of hidden faults lead to formation of growth folds on the model surface which, in turn, is subject to surface processes. This study provides an insight into the feedback mechanisms between surface processes and tectonics in different tectonic settings. The findings contribute to better understanding of spatial and temporal distribution of tectonic activity with respect to surface processes. In addition, the findings contribute to the research of hazards generated by mass redistribution on the Earth's surface.

Keywords: *numerical modelling, landscape evolution, fault slip evolution*

Zusammenfassung

Die sich kontinuierlich entwickelnde Erdoberfläche wird beeinflusst sowohl von Massenumlagerung, d.h. Erosion und Sedimentation, als auch durch tektonische Verformung. Um mögliche Rückkopplungsmechanismen zwischen tektonischer Aktivität und Oberflächenprozessen in unterschiedlichen tektonischen Regimes zu untersuchen, werden die Experimente in dieser Studie mit Hilfe der Software CASQUS berechnet. Diese berechnet und koppelt die Oberflächenprozesse mit einem in Abaqus Finite Element Analysis (FEA) konstruierten, drei-dimensionalen Finite - Elemente Model, welches auch planare Störungen enthält. Beide Programme sind vollständig gekoppelt während der gesamten Laufzeit der Modelle bis zu Millionen Jahre. Die Versuchsreihe beginnt mit einem Modell, in dem die Erdkruste gedehnt wird. Nach isolierten Abschiebungen werden die Versuche auf mehrere Abschiebungen erweitert. Um den tatsächlichen Einfluss von Oberflächenprozessen zu testen, wird die regionale Dehnung des Modells nach einer bestimmten Zeit gestoppt, aber Oberflächenprozesse bleiben weiterhin aktiv. Die Experimente zum Schluss untersuchen die Wechselwirkung von Oberflächenprozessen und Evolution von blinden Störungen in Regionen, in denen die Erdkruste verkürzt wird. In den Testreihen wird der Einfluss von Parametern wie diffusive Prozesse auf dem Berghang, fluviale Erosion und Störungslänge sowie Einfallswinkel untersucht. Die Ergebnisse zeigen, dass Oberflächenprozesse beeinflussen die Evolution von Störungen in Regionen, wo die Kruste gedehnt wird und die Störungen die Erdoberfläche erreichen. Die Menge der zusätzlichen Bewegung auf der Störungsfläche variiert bei unterschiedlichen Parametern, wobei sowohl diffusive Prozesse als auch Störungslänge und Einfallswinkel einen stärkeren Einfluss auf die Störung zeigen. Die Bewegung einzelner Störungen ist bis zu 200 m mehr, wenn Oberflächenprozesse aktiv sind. Die Erosions- und Sedimentationsraten variieren zwischen 30 und 80 m/Ma. Wenn die regionale Dehnung endet, können Oberflächenprozesse dazu führen, dass Störungen weiterhin über mehrere Millionen Jahre aktiv bleiben. Die Bewegung der Störungen nach dem Ende der regionalen Dehnung kann dann bis zu 160 m erreichen. Es besteht eine Korrelation zwischen der Evolution von Störungen, Massenumlagerung und Differentialspannung. Unabhängig von der Tiefe, die in dieser Studie für die Störungsoberkante verwendet werden, haben Oberflächenprozesse keinen wesentlichen Einfluss auf die Evolution von Störungen. Die Bewegung einer blinden Störung führt jedoch zur Formation von Falten an der Modelloberfläche, welche durch Oberflächenprozesse verändert wird. Diese Studie bietet einen Einblick in die Mechanismen der Wechselwirkung zwischen Oberflächenprozessen und tektonischer Aktivität unter unterschiedlichen tektonischen Bedingungen. Die Erkenntnisse leisten einen Beitrag zum besseren Verständnis der räumlichen und zeitlichen Verteilung von tektonischer Aktivität und Oberflächenprozessen. Dazu steuern die Rückschlüsse aus dieser Studie bei der Forschung von Gefahren durch Massenumlagerung an der Erdoberfläche bei.

Schlagwörter: numerische Modellierung, Evolution von Erdoberfläche, Entwicklung von Störungen

Contents

Abstract	3
Zusammenfassung	4
Contents	5
Chapter 1: Introduction	7
Chapter 2: Setup of the numerical model with full coupling between tectonics and landscape evolution	14
Chapter 3: Influence of surface processes on the behavior of normal faults after cessation of regional extension	18
3.1 Motivation	18
3.2 Model setup	19
3.3 Model results	20
3.4 Discussion.....	31
3.5 Conclusions	35
Chapter 4: Influence of surface processes on normal fault arrays	36
4.1 Motivation	36
4.2 Model setup	38
4.3 Model results	39
4.3.1 Horst bounded by 4 x 30-km-long faults.....	39
4.3.2 Horst bounded by 6 x 20-km-long faults.....	42
4.4 Discussion.....	45
4.5 Conclusions	59
Chapter 5: Blind thrusts: slip behaviour and landscape evolution	60
5.1 Motivation	60
5.2 Model setup	62

5.3 Model results	63
5.4 Discussion.....	67
5.4.1 Comparison with other studies	75
5.5 Conclusions	79
Chapter 6: Discussion	81
Chapter 7: Conclusions.....	86
Acknowledgements.....	87
References	88
Appendix99

1. Introduction

In regions undergoing active tectonics, the mass redistribution in a landscape due to surface processes affects tectonic deformation and vice versa (e.g. Molnar and England, 1990; Burbank and Pinter, 1999). In the brittle upper crust, this deformation is typically accommodated by faults. The mode of movement along fault planes is in general controlled by the tectonic setting and ultimately by the orientation of the principal stresses (e.g. Anderson, 1952; Richardson et al., 1979). For example, if the crust is extended (normal faults) or shortened (thrust/reverse faults), the maximum principal stress is vertical or horizontal, respectively. The initiation and further evolution of faults depend, among other factors, on the strength of surroundings and on the initial fault length and dip (Hardy and Finch, 2006; Burrato et al., 2012; Albrecht and Lingrey, 2012) as well as on the boundary conditions controlling the crustal deformation rate.

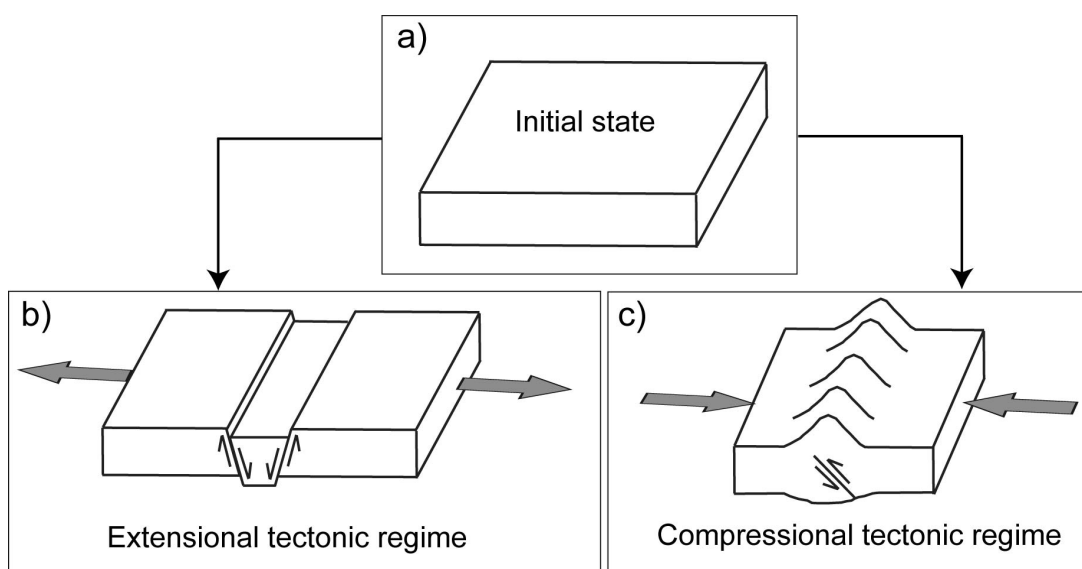


Figure 1: Simplified schematic sketch of deformation mechanisms. *a)* Initial state of the crust, *b)* an example of the deformation within an extensional tectonic regime and *c)* subsequent deformation during shortening.

Active extension or shortening of the continental crust over millions of years leads to the growth of faults and topography (Cowie and Scholz, 1992a; Dawers et al., 1993; Nicol et al., 1997; Walsh et al., 2002; Nicol et al., 2005). A simplified sketch of different crustal deformation mechanics is illustrated in Figure 1. Depending on the orientation of the faults, large-scale extension leads to formation of horst or graben structures (e.g. Eaton, 1982) (Figure 1b). In contrast, a compressional tectonic regime results in folding and local thickening of the crust (Figure 1c). A natural example of an area in an extensional setting that spans over almost 3000 km length

Chapter 1

and up to 1000 km width is the Basin-and-Range Province in the western U.S. (e.g. *Eaton, 1982; Wernicke and Snow, 1998; Ellis and Densmore, 1999; Wernicke et al., 2000; Niemi et al., 2004*). More localized crustal extension leads to the formation of rifts and graben systems, such as in the North Sea (e.g. *Gabrielsen et al., 2001*) or the Gulf of Corinth (e.g. *Briole et al., 2000; Sachpazi et al., 2003; Avallone et al., 2004; Sakellariou et al., 2007; Taylor et al., 2011*). In contrast, a prominent example of a tectonic setting experiencing crustal shortening and subsequent thrusting and folding is provided by the Himalayas (e.g. *Avouac et al., 1993; Burbank et al., 1996; de Celles et al., 2002; Long et al., 2011*). The Apennines in Italy represent another, younger fold and thrust belt, where both shortening and extension contribute to the formation of the mountain range (e.g. *Roberts and Michetti, 2004; Palumbo et al., 2004; Roberts, 2006*). An example of a normal fault in the central Apennines is shown in *Figure 2*.

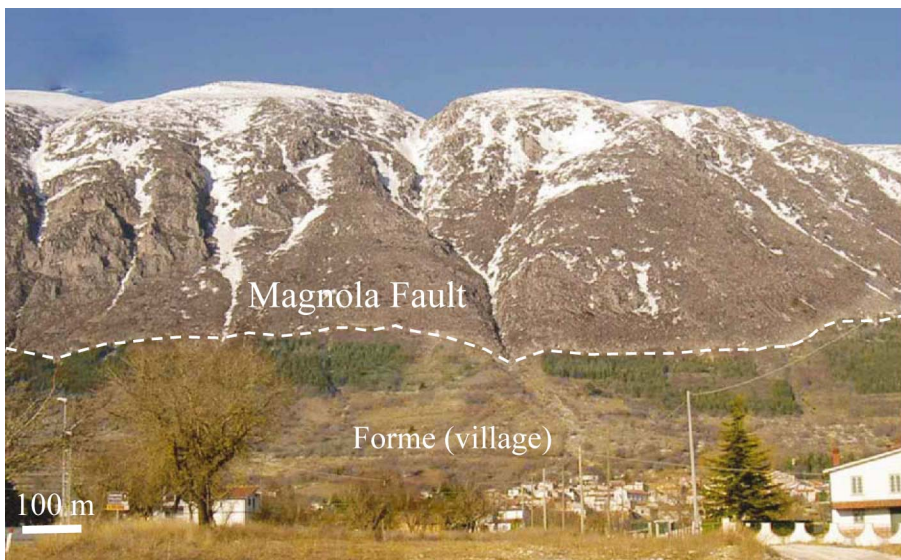


Figure 2: The Magnola fault in the Apennines, central Italy. The fault trace is marked by the dashed white line. Modified after *Palumbo et al. (2005)*.

In some regions the fault remains blind below overlying sediments (*Hardy and Finch, 2006*). However, when subjected to crustal shortening, these faults may induce a fault-propagation fold at the surface as more and more displacement is accumulated by the fault at depth (e.g. *Ellis and Densmore, 2006*). Such folds are present for instance, below the Los Angeles area (e.g. *Shaw and Suppe, 1994; Pratt et al, 2002; Dolan et al., 2003; Lin and Stein, 2006*).

The evolution of a fault-bounded topography through time is controlled by erosion and tectonically induced uplift (*Harbor, 1997; Densmore et al., 1998*). Erosion affects the Earth's surface continuously but since the erosion rate is controlled by climatic conditions and by the resistance of the exhumed material, spatial and

Chapter 1

temporal variations in both denudation and sedimentation rates are possible (*Burbank and Anderson, 2012*). Local variations in erosion rates probably due to monsoon rain are known from the Lesser Himalaya, where the erosion rate of 0.2 mm/a is significantly lower than in the Greater Himalaya, where the erosion partially occurs at rates of up to 0.8 mm/a (e.g. *Wobus et al, 2005*). Variable erosion rates of 0.5 to 1.3 mm/a, when averaged over 10'000–100'000 years, occur also in the Teflon Peaks in the western Alaska Range, where the extreme relief of up to 5 km results from different rock types with varying material resistivity (*Ward et al., 2012*).

The interaction of surface processes and tectonics has received increasing interest since the beginning of the 1990s (e.g. *Molnar and England, 1990; Burbank and Pinter, 1999; Whipple and Meade, 2006*). Besides by geological field studies (e.g. *Montgomery and Brandon, 2002; Trudgill, 2002; Densmore et al., 2004; Kirby and Whipple, 2012*), the feedback mechanisms between tectonics and surface processes have been investigated by using numerical methods (e.g. *Koons, 1989; Kooi and Beaumont, 1994; Avouac and Burov, 1996; Braun and Sambridge, 1997; Densmore et al., 1998; Ellis et al., 1999; Willett et al., 2001; Garcia-Castellanos, 2002; Fischer et al., 2004; Simpson, 2004a; Cowie et al., 2006; Pysklywec, 2006; Bishop, 2007; Burov and Toussaint, 2007; Braun et al., 2008; Tomkin, 2009; Godard and Burbank, 2011*) but also analogue modelling on different scale (e.g. *Mugnier et al., 1997; Bonnet and Crave, 2003; Malavieille and Konstantinovskaya, 2010*).

An example of the numerical experiments considering landscape evolution carried out by *Braun and Sambridge (1997)* is shown in *Figure 3*. The 100 km by 100 km wide model surface consists of 10'000 nodes, which are connected via an irregular grid. The total run time of the experiment was 1 Ma, which includes 10 000 steps of 100 a length. In each step and at each node, the removal and deposition of sediments is simulated using the CASCADE-algorithm (see *Chapter 2 of this work or Braun and Sambridge, 1997*). *Figure 3a* shows the model surface after 1000 time steps (after 100 ka). Since the grid is self-adaptive, i.e. nodes are automatically added if needed, the formation of rivers is recognisable as a denser grid. At the end of the model run after 10 000 time steps (after 1 Ma) the rivers have propagated towards the centre of the model and are more branched, which is obvious from *Figure 3b*. The topographic surface and the channel network at the end of the model run are shown in *Figure 3c*. The topographic elevation is up to 1 km and the intervals of the topographic contours are 0.2 km between 0 and 1 km. The dark areas represent a low topography, which is induced by the formation of the river network. The light areas reflect higher elevation and the black areas represent lakes.

Another example of a numerical model is provided by *Willett et al. (2001)*, who used a surface process model modified after *Braun and Sambridge (1997)*. The numerical

Chapter 1

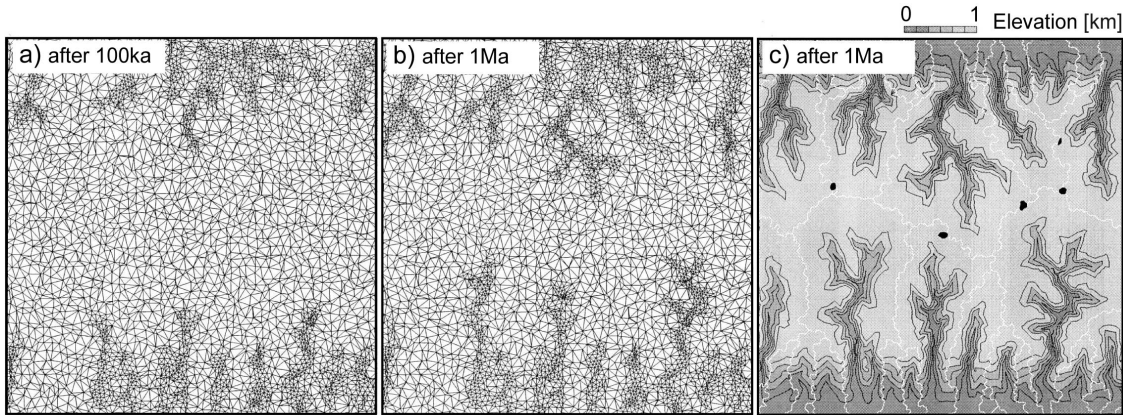
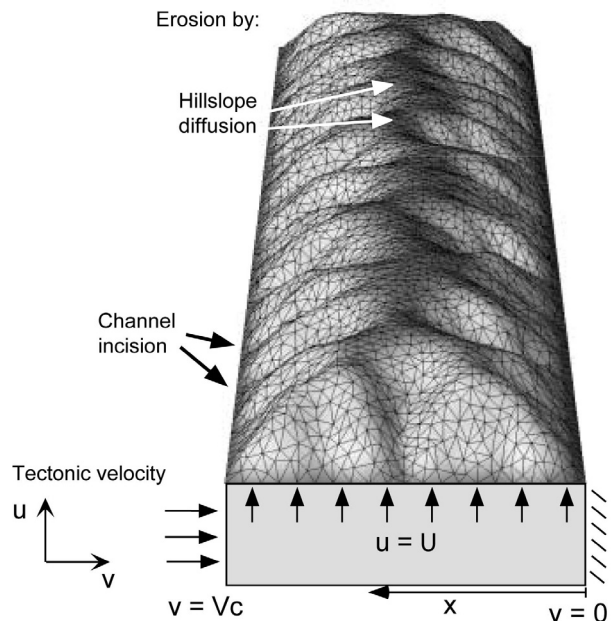


Figure 3: The landscape evolution model by *Braun and Sambridge (1997)*. *a)* Model surface with the irregular grid after 100 ka of model time. *b)* After 1 Ma the river network is more evolved, which is indicated by the locally denser grid. *c)* Topographic surface and the channel network after 1 Ma. The topographic contours are indicated by thin black lines and the topographic elevation is up to 1 km, whereas the intervals are 0.2 km between 0 and 1 km. The dark areas represent a low topography, the light areas reflect higher elevation. The black areas represent lakes.

models of *Willet et al. (2001)* include both tectonic uplift and horizontal velocity, whereas all surface edges are fixed at elevation. The number of elements on the irregular grid is allowed to increase as the landscape evolves. The model surface resulting from the interplay of these parameters is shown in *Figure 4*. The convergence velocity V_c is applied on one side only and decreases to zero on the opposite side. The uplifted topography is eroded by diffusive hillslope processes on elevated areas as well as channel incision on the river beds.

Figure 4: Model by *Willet et al. (2001)* which contains both tectonic and erosive components. The model edges remain at a fixed elevation. The shortening is limited to the left side only and the velocity (V_c) may vary between zero and the actual convergence velocity, depending on the setting used in different experiments. Note the irregular grid on the surface. Erosion affects the uplifted surface via diffusive hillslope processes and the river beds are subjected to channel incision (modified after *Willet et al., 2001*).



Chapter 1

The investigations on surface displacement through time as well as the interaction between surface processes and tectonics indicate that when numerical modelling is combined with algorithms considering the effect of surface processes on a large amount of surface nodes ($> 10'000$), the resulting topography and drainage network generated by the synthetic models significantly resembles to that of natural landscapes. A comparison is shown in *Figure 5* which illustrates the contour plot of topography on a numerical model of *Braun and Sambridge (1997)* (a) as well as a natural example showing the Snowy Mountains in Australia (b). In both figures, the river branching and general distribution of streams show similar behaviour.

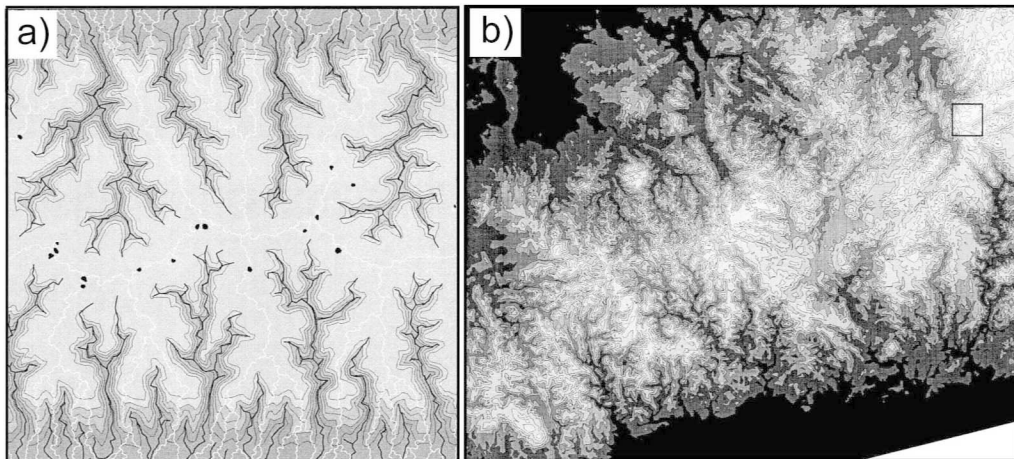


Figure 5: Comparison of a numerical model with a natural example (*modified after Braun and Sambridge, 1997*). Contour maps of a) a numerical model and b) the Snowy Mountains in south-eastern Australia. The rectangle in b) shows the location of the Mount Kosciusko (2230 m).

The landscape evolution models introduced above include tectonics only as very simplified boundary conditions and do not consider the presence of faults. Numerical models with more evolved implemented tectonics, some adjusted to specific natural landscapes, are provided for example by *Cowie et al. (2006)*, *Fischer (2006)*; *Braun et al. (2008)*, *Petit et al., (2009)*, *Tomkin (2009)*, *Upton et al. (2009)* and *Koons et al. (2010)*. *Fischer (2006)* used the finite-element method to investigate the effect of rheological parameters on the surface deformation in the Aegian-Anatolian region. The model setup included different boundary conditions as well as layers with varying material properties determined by seismological studies. Surface processes were not included in this model, since it was not within the scope of the study. *Upton et al. (2009)* used three-dimensional mechanical models to investigate the behaviour of compressive wedges. Erosion was implemented as a mass removing boundary condition, which was varied spatially and temporally. One of the first attempts to couple tectonic models with models implementing surface processes was established by *Cowie et al. (2006)*, who investigated the response of surface process to fault

Chapter 1

interaction. In their study, the tectonic model represents a two-dimensional Earth's surface, which is affected by faults throughout the model run. The surface processes did not affect the tectonic evolution but the results from the tectonic model were afterwards coupled with the results from a model simulating the surface processes (*CASCADE* by Braun and Sambridge, 1997). Hence, it was a one-way coupled model (cf. Cowie et al., 2006).

Analysis of the feedback between surface processes and tectonics using fully coupled three-dimensional finite-element models including discrete faults, erosion and sediment deposition was first introduced by Maniatis et al. (2009). In their study a three-dimensional tectonic model including one or more faults (e.g. Maniatis and Hampel, 2008; Hampel et al., 2009) was created by using the commercial finite-element software Abaqus FEA (Dassault Systèmes Simulia Corp.; Hibbit et al., 2008). This model was fully coupled to the landscape evolution model *CASCADE* (Braun and Sambridge, 1997) by the software tool *CASQUS* (Kurfeß, 2008; Kurfeß and Heidbach, 2009).

The model results showed that erosion and sedimentation may lead to increased fault slip rate by affecting the fault displacement at depth (Maniatis et al., 2009). The experiments revealed, that surface processes lead to up to ~15 % higher slip rates, for both isolated faults and fault arrays, when compared with model runs carried out without surface processes. The parameter study shows that the intensity of surface processes is primarily controlled by the fault length, dip and the resulting displacement rate as well as the diffusion constant controlling diffusive hillslope processes. The impact of the fluvial erosion constant, that comprises the stream erosion and the precipitation rate, on the fault slip accumulation is rather small when compared to the effect of other parameters (Maniatis et al., 2009).

The key issue of this thesis was to investigate the impact of surface processes on the fault slip evolution and the resulting topography in settings including one or more faults. Another aim was to study the potential ability of surface processes to prolong faulting even after the far-field tectonic boundary conditions have ceased. Also the distribution of fault displacement within an array as well as the feedback between interacting neighbouring faults was investigated. The finite element technique using the fully coupled models adopted by Maniatis et al. (2009) is applied to all experiments used for this thesis. The parameters varied depend on the model setup and include for example different fault length and dip as well as variable parameters controlling the surface processes. The basic model setup and the modelling technique are described in detail in *Chapter 2*. *Chapter 3* comprises the results from the first set of experiments with single normal faults. The experiments were used to investigate the potential interaction of fault slip accumulation and surface processes after cessation of regional extension. *Chapter 4* describes the effect of surface processes

Chapter 1

on fault arrays. In different experiments, the arrays consist of 4 or 6 normal faults. Besides the effect of the position of a fault in an array on the fault slip evolution of each fault, the feedback between individual faults was investigated. Also the effect of cessation of extension on fault arrays was studied. The last model setup described in *Chapter 5* considers blind thrust faults, where the depth of the fault top edge below the model surface is varied. Afterwards, the results from all experiments in this thesis are discussed in *Chapter 6*.

2. Setup of the numerical model with full coupling between tectonics and landscape evolution

The three-dimensional models are constructed with the commercial finite-element software Abaqus FEA version 6.9.3 and higher (*Dassault Systèmes, 2009-2012*). The models consist of a 15-km-thick and up to 200 x 200-km-wide elastic upper crust (*Fig. 6*). Depending on the experiment, a single planar fault or an array of faults is embedded in the centre of the model. Both fault dip and length are varied in different model runs. Gravity is included as a body force in the Casqus cell and as a load in the rest of the model. To account for isostasy, a lithostatic pressure (3.97×10^8 Pa) and an elastic foundation are applied to the bottom of the model, which is free to move vertically. The property of the elastic foundation represents a lower crust with a density of 2900 kg/m^3 . The model domain is meshed using two different types of elements. The uppermost up to 2 km-thick cell (*Fig. 6*), which represents the CASQUS layer (see below), is meshed by a grid of hexahedral elements with an edge length of ~ 1 km. To ensure that the river network will not follow preferred directions, an irregular mesh is induced by randomly shifting the surface nodes of the original Abaqus mesh horizontally and vertically, whereas the amounts vary in different model setups. The remaining model is meshed using tetrahedral elements, whose edge length increases from 1 km at 1 or 2 km depth to 5-6 km at 15 km depth, depending on the model setup used in the experiments.

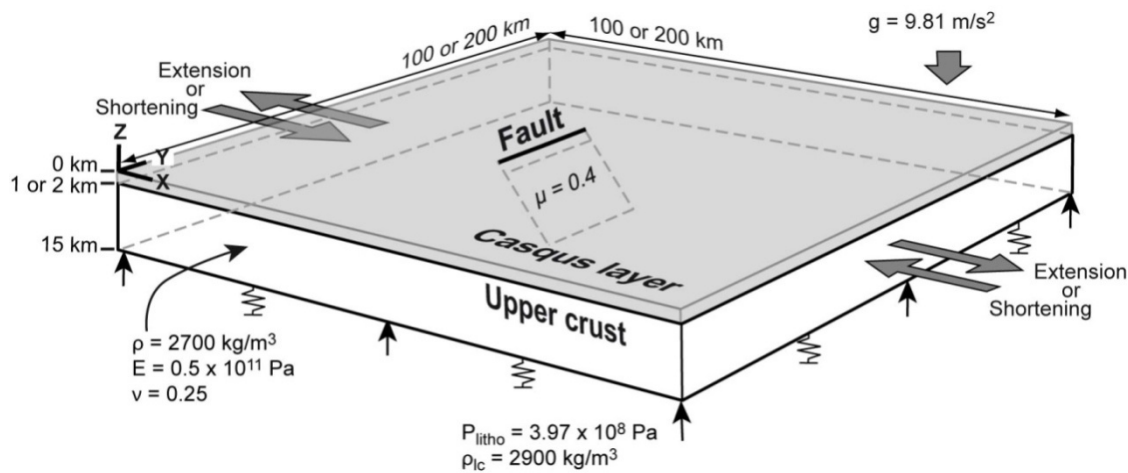


Figure 6: The basic model setup in the present study. The three-dimensional finite-element model consists of an upper crust with one or more faults in the centre. The uppermost 1- 2 km (depending on the experiment) of the model are defined as the Casqus layer that may be affected by erosion and sediment deposition. Parameters are E = Young's modulus, P_{litho} = lithostatic pressure, ρ = density, ν = Poisson's ratio, μ = friction coefficient, and g = gravitational acceleration. An elastic foundation and a lithostatic pressure applied to the model bottom account for isostasy.

Chapter 2

After establishment of isostatic equilibrium at the beginning of each model run, the model domain is extended or shortened at a total rate of 4 mm/a by applying velocity boundary conditions to the fault-parallel model sides in the yz -plane (Fig. 6). The model sides in the xz -plane are fixed in the y -direction. Slip initiation is controlled by the Mohr-Coulomb failure criterion $\tau = c + \mu\sigma_n$, where τ is the shear stress, c cohesion, μ friction coefficient and σ_n normal stress. In the experiments of the present study the friction coefficient μ is set at 0.4 and the cohesion is zero (e.g. Twiss and Moores, 1992). The slip rate of the fault is not prescribed but evolves freely as a result of the applied extension or shortening rate.

Modelling methods

To include surface processes into the model, the software CASQUS (Kurfeß, 2008; Kurfeß and Heidbach, 2009) is used to link the three-dimensional Abaqus model with the landscape evolution model CASCADE (Braun and Sambridge, 1997) by an Abaqus user subroutine. The principle of CASQUS is illustrated in Figure 7. The model surface is divided into a mesh of elements and nodes. The surface nodes along the model boundaries (some marked by stars) are fixed. These nodes are not affected by surface processes but their elevation is controlled by tectonics via Abaqus. The remaining surface nodes (examples are indicated by black dots) on the adaptive mesh domain are affected by both tectonics and surface processes due to CASQUS and Abaqus, respectively. The vertical movement of the surface nodes resulting from mass redistribution (CASCADE) and tectonics (Abaqus) is also shown. Therefore, the net vertical movement resulting from erosion and sedimentation lead to subsequent surface node uplift or subsidence.

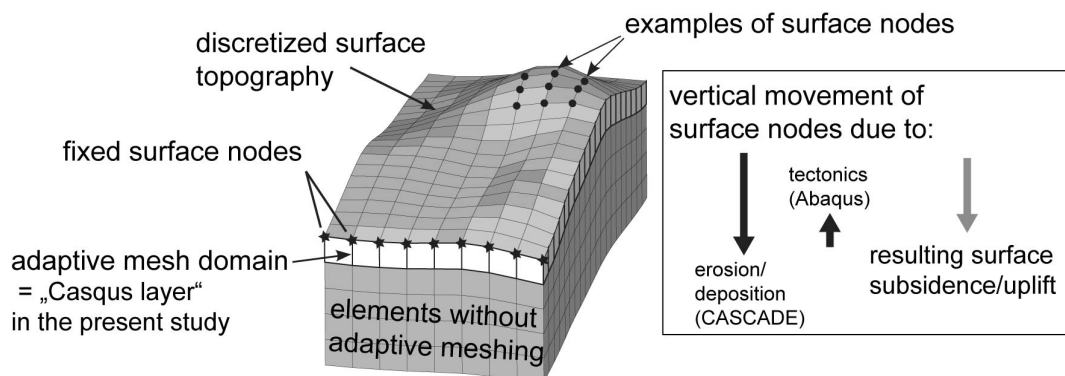


Figure 7: Sketch illustrating the principle of CASQUS Finite Element model (modified after Kurfeß, 2008; Kurfeß and Heidbach, 2009). The fixed surface nodes along the model boundaries (marked by stars) are not affected by surface processes but their elevation is controlled by tectonics via Abaqus. The rest of the surface nodes (examples marked by black dots) on the adaptive mesh domain are affected by the interaction of CASQUS and Abaqus. The net vertical movement of the surface nodes resulting from mass redistribution (CASCADE) and tectonics (Abaqus) result in uplift or subsidence of the surface nodes.

Chapter 2

At the model boundaries, sediments may leave the model domain. To ensure that only changes in volume and mass of the affiliated elements but no arbitrary stress changes occur during the shift of the surface nodes, an Arbitrary Lagrangian-Eulerian approach and adaptive meshing are used in the CASQUS layer. Hence, both the motion (Lagrangian) and the interrelation of the surface nodes (Eulerian) are introduced by adaptive meshing in the resulting new elevation. As the topographic changes induced by erosion and sedimentation are associated with a redistribution of mass on the model surface, they are able to affect the stress field in the model and subsequently the slip on the fault. Therefore, the models used in this thesis are fully coupled.

CASQUS includes diffusive hillslope processes as well as fluvial erosion and deposition. The former is implemented by the linear diffusion equation, in which the temporal change in elevation of a point is proportional to the second spatial derivative of topography (*Kooi and Beaumont, 1994; Braun and Sambridge, 1997*):

$$\partial h / \partial t = k_D \nabla^2 h \quad (1)$$

where h is elevation, t time and k_D the diffusion constant. Equation (1) describes the cumulative effect of different types of surface processes such as slope wash, rain splash and soil creep. The temporal change in elevation at a point on the model surface caused by fluvial erosion, transport and deposition is calculated by the relationship

$$\partial h / \partial t = -1/l_f (q_{f,eqb} - q_f) \quad (2)$$

Where q_f is the sediment flux of a river, $q_{f,eqb}$ the sediment transport capacity and l_f the erosion/deposition length scale. The latter is an empirical constant that describes how fast the river locally tends towards equilibrium due to erosion or deposition of sediments. Erosion occurs for $q_f < q_{f,eqb}$ and deposition for $q_f > q_{f,eqb}$. The fluvial model is transport-limited, i.e. q_f cannot exceed $q_{f,eqb}$ (*Braun and Sambridge, 1997*). The sediment transport capacity $q_{f,eqb}$ is calculated by

$$q_{f,eqb} = -K_f q_r dh/dl \quad (3)$$

where K_f is a non-dimensional empirical transport coefficient and q_r the fluvial discharge, which depends on the catchment area and the precipitation rate p , and the slope dh/dl in the direction of river drainage. The parameter $K_f \cdot p$ ultimately controls fluvial erosion in the model and is included by CASQUS.

The overview of the interaction between CASCADE and Abaqus via CASQUS is shown in *Figure 8*. During each model run, the ongoing tectonic deformation changes the elevation of the Abaqus model surface. To couple the spatial and temporal variations in both Abaqus models and CASQUS, a data exchange takes place every 10 ka, since this synchronization interval shows relatively uniform long-term model behaviour (*Kurfeß, 2008; Kurfeß and Heidbach, 2009*). At that point, the change in elevation resulting from mass redistribution at each surface node is calculated by CASQUS and transmitted to Abaqus, which then shifts the surface

Chapter 2

nodes to their new elevation. In a summary, the workflow comprises calculation of steps that are responsible for the surface processes alternating with steps during which the tectonic response to surface processes is computed. This procedure is repeated during the model run until the desired model time is completed, which in this thesis is extended to millions of years.

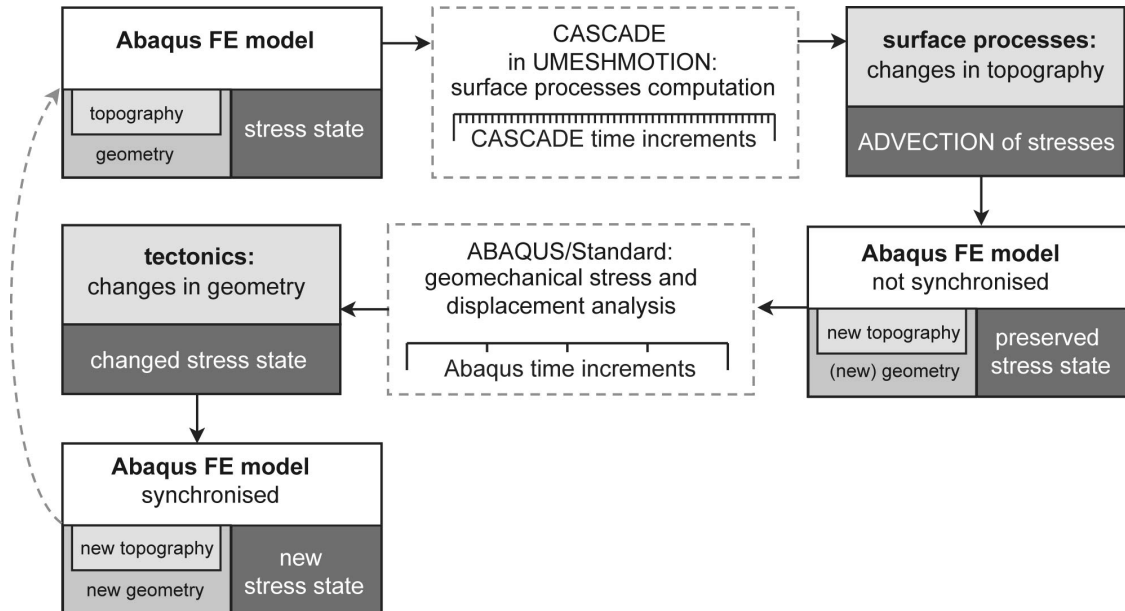


Figure 8: Workflow of the CASQUS routine that couples Abaqus Finite Element (FE) models with the landscape evolution tool CASCADE (flow of information modified from Kurfeß, 2008; Kurfeß and Heidbach, 2009). The two steps for calculation are indicated by dashed grey frames. In the first step, the change in elevation is calculated by CASCADE for each node and transmitted to Abaqus, where surface nodes are subsequently shifted to their new elevation. This leads to changes in topography. In the second step, the subsequent changes in the stress state as well as in the geometry of the model are computed. As soon as these changes are transmitted to Abaqus, the geometry of the FE model is affected by tectonics.

3. Influence of surface processes on the behaviour of normal faults after cessation of regional extension (modified after Turpeinen et al., submitted to Geomorphology)

3.1 Motivation

Accumulation of fault displacement on timescales of up to millions of years leads to the growth of normal faults in regions where the crust undergoes extensional deformation (*Cowie and Scholz, 1992a; Dawers et al., 1993; Nicol et al., 1997; Walsh et al., 2002; Nicol et al., 2005*). Continental regions experiencing active large-scale extension generate variable topography over wide areas. Some prominent examples include the Basin-and-Range Province in the western U.S. (*e.g. Eaton, 1982; Wernicke and Snow, 1998; Wernicke et al., 2000; Niemi et al., 2004*) and the Aegean region in the back-arc of the Hellenic subduction zone (*Lister et al., 1984; Lee and Lister, 1992; Gautier and Brun, 1994; Jackson, 1994*). In addition, the formation of rifts and graben systems is induced by more localized extension of the continental crust. This is the case for example in the East African Rift System (*e.g. Bosworth et al., 1992; Morley et al., 1992; Hendrie et al., 1994; Bosworth and Strecker, 1997*), in the North Sea (*e.g. Ziegler, 1983; Gabrielsen et al., 2001*) and in the Rhine Graben (*e.g. Ziegler and Dèzes, 2005*).

Geological field studies and theoretical considerations show that the growth of faults can be described by a fundamental scaling law. The fault scaling law comprises the maximum displacement D_{\max} on a fault and the fault length L by using the relationship $D_{\max} = \gamma \cdot L$ (*Cowie and Scholz, 1992a,b,c; Dawers et al. 1993; Mansfield and Cartwright 1996; Schlische et al., 1996*). The shear strength of the rock defines the constant γ which is high for strong rocks and low for weaker rocks. Hence, the ratio of D_{\max} to L is higher for faults transecting through rocks of higher strength. The fault scaling law also implies that when an isolated fault is embedded in a rock with a uniform value of γ , a constant ratio of D_{\max} to L should be maintained as the fault grows (*Cowie and Scholz 1992a,b,c; Dawers et al. 1993*). This ratio is claimed to remain constant in a fault-bounded topography during fault slip accumulation when erosive forces do not affect the Earth's surface (*Cowie and Roberts, 2001; Densmore et al., 2004; Hetzel et al., 2004*).

The growth of mountain ranges on the footwall of active fault systems is induced by slip accumulation on normal faults (*King and Ellis, 1990; Anders et al., 1993; Ellis et al., 1999; Densmore et al., 2004*). After the fault displacement is induced the maximum elevation along the elongate mountain range is obtained near the centre of the range and decreases along-strike towards the fault tips. This reflects the typical along-strike distribution of fault slip of the normal fault (*Cowie and Roberts, 2001*;

Chapter 3

Densmore et al., 2004). The further evolution of a normal fault-bounded topography through time depends on the intensity of tectonically induced uplift and erosion (*Harbor, 1997; Densmore et al., 1998*).

The Basin-and-Range Province is bounded by normal faults in different stages of their evolution. For an active normal fault with a few hundred metres of displacement the catchment-wide erosion rates in the footwall determined from cosmogenic¹⁰Be concentrations range from 10 to 35 mm/ka (*Densmore et al., 2009*). Significantly higher and more variable erosion rates of 70 to 700 mm/ka were calculated for a more mature fault with a displacement of a few kilometres (*Densmore et al., 2009*). Numerical modelling of *Maniatis et al. (2009)* has shown that erosion and sedimentation may lead to increased fault slip rate by affecting the fault displacement at depth. In their study, a three-dimensional tectonic model including one or more faults (e.g. *Maniatis and Hampel, 2008; Hampel et al., 2009*) was fully coupled with a landscape evolution model (*Braun and Sambridge, 1997*) by the software tool CASQUS (*Kurfeß and Heidbach, 2009*).

Although the feedback between normal faulting and surface processes is suggested by geological field evidence and numerical modelling, it remains unknown if mass redistribution due to erosion and sediment deposition is capable to prolong faulting even after far-field extension has ceased. To investigate the interaction of fault slip accumulation and surface processes after the cessation of regional extension, finite-element modelling using the fully coupled models introduced by *Maniatis et al. (2009)* is applied. First, the model setup is described and then the results of a parameter study, in which the parameters controlling erosion and sediment deposition as well as the dip and length of the normal fault were varied.

3.2 Model setup

The model setup is identical to the one described in *Chapter 2*. The specific model setup used for single normal faults is shown in *Figure 9*, which also shows the areas where erosion and sedimentation were derived. Each model run consists of two consecutive phases. The first phase includes extension of the model until the normal fault has obtained a displacement-length ratio according to the scaling law $D = 0.03L^{1.06}$, where D is the displacement at the fault centre in metres and L the fault length in metres (*Schlische et al., 1996*). The duration of the first model phase depends on the fault slip rate and varies between 1-1.5 Ma in different experiments (*Table 3.1*). The second model phase begins with cessation of the regional extension by fixing the model sides in the yz -plane at their current position (*Figure 9*). Subsequently all models are run for another 3 Ma without far-field extension. When

Chapter 3

surface processes are applied on the model surface, erosion and sedimentation are active during the entire model run with constant diffusion and fluvial erosion coefficients.

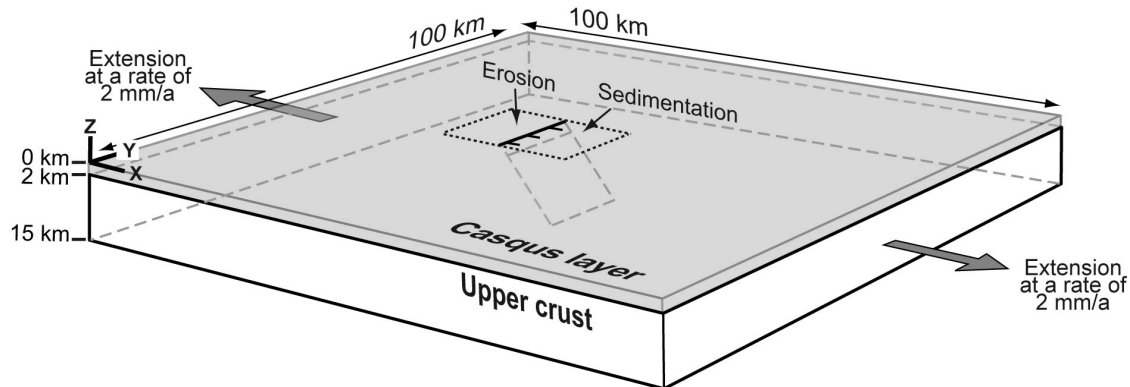


Figure 9: Perspective view of the three-dimensional finite-element model consisting of an upper crust with a normal fault in the centre. The rectangle with black dashed borders in the middle of the model surface shows the position of the areas where erosion (footwall) and sedimentation (hanging wall) were determined.

3.3 Model results

Results from experiments with and without surface processes

To show the general effect of surface processes on the fault slip evolution, a reference model containing a 60°-dipping fault of 20 km length was run with and without surface processes. When surface processes are applied, the diffusion and fluvial erosion constants are $k_D = 0.3 \text{ m}^2/\text{a}$ and $K_f \cdot p = 0.03 \text{ m/a}$, respectively, which represent commonly used intermediate values (e.g., Braun and Sambridge, 1997). The fault slip evolution for the complete model runs including both the first and the second model phase is shown in *Figure 10a*. During the first model phase, i.e. with regional extension, the fault slips at a higher rate if surface processes are active. The fault slip rate in the first model phase is 1.09 mm/a for the model run with surface processes and 1 mm/a without surface processes. This is in accordance with the findings of Maniatis et al. (2009). After cessation of extension in the model, the fault slip ceases in the absence of surface processes (*Figure 10a*). In the presence of surface processes during the model run the normal slip after the end of regional extension continues (*Figure 10a*). *Figure 10b* shows the slip evolution of the fault during the second model phase. Note that in *Figure 10b* the model time is shown relative to the time point at which the extension stops. When surface processes are active, the additional fault slip is 86 which is obtained during $\sim 1.5 \text{ Ma}$. Hence the

Chapter 3

slip rate during normal slip on the fault is 68 m/Ma. After that the slip is reversed and the rate is -5 m/Ma. The map views are generated by using GMT (*Wessel and Smith, 1998*).

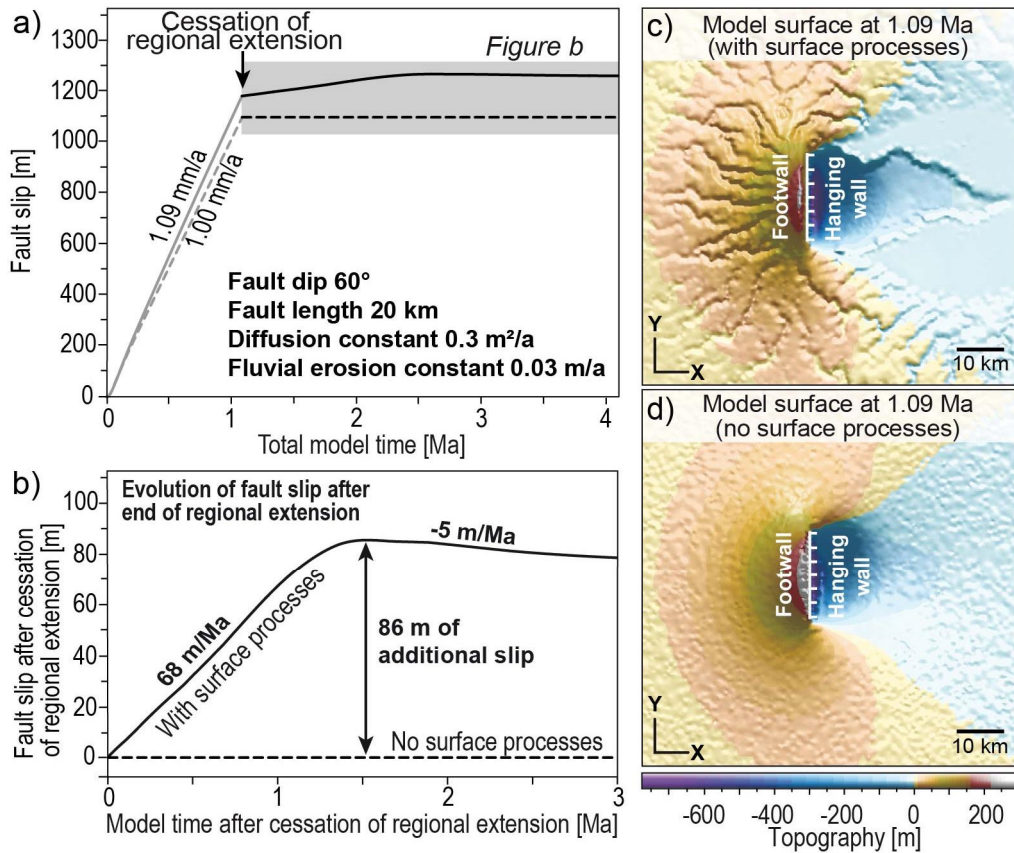


Figure 10: Results of the reference model (fault length 20 km; dip 60°) with and without surface processes. In the model run with surface processes, diffusion and fluvial erosion constants of $k_D = 0.3 \text{ m}^2/\text{a}$ and $K_f \cdot p = 0.03 \text{ m/a}$, respectively, are used. *a)* Complete fault slip evolution with and without surface processes during both first and second model phase, i.e. before and after cessation of regional extension. *b)* Additional fault slip after cessation of regional extension. Note that in this and the following figures, fault slip and model time are shown relative to the values reached at the end of regional extension to allow a direct comparison between the different experiments (see *Table 3.1* for absolute values of fault slip and slip rates). *c)* Topography on the model surface at cessation of regional extension when surface processes are active. *d)* Topography on the model surface at cessation of regional extension without surface processes. The irregular small-scale topography is an expression of the irregular grid that is required by CASQUS.

The difference between the topography of the model surface in the experiments with and without surface processes is shown in *Figure 10c* and *10d*, respectively. When the model surface is subject to erosion and sedimentation, an approximately radial drainage system is generated by the uplift of the footwall. Subsequently, sediments are transported away from the footwall and either toward the basin in the hanging wall or out of the model. Some rivers flow around the fault tips whereas others flow directly from the footwall across the fault towards the hanging wall basin

Chapter 3

(Figure 10c). The irregular small-scale topography on the model surface in Figure 10d is an expression of the artificially induced irregular grid that is required by CASQUS (for details, see Chapter 2). Note that the grid is applied to the model surface in all model runs with and without surface processes to ensure the same initial morphology. An overview of the experiments and the duration of the first model phase as well as the corresponding fault displacement are provided in Table 3.1.

Table 3.1: Overview of the experiments carried out for this study. Also shown are the length of the first model phase (with regional extension until the scaling law is fulfilled) as well as the total displacement and average slip rate of the fault at the end of the first model phase, i.e. before the extension of the model is stopped.

Fault length [km]	Fault dip [°]	Diffusion constant k_D [m²/a]	Fluvial erosion constant $K_f \cdot p$ [m/a]	Duration of first model phase [Ma]	Displacement at the end of first model phase [m]	Slip rate at the end of first model phase [mm/a]
<i>Reference model</i>						
20	60	0.3	0.03	1.09	1181	1.09
20	60	no surface processes		1.09	1094	1.00
<i>Variable diffusion constant</i>						
20	60	0.1	0.03	1.09	1139	1.05
20	60	0.5	0.03	1.09	1222	1.13
<i>Variable fluvial erosion constant</i>						
20	60	0.3	0.01	1.09	1189	1.10
20	60	0.3	0.05	1.09	1175	1.08
<i>Variable fault length</i>						
10	60	0.3	0.03	1.02	577	0.57
40	60	0.3	0.03	1.48	2438	1.66
<i>Variable fault dip</i>						
20	45	0.3	0.03	0.96	1162	1.21
20	75	0.3	0.03	1.66	1113	0.68

Results from experiments with variable diffusion constant k_D

In the first set of the parameter study the parameter controlling erosion and sedimentation, i.e. the diffusion constant k_D is varied. The length of the 60°-dipping

Chapter 3

fault is 20 km and the fluvial erosion constant $K_f \cdot p$ is set at 0.03 m/a in all model runs. *Figure 11* shows the effect of a five-fold variation in the diffusion constant, which was set to values of 0.1, 0.3 and 0.5 m²/a in different experiments. From the figure it is obvious that the fault slip accumulation during the first model phase increases with increasing diffusion constant k_D , resulting in 1.05 mm/a for the lowest k_D of 0.1 m²/a and in 1.13 mm/a for diffusion constant k_D of 0.5 m²/a (*Table 1; Figure 11a*). After cessation of regional extension the time period of normal sense of movement decreases for higher values of the constant (*Figure 11b*). In case of diffusion constant k_D of 0.1 m²/a normal faulting occurs at a relatively constant rate of 19 m/Ma during the complete time span after cessation of far-field extension. The fault slip evolution for the highest diffusion constant $k_D = 0.5$ m²/a shows a normal slip rate of 86 m/Ma until around 600 ka. The maximum fault slip accumulation until that point is 43 m. Again, the fault experiences a transition to reverse slip at a low rate of -4 m/Ma. At cessation of extension the topography of the model surface gets smoother for a higher diffusion constant (*Figure 11c*). In addition, some smaller channels disappear and the rim of the hanging wall basin tends to be straightened. If the diffusion constant is decreased, rivers and channels incise more deeply since the fluvial erosion becomes more dominant (*Figure 11d*).

Results from experiments with variable fluvial erosion constant $K_f \cdot p$

In the model runs with variable fluvial erosion constant $K_f \cdot p$ the diffusion constant k_D is 0.3 m²/a and the length of the 60°-dipping fault is 20 km. *Figure 12a* shows that a five-fold variation in the fluvial erosion constant $K_f \cdot p$ (0.01, 0.03 and 0.05 m/a) does not significantly change neither the co-extensional nor the post-extensional slip behaviour of the fault. The fault slip rate during the first model phase varies from 1.08 to 1.10 mm/a increasing with decreasing fluvial erosion constant $K_f \cdot p$. During the second model phase the transition to reverse slip occurs slightly earlier and the maximum fault displacement slightly decreases when the fluvial erosion constant $K_f \cdot p$ increases (*Figure 12b*). For the lowest fluvial erosion constant of $K_f \cdot p = 0.01$ m/a the fault slip stops for ~80 ka after obtaining the maximum displacement before the normal sense of slip is reversed to thrusting at a rate of -2m/Ma. For the highest fluvial erosion constant of 0.05 m/a, the slip rate is -4 m/Ma after transition to reverse slip. In contrast to the minor effect on the fault slip, the fluvial erosion constant strongly affects the topography on the model surface (*Figure 12c, d*). For a higher fluvial erosion constant (*Figure 12c*), the streams incise more deeply into the fault footwall, while the number of streams increases. In case of a lower fluvial erosion constant, the area of the hanging wall basin increases (*Figure 12d*).

Chapter 3

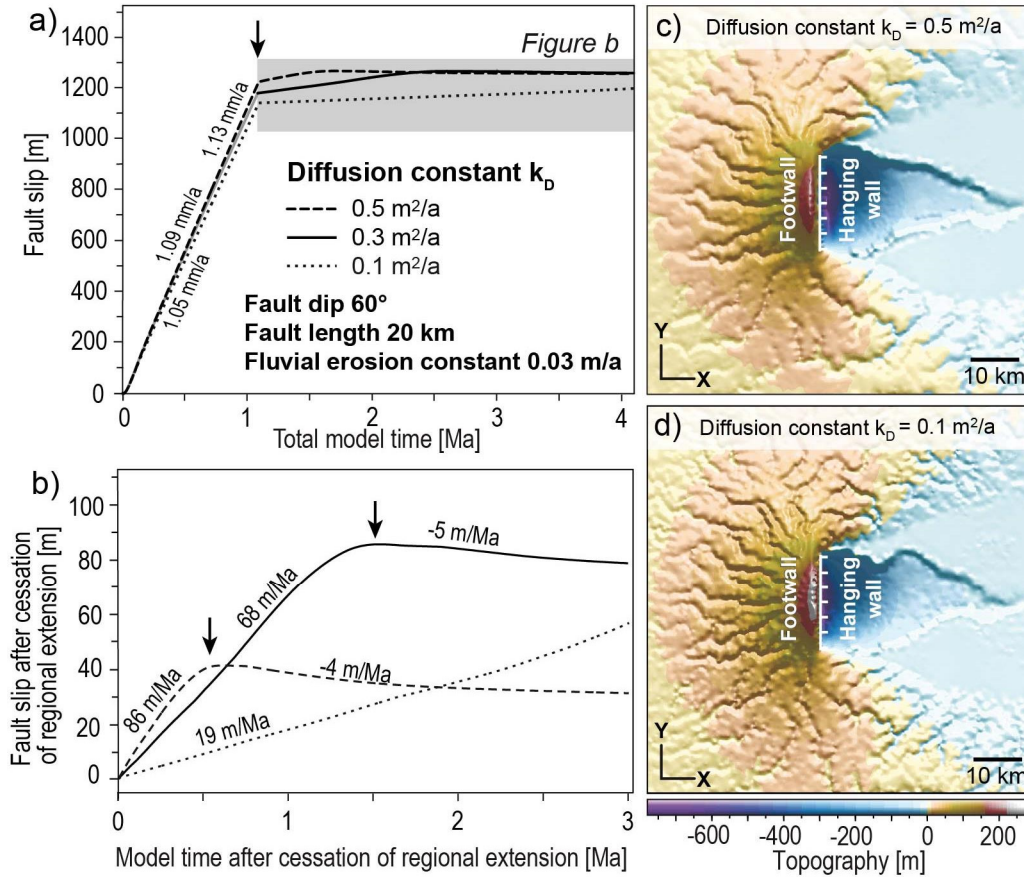


Figure 11: Results from the experiments with different diffusion constants k_D . The fault length is 20 km and the fault dips with 60° . *a)* Complete fault slip evolution. The time point of cessation of regional extension is indicated by the arrow. The line with dots corresponds to diffusion constant $k_D = 0.1 \text{ m}^2/\text{a}$, the black line represents the diffusion constant $k_D = 0.3 \text{ m}^2/\text{a}$ and the dashed curve indicates the diffusion constant $k_D = 0.5 \text{ m}^2/\text{a}$. Both the fault slip rate and the maximum fault displacement vary slightly for different parameters and are the highest for the diffusion constant $k_D = 0.5 \text{ m}^2/\text{a}$. The end of the first phase, i.e. the time point of cessation of regional extension, is indicated by the arrow. *b)* The fault slip evolution after the end of extension. In the experiment with $k_D = 0.1 \text{ m}^2/\text{a}$, the slip rate is averaged over 3 Ma. For other model runs the positive slip rates indicate normal sense of slip and average over the time between the end of regional cessation and the time point with the maximum amount of displacement. Negative slip rates indicate reverse sense of slip and average over the time between the time point with the maximum amount of displacement and the end of the model run. *c)* Topography on the model surface at cessation of regional extension for the model run with diffusion constant $k_D = 0.5 \text{ m}^2/\text{a}$. *d)* Topography on the model surface at cessation of regional extension for diffusion constant $k_D = 0.1 \text{ m}^2/\text{a}$.

Results from experiments with variable fault dip

In the third model set, the fault dip was varied while keeping the parameters controlling the surface processes constant, i.e. the diffusion constant k_D is $0.3 \text{ m}^2/\text{a}$ and the fluvial erosion constant $K_f \cdot p$ is set at 0.03 m/a . The fault length is 20 km.

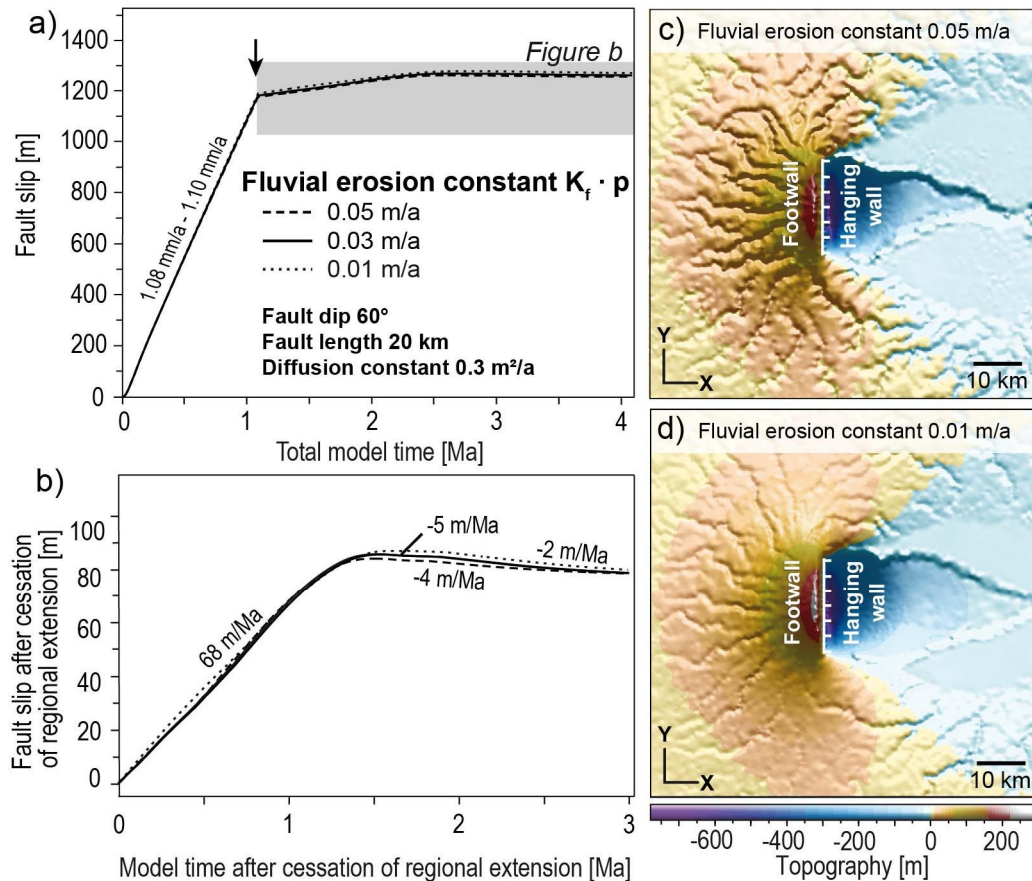


Figure 12: Results of the experiments with different fluvial erosion constants $K_f \cdot p$. The fault length is 20 km and the fault dips with 60°. *a)* Complete fault slip evolution. The time point of cessation of regional extension is indicated by the arrow. The line with dots represents the model run with $K_f \cdot p = 0.01$ m/a, the black line corresponds to $K_f \cdot p$ of 0.03 m/a and the dashed curve shows the effect of fluvial erosion constant $K_f \cdot p = 0.05$ m/a. Both the fault slip rate and the maximum fault displacement vary slightly for different parameters and are the highest for the fluvial erosion constant $K_f \cdot p = 0.01$ m/a. The end of the first phase, i.e. the time point of cessation of regional extension, is indicated by the arrow. *b)* Fault slip evolution after the end of extension. In all model runs the positive slip rates indicate normal sense of slip and average over the time between the end of regional cessation and the time point with the maximum amount of displacement. Negative slip rates indicate reverse sense of slip and average over the time between the time point with the maximum amount of displacement and the end of the model run. *c)* Topography on the model surface at cessation of regional extension for the model run with fluvial erosion constant $K_f \cdot p = 0.05$ m/a. *d)* Topography on the model surface at cessation of regional extension for fluvial erosion constant $K_f \cdot p = 0.01$ m/a.

Figure 13a indicates that the fault dip affects the fault slip rate in the first model phase. The fault slip accumulates at a rate of 1.21 mm/a for 45°-dipping fault and the rate is 0.68 mm/a for a 75°-dipping fault. Hence, for a shallower fault dip the natural maximum displacement is obtained earlier than for steeper faults. From *Figure 13b* it is obvious that the fault dip strongly affects the fault slip evolution after the cessation

Chapter 3

of far-field extension. With increasing fault dip the time period of normal slip is reduced. Hence, for a shallower fault dip of 45° the fault slips at an average rate of 29 m/Ma throughout the second phase after cessation of regional extension. The additional fault slip amounts to around 86 m. For the steeper fault dip of 75° a short period of normal slip during ~ 30 ka at a rate of 17 m/Ma is followed by reverse slip at a rate of -7 m/Ma until the end of the model run. The additional fault displacement obtained is ~ 0.5 m.

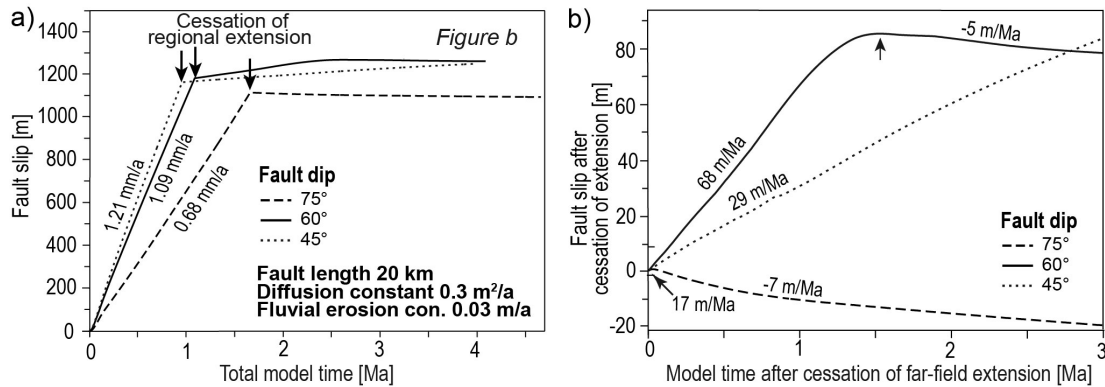


Figure 13: Results of the experiments with variable fault dip and constant fault length of 20 km. The diffusion and fluvial erosion constants are the same as in the reference model. Note that the slip rates are average values. *a)* Complete model runs for each model setup with variable fault dip. The end of the first phase, i.e. the time point of cessation of regional extension, is indicated by arrows. The line with dots corresponds to fault dip of 45° , the black line represents the 60° -dipping fault and the dashed curve indicates a fault dip of 75° . *b)* Fault slip evolution after the end of extension. In the experiment with a fault dip of 45° , the slip rate is averaged over 3 Ma. For other model runs the positive slip rates indicate normal sense of slip and average over the time between the end of regional cessation and the time point with the maximum amount of displacement. Negative slip rates indicate reverse sense of slip and average over the time between the time point with the maximum amount of displacement and the end of the model run. Note the different scales in Figures *a)* and *b)*.

Results from experiments with variable fault length

In contrast to the effect of fault dip, increasing fault length leads to higher slip rate during the first model phase. The diffusion constant k_D is $0.3 \text{ m}^2/\text{a}$ and the fluvial erosion constant $K_f \cdot p$ 0.03 m/a in all model runs. The fault dip is 60° . *Figure 14a* shows that the fault obtains displacement at rates varying between 0.57 mm/a (10 km) and 1.66 mm/a (40 km). Also the fault slip accumulation after the end of regional extension increases for higher fault lengths (*Figure 14b*). The fault displacement for a 40-km-long fault is similar to that of a 45° -dipping fault, when the fault slip evolution after cessation of extension is considered. The slip rate is 30 m/Ma and the additional fault slip amounts to 86 m. For the 10-km-long fault the slip rate is 19 m/Ma until 160 ka. The fault slip reaches ~ 3 m and the reverse slip after that has a very low rate (-1 m/Ma).

Amount of erosion and sedimentation with and without regional extension

In the vicinity of the fault, the average amount of erosion on the footwall and sedimentation on the hanging wall was determined through time between the fault tips on both sides of the fault's surface trace, respectively. The areas are indicated by white dashed frames in *Figure 9*. *Table 3.2* comprises the average amount and rates of erosion (-) and sedimentation (+) for all model runs. To evaluate the relative effect of mass redistribution on the fault slip evolution, the width of the area is half of the fault length, i.e. 5 km for a 10-km-long fault, 10 km for a 20-km-long fault and 20 km for a fault of 40 km length. *Figure 15a* shows the average amounts of erosion and sedimentation for different diffusion and fluvial erosion constants throughout the complete model run.

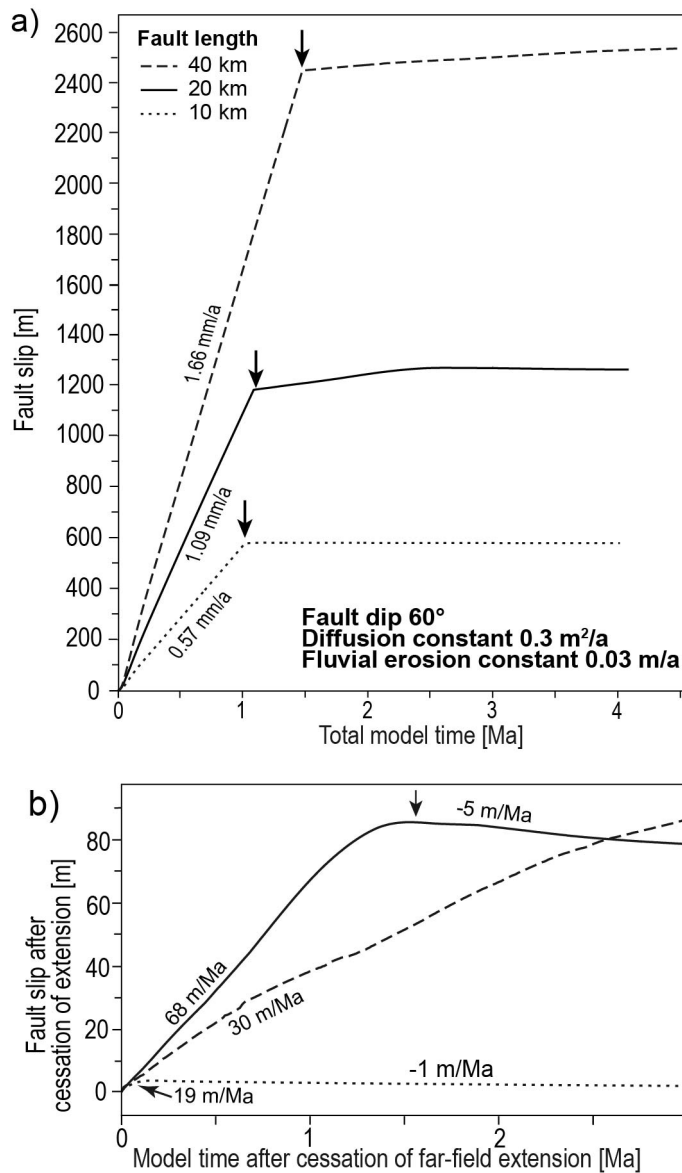


Figure 14: Results from the experiments with variable fault length (fault dip: 60°). The diffusion and fluvial erosion constants are the same as in the reference model. Note that the slip rates are average values. *a)* Complete model runs for each fault length. The end of the first phase, i.e. the time point of cessation of regional extension, is indicated by arrows. Both the slip rate and the time period of the first phase increase with increasing fault length. The line with dots corresponds to fault length of 10 km, the black line represents the 20-km-long fault and the dashed curve indicates a fault length of 40 km. *b)* Fault slip evolution after the end of extension. In the experiment with a fault length of 40 km, the slip rate is averaged over 3 Ma. For other model runs the positive slip rates indicate normal sense of slip and average over the time between the end of regional cessation and the time point with the maximum amount of displacement. Negative slip rates indicate reverse sense of slip and average over the time between the time point with the maximum amount of displacement and the end of the model run.

Table 3.2: Overview of the amount of erosion and sedimentation for experiments carried out for this study. Also shown are the length of the first model phase with regional extension and the parameters varied in the model runs. The length of the second model phase is 3 Ma in all experiments. The width of the area where the erosion and sedimentation was determined is half of the fault length.

Parameters varied in the experiments				Erosion (footwall)			Sedimentation (hanging wall)			
Fault length [km]	Fault dip [°]	Diffusion constant k_D [m^2/a]	Fluvial erosion constant $K_r \cdot p$ [m^2/a]	Duration of first model phase [Ma]	First model phase [m]	Second model phase [m]	Total [m]	First model phase [m]	Second model phase [m]	Total [m]
<i>Reference model</i>										
20	60	0.3	0.03	1.09	-60	-71	-131	63	67	130
<i>Variable diffusion constant</i>										
20	60	0.1	0.03	1.09	-38	-76	-114	35	61	96
20	60	0.5	0.03	1.09	-71	-62	-133	79	70	149
<i>Variable fluvial erosion constant</i>										
20	60	0.3	0.01	1.09	-53	-53	-106	56	58	114
20	60	0.3	0.05	1.09	-66	-83	-149	70	70	140
<i>Variable fault length</i>										
10	60	0.3	0.03	1.02	-41	-17	-58	61	31	92
40	60	0.3	0.03	1.48	-78	-131	-209	48	58	106
<i>Variable fault dip</i>										
20	45	0.3	0.03	0.96	-42	-88	-130	30	76	106
20	75	0.3	0.03	1.66	-60	-60	-120	65	53	118

Chapter 3

The first phase with far-field extension is indicated by the grey background and ends at 1.09 Ma of model time. Throughout the model run, i.e. within 4.09 Ma, both erosion and sedimentation decrease for lower diffusion constants k_D , resulting in a total of -114 m and 96 m for $k_D = 0.1 \text{ m}^2/\text{a}$ as well as -133 m and 149 m for $k_D = 0.5 \text{ m}^2/\text{a}$, respectively (Table 3.2). For $k_D = 0.3 \text{ m}^2/\text{a}$ both total erosion and sedimentation are around 130 m.

The evolution of the mass redistribution for different fluvial erosion constants $K_f \cdot p$ is shown in Figure 15b. Again, the first phase which includes the regional extension of the model is indicated by the grey background and ends at 1.09 Ma of model time. The mass redistribution decreases with decreasing fluvial erosion constant $K_f \cdot p$, whereas the difference between the model runs with $K_f \cdot p = 0.01 \text{ m/a}$ and 0.03 m/a is not that pronounced until the end of the first phase with regional extension. In the end of the model runs (after 4.09 Ma) the erosion and sedimentation result in -114 m and 96 m for the lowest $K_f \cdot p$ of 0.01 m/a as well as -133 m and 149 m for the highest value of $K_f \cdot p$ (0.05 m/a ; Table 3.2).

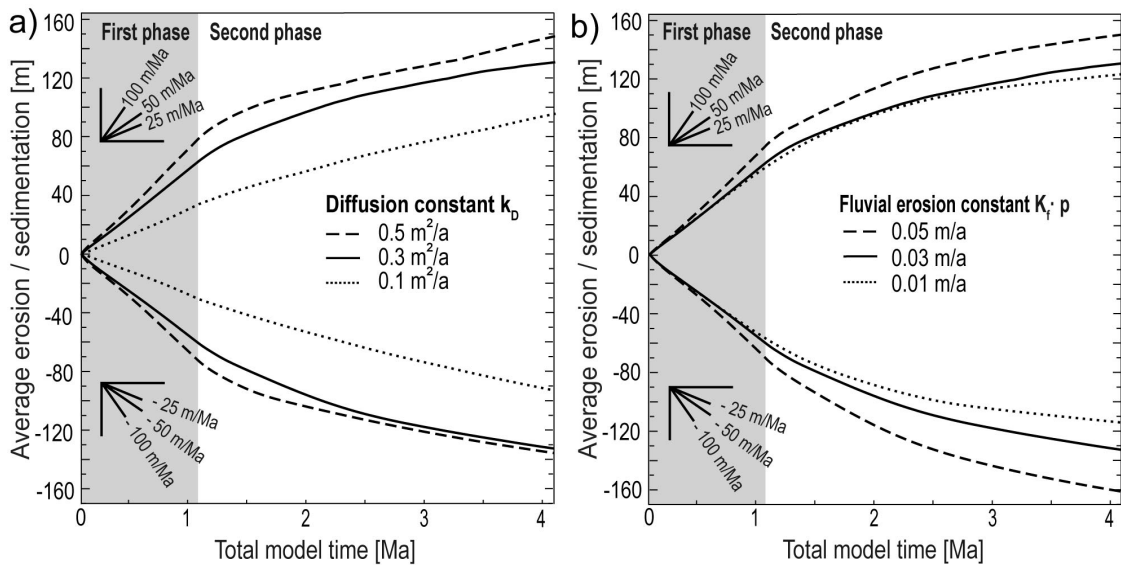


Figure 15: Average erosion in the footwall (-) and sedimentation in the hanging wall through time for parameters controlling the surface processes. The evolution of mass redistribution is shown for different diffusion constants k_D in Figure a). The line with dots corresponds to diffusion constant $k_D = 0.1 \text{ m}^2/\text{a}$, the black line represents the diffusion constant $k_D = 0.3 \text{ m}^2/\text{a}$ and the dashed curve indicates the diffusion constant $k_D = 0.5 \text{ m}^2/\text{a}$. The fault length is 20 km, the fault dip 60° and the fluvial erosion constant $K_f \cdot p$ is 0.03 m/a in all model runs. b) Effect of the fluvial erosion constant $K_f \cdot p$ on erosion and sedimentation. The line with dots represents the model run with $K_f \cdot p = 0.01 \text{ m/a}$, the black line corresponds to $K_f \cdot p$ of 0.03 m/a and the dashed curve shows the effect of fluvial erosion constant $K_f \cdot p = 0.05 \text{ m/a}$. The fault length is 20 km, the fault dip 60° and the diffusion constant k_D is set at $0.3 \text{ m}^2/\text{a}$ in all model runs. The first model phase with regional extension until 1.09 Ma of model time is marked by the grey rectangle. For comparison, the small graphics show different erosion and sedimentation rates.

Chapter 3

Figure 16a illustrates the effect of the fault dip on the sedimentation and erosion rates through time. The time point of maximum natural displacement according to the fault scaling law $D_{max} = 0.03 \cdot L^{1.06}$ (D_{max} = maximum displacement, L = fault length in metres; Schlische et al., 1996) varies for different fault dips and is indicated by arrows. Note that the run time after cessation of extension is 3 Ma for each model setup. From Figure 16a and Table 3.2 it is obvious that the fault dip affects the ultimate amount of mass redistribution in the vicinity of the fault. Thus, for the fault dipping at 45° the erosion is -130 m and the sedimentation 106 m. The corresponding amounts for the 75°-dipping fault are -120 m and 118 m, respectively.

The effect of fault length is shown in Figure 16b. Again, the time period until the maximum natural displacement is obtained depends on the fault length. The amount of mass redistribution increases with increasing fault length and the erosion results in -209 m and the sedimentation is 106 m for the 40-km-long fault. For a fault length of 10 km the erosion is -58 m and the sedimentation 92 m (Figure 16b, Table 3.2).

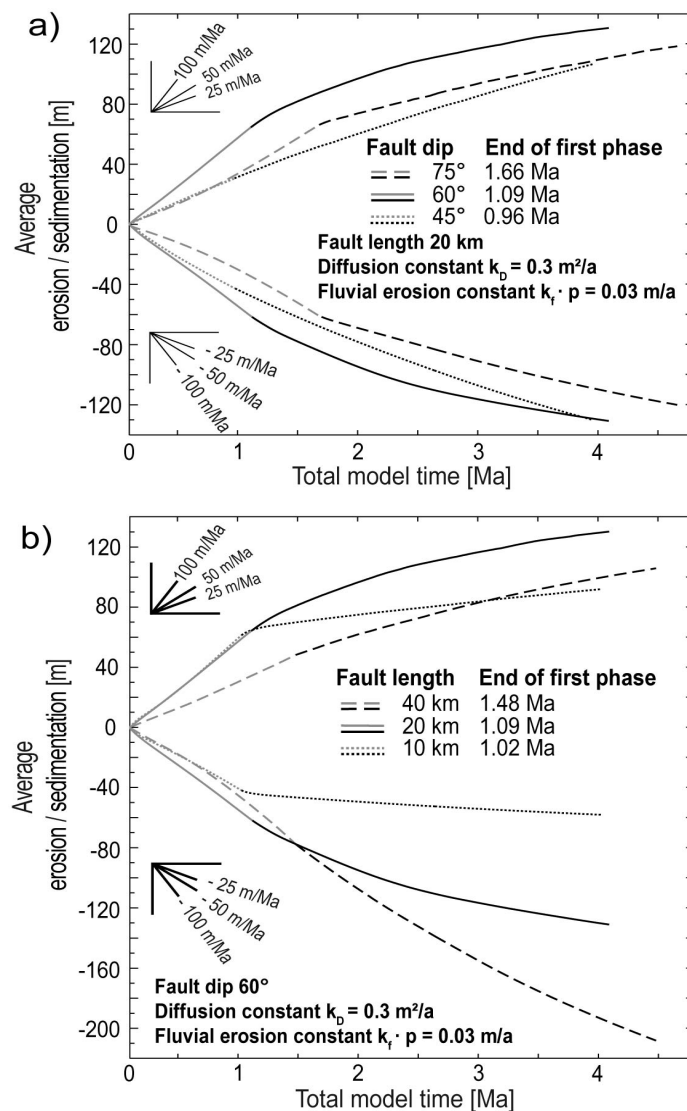


Figure 16: Average erosion (-) in the footwall and sedimentation (-) in the hanging wall through time for parameters controlling the fault geometry. The fluvial erosion constant $K_f \cdot p$ is 0.03 m/a and the diffusion constant k_D is set at 0.3 m²/a in all model runs. The first model phase with regional extension varies for different parameters and is marked by the grey curves from the beginning of each model run. For comparison, the small graphics show different erosion and sedimentation rates. The evolution of mass redistribution is shown for different fault dips in Figure a). The line with dots corresponds to fault a fault dip of 45°, the black line represents the 60°-dipping fault and the dashed curve indicates a fault dip of 75°. The fault length is 20 km. b) Effect of fault length on erosion and sedimentation. The line with dots corresponds to fault length of 10 km, the black line represents the 20-km-long fault and the dashed curve indicates a fault length of 40 km. The fault dip is 60° in all model runs.

3.4 Discussion

The model results indicate that surface processes may prolong fault slip accumulation for additional 10^5 - 10^6 years when regional extension ceases. The pattern for the fault slip evolution and the subsequent changes on the model surface depends on the parameters controlling the intensity of surface processes as well as the fault geometry. For example, an almost constant rate of fault displacement for several millions of years is obtained for a low diffusion constant ($0.1 \text{ m}^2/\text{a}$; *Figure 11b*), a shallow fault dip (45° ; *Figure 13b*) and a long fault (40 km ; *Figure 14b*). Additional model runs reveal, that when the run time is extended to $\sim 7 \text{ Ma}$ after the end of far-field extension, faults with a fault dip of 45° or diffusion constant $k_D = 0.1 \text{ m}^2/\text{a}$ are able to attain normal fault slip for more than 3 Ma before a reverse slip occurs (*Figure 17*).

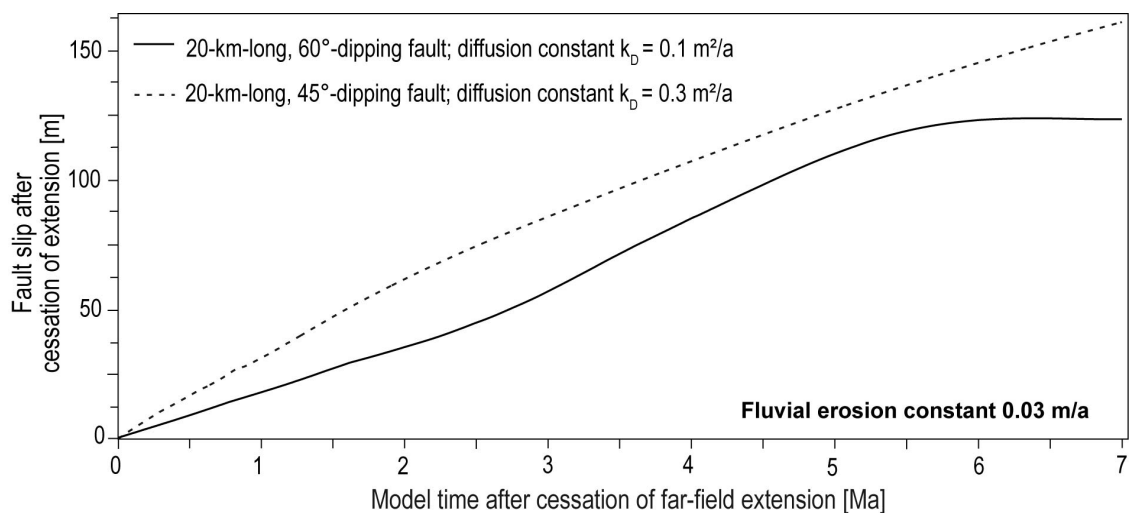


Figure 17: Additional model runs showing the fault slip evolution after cessation of regional extension for a 60° -dipping normal fault of 20 km length and with diffusion constant $k_D = 0.1 \text{ m}^2/\text{a}$ (grey line) and a 20-km -long fault with a dip of 45° and diffusion constant $k_D = 0.3 \text{ m}^2/\text{a}$ (black line).

In contrast, in model runs with intermediate and high diffusion constants (0.3 or $0.5 \text{ m}^2/\text{a}$; *Figure 11b*), an intermediate fault dip (60° ; *Figure 13b*) or length (20 km ; *Figure 14b*) the fault at first obtain normal slip for 0.5 - 1.5 Ma before a transition to slow reverse slip. For short or steeply dipping fault (75° or 10 km ; *Figure 13b, 14b*) only a short period of less than 200 ka of additional normal slip followed by a long period of slow reverse slip is observed (*Figure 13b, 14b*). The additional normal slip is accumulated at rates between 19 and 86 m/Ma (*Figs. 11-14*) with exception of the models with a short or steeply dipping fault. Such rates of fault displacement imply that after the cessation of regional extension, a 20-km -long normal fault would experience 25 to 115 additional earthquakes in 1 Ma assuming a magnitude ~ 6 and a coseismic slip of $\sim 0.75 \text{ m}$.

Chapter 3

The model results show that the prolongation of fault slip by surface processes is caused by the redistribution of mass on the model surface due to erosion, sediment transport and deposition. *Table 3.2* and *Figures 15* and *16* show that the average amounts of erosion and sedimentation range from around 40 to 210 m through time in different experiments. Hence, the resulting erosion rates in the fault footwall are similar to the catchment-wide erosion rates determined for the low-relief footwall of a young active normal fault in the Basin-and-Range Province ($10\text{-}35\text{ m/Ma}$; *Densmore et al., 2009*). In *Figures 15* and *16* it is also shown that in most experiments the difference between the amount of eroded and deposited material is less than ~ 30 m. Only in the experiment with a 40-km-long fault, much more material is eroded in the footwall than deposited in the hanging wall basin (*Figure 16b*). This is due to the fact that some material leaves the model via the model boundaries or is deposited outside the evaluated area on the hanging wall.

All experiments show similar pattern of interaction between the cessation of extension and the evolution of mass redistribution on the model surface. The end of the first model phase, i.e. the end of regional extension of the model, is governed by a more or less gradual transition to lower erosion and sedimentation rates. When compared with the slip histories of the faults (*Figs. 11 - 14*), it is obvious that the duration of the transition to lower erosion and sedimentation rates reflects the fault slip evolution after the cessation of extension. If no significant change of the erosion and sedimentation rates occurs after the end of extension (e.g. *Figure 15a*; $k_D = 0.1\text{ m}^2/\text{a}$), the accumulation of normal slip continues (*Figure 11a*). A transition from normal to reverse slip coincides with a significant reduction of the erosion and sedimentation rates (e.g. *Figure 13*, *Figure 15b*). If the erosion and sedimentation rates are suddenly reduced (e.g. *Figure 16b*; 10-km-long fault), a short phase of normal slip is followed by a long period of slow reverse slip (*Figure 14b*). When the evolution of the erosion and sedimentation rates and the fault slip history are compared, it is obvious that the slip behaviour of the fault is indeed a response to the mass redistribution on the model surface.

Figure 18a illustrates the topographic profiles on the model surface, which run perpendicular to the fault and were extracted from the reference model with a 20-km-long and 60° -dipping normal fault. Between the end of far-field extension at 1.09 Ma and the end of the model run at 4.1 Ma a lowering of the footwall can be observed. The highest point in the footwall is shifted away from the fault's surface trace due to erosion but the deepest point of the hanging wall basin remains almost at the same position during the second model phase. The elevation of the deepest point is first lowered by around 100 m until the maximum normal slip is reached at 2.63 Ma. The deepest point of the basin is located at a similar elevation at the beginning and at the end of the second model phase (*Figure 18a*). The model surfaces at successive time points (*Figure 18b-d*) show that a headward erosion of the streams gradually reduces

Chapter 3

the width of the highest part of the footwall. The area of the hanging wall basin decreases, while valleys that formed during the first model phase in the footwall are deepened and widened by river incision (*Figure 18c*).

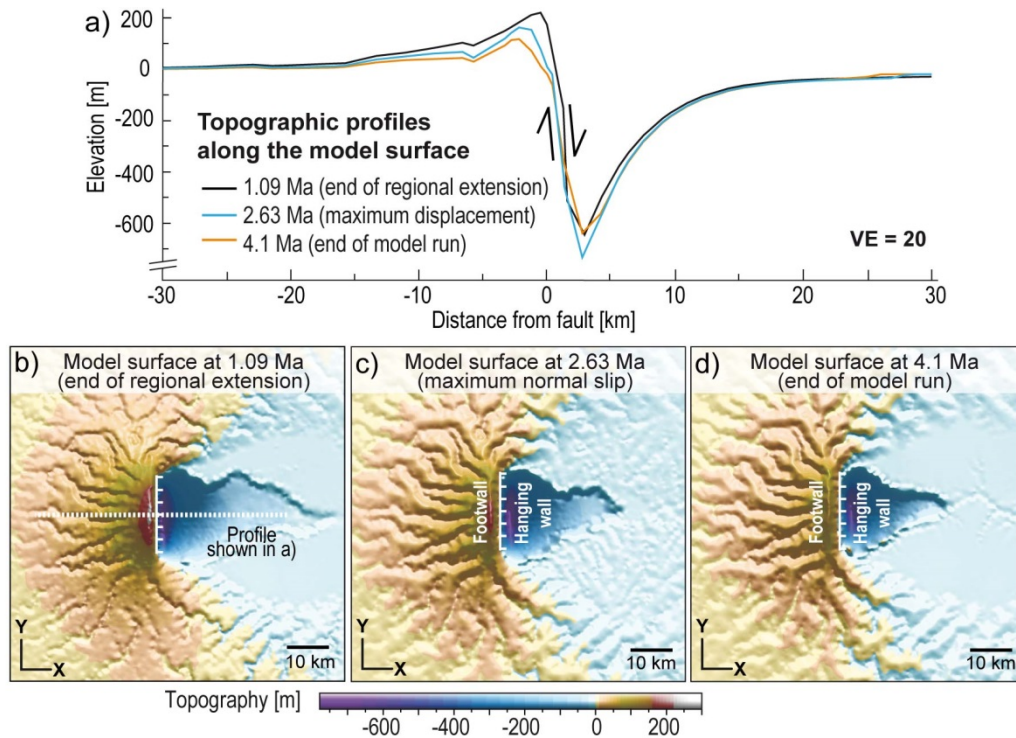


Figure 18: Topographic evolution of the model surface in the reference model. *a)* Topographic profiles along the model surface extracted at 1.09 Ma (cessation of far-field extension), 2.63 Ma (maximum normal displacement) and 4.1 Ma (end of model run). Vertical exaggeration (VE) is 20. The location of the profiles is shown *b)*. Map view of the model surface at *b)* 1.09, *c)* 2.63 and *d)* 4.1 Ma.

The mass redistribution that deforms the model surface impacts the stress field of the crust and ultimately the fault slip behaviour (*cf. Maniatis et al., 2009*). The local removal and addition of sediments due to erosion and sediment deposition, respectively, affects the vertical stress, which is the maximum principal stress σ_1 in regions of normal faulting, especially in the vicinity of the fault. In addition, the fault footwall experiences unloading by erosion and the hanging wall is subject to loading by sediment deposition, which lead to flexure of the crust and subsequently affect the horizontal stress, which is the minimum principal stress σ_3 for normal faults. The stresses were derived in the hanging wall at a depth of ~ 3 km. The net effect of the changes in vertical and horizontal stresses reflects the variations in the differential stress ($\sigma_1 - \sigma_3$), which are temporarily in accordance with the changes in erosion and sedimentation rates and hence also govern the fault slip evolution (*Figure 19*). An exception is the 40-km-long fault, where the differential stress decreases, although

Chapter 3

the fault accumulates slip at a relatively constant rate (*Figure 14*). The decrease in the differential stress may result from the unloading of the footwall due to erosion, which significantly exceeds the amount of sedimentation on the hanging wall (*Figure 16b*). This leads to more pronounced decrease in the vertical stress (σ_1) in the footwall due to erosion and hence to a stress drop in the vicinity of the fault. Although doing so, the failure criterion of Mohr-Coulomb still remains fulfilled and faulting continues.

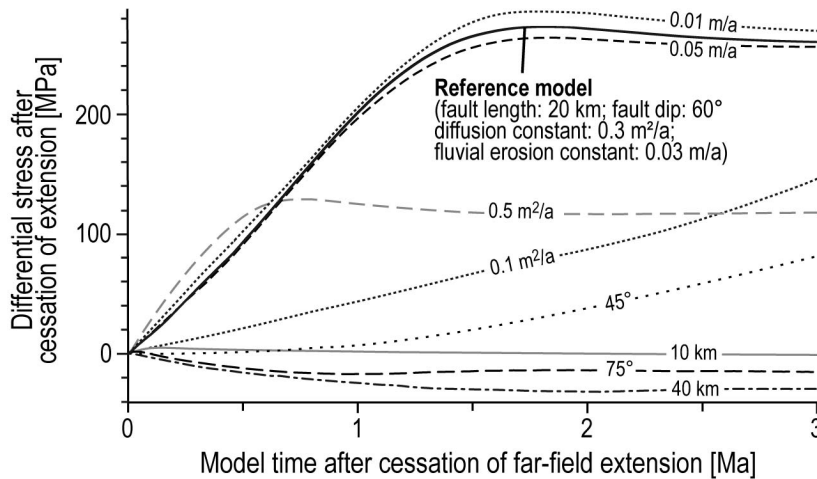


Figure 19: Evolution of the differential stress at a point in the fault hanging wall at ~ 3.5 km depth after cessation of regional extension. The labels at the individual curves indicate the parameter that was varied in the respective experiment compared to the reference model.

The findings indicate that the activity of normal faults in natural settings considering rifts and graben systems may be prolonged when the far-field tectonic boundary conditions that originally caused the extension change. However, exact timing of the cessation of regional extension may be difficult, since the apparent transition from syn- to post-rift sedimentation (as, for example, derived from seismic reflection profiles) may not coincide with the end of the regional extension. Hence, sediments deposited in the hanging wall of the normal faults may be further tectonically deformed after regional extension has ceased. The models of the present study imply that an abrupt reduction in the erosion and sedimentation rates after cessation of regional extension may lead to reverse slip on the fault. In other words, such an inversion would not be necessarily associated with an onset of far-field shortening.

The graben system of the northern North Sea provides a natural example where continued fault slip owing to erosion and sediment deposition may have played a role. For the post-rift stage initiated in the lower Cretaceous, subsidence curves derived from seismic reflection profiles show a discrepancy of >200 m between the

Chapter 3

observed subsidence and the thermal subsidence predicted by the *McKenzie (1978)* model, indicating a deceleration of subsidence or relative uplift (*Gabrielsen et al., 2001*). To explain this discrepancy, several mechanisms were proposed including a widespread thermal event (*Rohrman and van der Beek, 1996*), inversion associated with intra-plate shortening (*Cloetingh et al., 1985*) or extension in response to the opening of the Atlantic further south (*Skibeli et al., 1995*). Due to the results discussed above it can be speculated that post-rift erosion of the rift shoulders as well as sediment transport and deposition in the basins may have contributed to prolong the activity of the normal faults. As the post-rift erosion and sedimentation rates varied between the different regions of the northern North Sea (*Gabrielsen et al., 2001*), the amount of post-rift faulting may also have varied.

3.5 Conclusions

The experiments run by using three-dimensional finite-element models with full coupling between faulting and surface processes show that the fault slip accumulation of a normal fault may continue for up to 10^6 years after the end of regional extension if erosion, sediment transport and deposition continue to be active. The amount of accumulated post-extensional displacement on the fault is primarily controlled by the diffusion constant, fault dip and length, whereas it is less affected by the fluvial erosion constant. Surface processes induce mass redistribution which affects the stress state, which, in turn, affects the prolonged fault displacement. The results imply that in regions where the main tectonic activity has ceased, earthquakes may still occur because the fault-generated topography continues to be affected by surface processes.

4. Influence of surface processes on normal fault arrays

4.1 Motivation

After evaluating the response of a single fault, the study was extended to more complex structures consisting of several normal faults. The main question of this study is how surface processes may affect the slip evolution of faults depending on their position in a fault array and how faults interact with each other. The models can be applied, for example, to the Gulf of Corinth where the elongated basin borders on roughly E-W oriented en echelon normal faults (e.g. Briole *et al.*, 2000; Moretti *et al.*, 2003; Sachpazi *et al.*, 2003; Avallone *et al.*, 2004; McNeill *et al.*, 2005; Lykousis *et al.*, 2007; Sakellariou *et al.*, 2007; Taylor *et al.*, 2011; Ford *et al.*, 2013) (Figure 20).

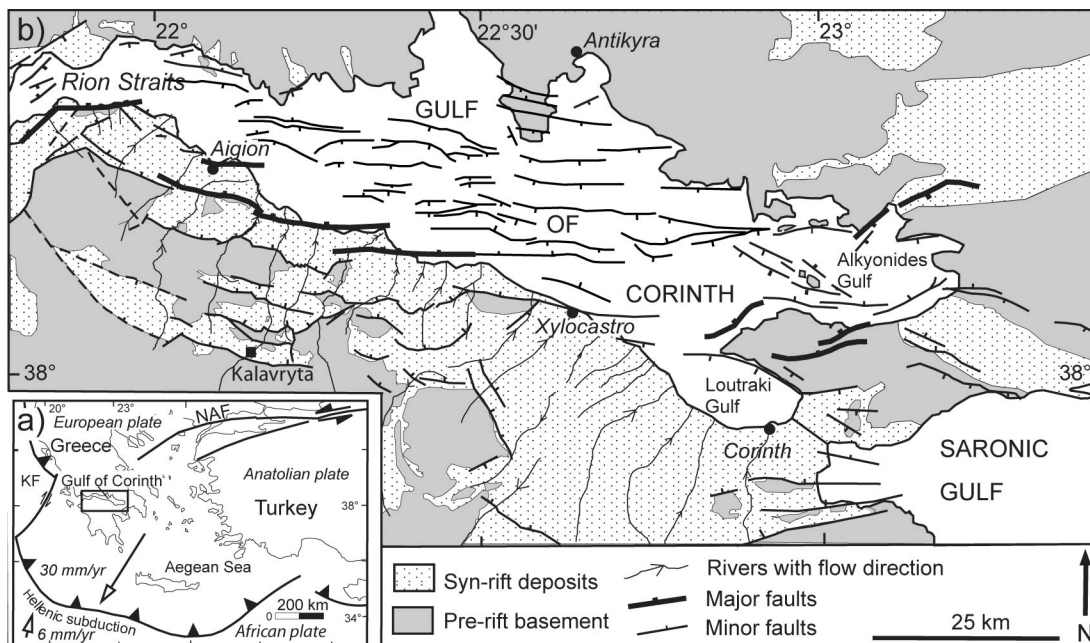


Figure 20: Overview of the Gulf of Corinth (Modified after Ford *et al.*, 2013). a) The location of the Gulf between Peloponnese peninsula and the mainland of Greece. The Gulf of Corinth is highlighted by the black frame. The velocities of the tectonic plates are indicated by arrows. The NAF is the North Anatolian Fault and KF the Kefalonia Fault. The more detailed map with faults and rivers is shown in b).

The length of the graben system is around 110 km and the width decreases from around 30 km in the east to less than 2 km in the western part (Moretti *et al.*, 2003; Lykousis *et al.*, 2007; Ford *et al.*, 2013). In this rift system, the N-S extension has been inferred to have started in the eastern part in the Pliocene and then propagated westward (Moretti *et al.*, 2003). Hence, the eastern part of the gulf is wider and deeper than the western part and the thickness of syn-rift sediments decreases from

Chapter 4

almost 3 km in the east to a few hundred meters in the west (Moretti *et al.*, 2003; Lykousis *et al.*, 2007; Taylor *et al.*, 2011). The corresponding water depths in the basin result in around 900 m and 65 m, respectively (Brooks and Ferentinos, 1984; Moretti *et al.*, 2003; Lykousis *et al.*, 2007). GPS measurements show that the current extension rate increases from <10 mm/a in the east to ~15 mm/a in the west (Briole *et al.*, 2000; Avallone *et al.*, 2004; Floyd *et al.*, 2010). Although the present-day opening rate is higher in the western part of the Gulf of Corinth, the eastern part remains seismically active, as evident from a sequence of $M_s > 6$ earthquakes that occurred in the eastern part of the graben in 1981 (Jackson *et al.*, 1982).

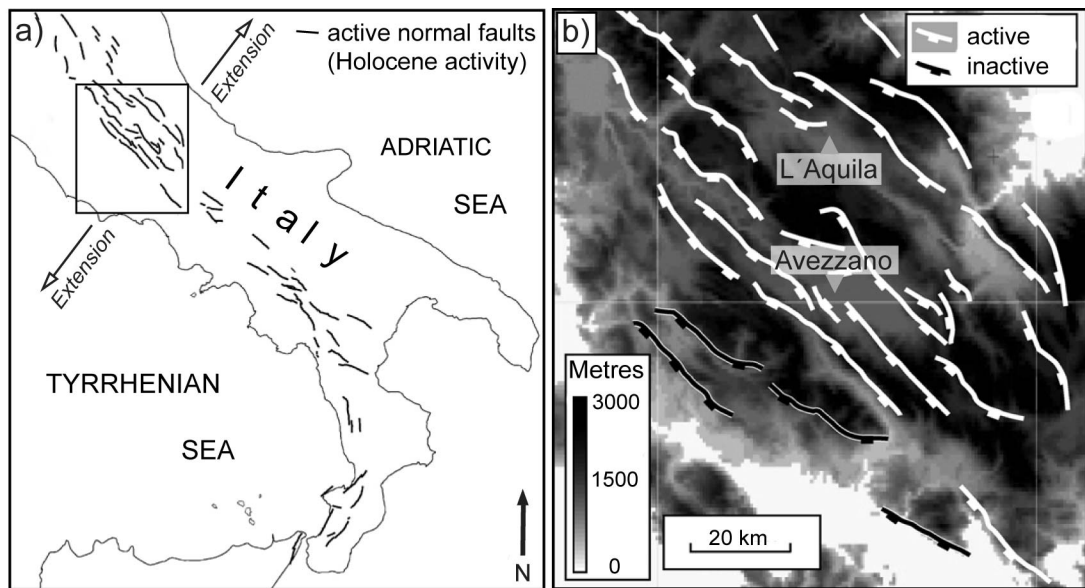


Figure 21: Overview of the Apennines. *a)* Active normal faults that intersect the Holocene deposits (Modified after Roberts and Michetti, 2004; Roberts, 2006). The approximate direction of extension is indicated by the arrows. The black rectangle marks the Lazio-Abruzzo region shown in the 1 km² pixel digital elevation model in *b)* (Modified after Roberts and Michetti, 2004).

Another example of normal fault arrays are the Apennines, Italy (Figure 21). Especially the Lazio-Abruzzo region of the central Apennines is a matter of common interest, since the faults have been active through the Holocene with several $M_s > 5.5$ earthquakes also during the last 100 years (e.g. Westaway *et al.*, 1989; Michetti *et al.*, 1996). One of the most recent devastating earthquakes in the central Apennines ruptured with M_w 6.3 on 6th April 2009 hitting L'Aquila located in the northern part of the fault array (e.g. Chiarabba *et al.*, 2009; Bonini *et al.*, 2013; Guglielmino *et al.*, 2013) (Figure 2b). The area of Lazio-Abruzzo is around 155 km long and 55 km wide, NW-SE oriented thrust belt enclosing several parallel as well as an echelon normal faults (Cowie and Roberts, 2001; Roberts and Michetti, 2004) with lengths between ~20 and 40 km (Roberts and Michetti, 2004), which correspond to the fault lengths of 20 - 30 km used in the present study. The generally NE-SW trending extension (Montone *et al.*, 1999) began in the late Pliocene (Cavinato and de Celles,

Chapter 4

1999; Roberts and Michetti, 2004). The velocity of the horizontal extension is ~ 4 mm/a for the last 18 ka in the central area of Lazio-Abruzzo Apennines when derived from vertical offsets on faults (Roberts and Michetti, 2004; Roberts, 2006), which is similar to the rate of ~ 3 mm/a derived from GPS measurements and earthquake slip vectors (D'Agostino et al., 2008; D'Agostino et al., 2011).

In the following, arrays constrained by 4 and 6 normal faults are studied. After introduction of the model setup for both arrays, the next passage describes the effect of diffusion constant k_D on the morphology due to erosion and sedimentation and the subsequent effect on the fault slip evolution. Afterwards, the results are discussed and applied to natural examples mentioned above.

4.2 Model setup

The models consist of a 200 km by 200 km wide lithosphere instead of 100 km by 100 km used for the model runs for a single fault. The Cascus-cell is limited to an area of 100 km by 100 km. The total length of both arrays in the middle of the model, i.e. in the middle of the Cascus-cell, results in 64 km (Figure 22a, b). The initial noise on the top of the Cascus-cell is up to 150 m in the horizontal direction and up to 2 m in the vertical direction. Since the model is larger than the one used for the single faults the phase of pre-faulting is prolonged to 200 ka to achieve the same amount of initial morphology for Cascus than in the smaller models for isolated normal faults.

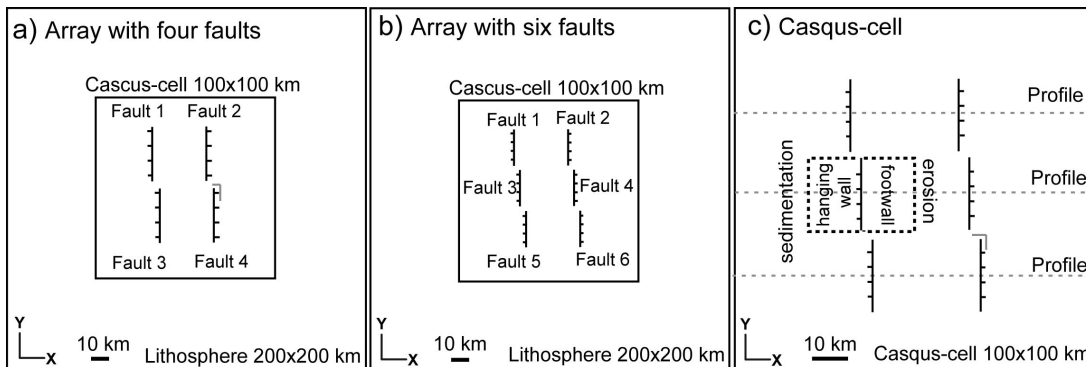


Figure 22: Schematic model sketches showing the horst structures for an array of a) four 30-km-long normal faults and b) six 20-km-long normal faults. The fault dip is 60° and the width of the horst results in 30 km on the model surface. The Cascus-cell on which the surface processes are applied is limited to 100x100 km and encloses the fault array. c) The position of the profiles on the model surface within the cascus-cell (dashed grey lines) as well as an example of the areas for sedimentation in the hanging wall and erosion in the footwall (dashed black rectangles). The grey lines in Figures a) and c) indicate the approximate position of the prescribed canyon.

Chapter 4

The first fault array that was examined consists of an around 30 km wide horst bounded by four 30-km-long normal faults with a fault dip of 60° . The distance between the fault tips of consecutive faults in the en-echelon array is 4 km both in x- and y-directions (*Figure 22a*). For the second horst structure three 20-km-long, also 60° -dipping faults bounding the horst on one side are arranged as a left-stepping en echelon structure. The distance between the fault tips of the sequenced faults is 4 km in x-direction and 2 km in y-direction. A fault array with same configuration but different dip direction is present in the other side of the horst, so that the distance between the fault surface traces is ~ 30 km (*Figure 22b*). Also an additional model run with a prescribed canyon between 2 faults was performed for both arrays to examine the effect of deliberate loading of a specific hanging wall with sediments. The canyon was constructed by lowering and lifting selected nodes by 50 meters to allow or prohibit, respectively, the sediment flow in specific directions from the beginning of the model run. The position of the predefined canyon is also illustrated in *Figure 22a* for the array with 4 faults and in *Figure 22c* for the array with 6 faults.

4.3 Model results

For both fault arrays surface processes lead to formation of rivers that incise the horst structure and transport sediments either out of the model or to the hanging wall basins. Elevated parts in the footwall are generally lowered due to erosion and the hanging walls experience further subsidence and filling due to sediment supply from the footwall.

4.3.1 Horst bounded by 4 x 30-km-long faults

The amount of fault slip accumulated after the complete model run without surface processes is shown in *Table 4.1*. The total fault displacement was determined from a node in the middle of the fault in the hanging wall at 2 km depth, e.g. beneath the Casqus layer. The highest fault slip of 1471 m is obtained by fault 2 followed by fault 4 with 1464 m. Fault 3 accumulates 3 m less fault slip than fault 4. Fault 1 accumulates the slowest fault slip and the total displacement results in 14 m less than for fault 2.

Effect of the diffusion constant and fluvial erosion constant on fault slip

The cumulative fault slip shown in *Table 4.1* indicates that the total fault slip accumulation increases with increasing k_D for each fault. Again, fault 1 accumulates the lowest fault displacement for all diffusion constants k_D , while fault 2 obtains the highest fault slip accumulation resulting in up to 30 m more than for fault 1. Although the model run with diffusion constant $k_D = 0.5$ m²/a ran until around 1.62 Ma, it is possible to compare the fault slip rates because a steady-state slip accumulation has been already obtained until that point in time (*Table 4.1*).

Chapter 4

Table 4.1 Total displacement in the middle of each fault after 2.4 Ma of model time at 2 km depth in the hanging wall for all model runs with and without surface processes for the array with 4 faults. Also shown are the results for the model run with predefined river. Note that since some model runs were not completed, the resulting displacement at 1.62 Ma of model time is indicated by grey *italic type* for all model runs with surface processes. In the experiments on the diffusion constant the fluvial erosion constant is kept constant at 0.03 m/a. In the experiments on fluvial erosion constant the diffusion constant is 0.3 m²/a.

Total fault displacement [m]						
<i>With surface processes</i>						
Fault	<i>without surface processes</i>	diffusion constant k_D [m ² /a]			fluvial erosion constant $K_f \cdot p$ [m/a]	
		0.1	0.3	0.5	0.01	0.05
1	1457	1591	1610	-	1618	1618
	<i>980</i>	<i>1067</i>	<i>1089</i>	<i>1104</i>	<i>1100</i>	<i>1092</i>
2	1471	1619	1670	-	1642	1649
	<i>990</i>	<i>1084</i>	<i>1118</i>	<i>1133</i>	<i>1126</i>	<i>1114</i>
3	1461	1605	1646	-	1631	1651
	<i>984</i>	<i>1078</i>	<i>1108</i>	<i>1118</i>	<i>1114</i>	<i>1112</i>
4	1464	1609	1643	-	1635	1641
	<i>987</i>	<i>1078</i>	<i>1108</i>	<i>1118</i>	<i>1119</i>	<i>1110</i>
<i>with prescribed canyon</i>						
2	-	-	1647	-	-	-
	-	<i>1084</i>	<i>1115</i>	<i>1134</i>	-	-
4	-	-	1654	-	-	-
	-	<i>1078</i>	<i>1112</i>	<i>1118</i>	-	-

The predefined river that starts in the footwall and then flows on the ramp between the faults and imports sediments into the hanging wall basin of fault 4 instead of the hanging wall basin of fault 2. This leads to an additional displacement of 11 m the middle of the fault 4 at 2 km depth after 2.4 Ma of model time for diffusion constant $k_D = 0.3$ m²/a. In contrast, in the same model run fault 2 now receives less sediments on its hanging wall and experiences a decrease of 23 m in the fault slip accumulation. Due to convergence not being possible the model runs with the predefined canyon run until 1.62 Ma and 1.64 Ma for diffusion constant $k_D = 0.1$ m²/a and 0.5 m²/a, respectively. For comparison, the fault slip accumulated until 1.62 Ma of model time for all model runs with and without prescribed canyon is also shown in *Table 4.1*. As seen in *Table 4.1*, the influence of the prescribed river on the slip rates of fault 2 and fault 4 has been relatively low until 1.62 Ma. The difference between the fault slip accumulated for model runs with and without induced canyon at that time point is up

Chapter 4

to 4 m whereas the difference amounts to up to 23 m for 2.4 Ma of model time. At the end of the model run, the fault slip is lowered for all faults except fault 1 for lower fluvial erosion constant in the experiments with diffusion constant = 0.3 m²/a. Higher fluvial erosion constant leads to a decrease of fault slip accumulation on fault 2 und fault 4 after 2.4 Ma of model time.

Amount of erosion and sedimentation in models with 4 x 30-km-long faults

The average erosion in the end of the model runs was derived from a 30-km-long and 15-km-wide area in the footwall. The corresponding amount of sedimentation was extracted from the hanging wall (*Figure 22c*). *Table 4.2* shows the erosion and sedimentation accumulated until 2.4 Ma and 1.62 Ma of model time for all model runs and diffusion constants k_D . In general both sedimentation and erosion increase with increasing diffusion constant k_D for each fault. From the available results it is obvious that the lowest total sedimentation is accommodated by fault 4 in all model runs, varying between 63 m and 84 m for the model run until 2.4 Ma and from 36 m to 56 m for the model run until 1.62 Ma (*Table 4.2*).

Table 4.2 Cumulative amount of erosion (-) and sedimentation derived from the footwall and the hanging wall, respectively, for the array with 4 faults. Also shown are the results for one model run with predefined river redirecting the sediment flow into the hanging wall of fault 4. Note that since some model runs were not completed, the cumulative erosion and sedimentation at 1.62 Ma of model time is indicated by grey *italic type*. In the experiments on fluvial erosion constant the diffusion constant is 0.3 m²/a.

Total amount of erosion (-) and sedimentation [m]					
Fault	diffusion constant k_D [m ² /a]			fluvial erosion constant $K_f \cdot p$ [m/a]	
	0.1	0.3	0.5	0.01	0.05
	1	-93/69 <i>-52/41</i>	-119/88 <i>-68/52</i>	- <i>-63/57</i>	-69/71 <i>-41/46</i>
2	-87/77 <i>-48/44</i>	-103/153 <i>-56/85</i>	- <i>-62/89</i>	-63/84 <i>-40/52</i>	-126/107 <i>-70/62</i>
3	-91/82 <i>-51/48</i>	-104/108 <i>-59/63</i>	- <i>-61/66</i>	-61/82 <i>-38/52</i>	-131/136 <i>-73/77</i>
4	-98/63 <i>-55/36</i>	-121/84 <i>-71/50</i>	- <i>-74/56</i>	-74/65 <i>-46/43</i>	-135/97 <i>-77/57</i>
<i>With prescribed canyon</i>					
2	- <i>-</i>	-108/80 <i>-61/52</i>	- <i>-</i>	- <i>-</i>	- <i>-</i>
4	- <i>-</i>	-118/158 <i>-68/88</i>	- <i>-</i>	- <i>-</i>	- <i>-</i>

Chapter 4

Hence, the cumulative sedimentation rates for fault 4 vary from 0.026 mm/a to 0.035 mm/a until 2.4 Ma of model time and between 0.022 mm/a and 0.035 mm/a after 1.62 Ma. As seen in *Table 4.2* the highest total sedimentation for both 2.4 Ma and 1.62 Ma of model time is obtained by fault 3 for the diffusion constant $k_D = 0.1 \text{ m}^2/\text{a}$ (82 m and 48 m) and by fault 2 for the diffusion constant $k_D = 0.3 \text{ m}^2/\text{a}$ (153 m and 85 m). The corresponding sedimentation rates for fault 3 and diffusion constant $k_D = 0.1 \text{ m}^2/\text{a}$ amount to 0.034 mm/a until 2.4 Ma and to 0.030 mm/a until 1.62 Ma. For fault 2 in the model run with diffusion constant $k_D = 0.3 \text{ m}^2/\text{a}$ the sedimentation rates amount to 0.064 mm/a at 2.4 Ma of model time and to 0.052 mm/a until 1.62 Ma.

The model run with the predefined canyon between faults 2 and 4 and diffusion constant $k_D = 0.3 \text{ m}^2/\text{a}$ shows that the sedimentation in the hanging wall of fault 4 increases from 84 m to 158 m until 2.4 Ma. This results in an increased sedimentation rate of 0.066 mm/a. Until 1.62 Ma the amount of sedimentation increases from 50 m to 88 m, leading to a sedimentation rate of 0.054 mm/a. In contrast, the sedimentation in the hanging wall of fault 2 decreases from 153 m to 80 m until 2.4 Ma and from 85 m to 52 m until 1.62 Ma when compared with the corresponding model runs without prescribed river. The sedimentation rate decreases to 0.033 mm/a until 2.4 Ma and to 0.032 mm/a until 1.62 Ma. These changes in the sedimentation rates correlate with the changes in the fault slip accumulation shown in *Table 4.1*.

The highest erosion rate is obtained by fault 4 in all model runs with different diffusion constants k_D . The cumulative erosion increases with increasing diffusion constant k_D and hence varies from 55 m to 74 m until 1.62 Ma. The erosion rate increases from 0.034 mm/a to 0.046 mm/a. During the same time span fault 3 experiences erosion from 51 to 61 m, indicating an erosion rate of 0.031 mm/a to 0.038 mm/a. The erosion on the footwall of fault 2 increases from 48 m to 62 m with increasing diffusion constant k_D until 1.62 Ma. That means erosion rates from 0.030 mm/a to 0.038 mm/a. The erosion on the footwall of fault 1 is the highest for diffusion constant $k_D = 0.3 \text{ m}^2/\text{a}$ and results in 68 m. Thus the erosion varies from 52 to 68 m, i.e. from 0.032 mm/a to 0.042 mm/a.

4.3.2 Horst bounded by 6 x 20-km-long faults

Table 4.3 shows the total fault slip accumulation in the middle of the fault at 2 km depth in the hanging wall for all model runs. The model run without surface processes shows that the total displacement for fault 1 (1138 m) is 5 meters higher than for fault 2 (1133 m). Fault 3 in the middle of the model accumulates the highest displacement of 1168 m, which is very similar to the fault slip accumulation of fault 4 (1167 m). For fault 5 the fault slip amounts to 25 m more than for fault 6 (1124 m), the latter being the lowest in the horst structure. The results show that the opposed distal faults do not accumulate fault slip at the same rate.

Chapter 4

Effect of the diffusion constant and fluvial erosion constant on fault slip

From *Table 4.3* it is obvious that for each fault the accumulated fault slip increases with increasing k_D . The relations within the fault array also remain the same, e.g., the central faults 3 and 4 experience the highest fault displacement of up to 1323 m while faults 1 and 6 accumulate slip up to 46 m and 70 m less, respectively. In the model run with prescribed canyon transporting sediments from the footwall of fault 4 into the hanging wall basin of fault 6 the highest fault displacement in the middle of the fault for fault 6 is obtained for diffusion constant $k_D = 0.3 \text{ m}^2/\text{a}$ (1279 m) and the lowest for diffusion constant $k_D = 0.1 \text{ m}^2/\text{a}$ (1210 m). The fault slip accumulation in the middle of the fault 4 remains the same for both model runs with and without prescribed canyon. The fault slip is lowered by a few meters for all faults for higher fluvial erosion constant in the experiments with diffusion constant = $0.3 \text{ m}^2/\text{a}$. For lower fluvial erosion constant the fault slip accumulation is increased by up to $\sim 14 \text{ m}$ for after 2.4 Ma of model time. The results from the model run with the lower fluvial erosion constant (0.01 m/a) are similar to those for the higher diffusion constant ($0.5 \text{ m}^2/\text{a}$).

Table 4.3: Total displacement in the middle of each fault at 2 km depth in the hanging wall for all model runs with and without surface processes for the array with 6 faults. Also shown are the results for the model run with prescribed river. In the experiments on the diffusion constant the fluvial erosion constant is kept constant at 0.03 m/a . In the experiments on fluvial erosion constant, the diffusion constant is $0.3 \text{ m}^2/\text{a}$.

Total fault displacement [m]						
<i>With surface processes</i>						
Fault	<i>without surface processes</i>	diffusion constant k_D [m^2/a]			fluvial erosion constant $K_f \cdot p$ [m/a]	
		0.1	0.3	0.5	0.01	0.05
1	1138	1234	1270	1284	1284	1266
2	1133	1226	1277	1288	1291	1273
3	1168	1276	1303	1319	1313	1302
4	1167	1280	1311	1323	1324	1308
5	1149	1248	1290	1303	1310	1286
6	1124	1210	1263	1275	1276	1255
<i>with prescribed canyon</i>						
4	-	1280	1311	1323	-	-
6	-	1210	1279	1273	-	-

Chapter 4

Amount of erosion and sedimentation in models with 6 x 20km normal faults

The rates of average erosion and sedimentation were derived from 20-km-long and 10-km-wide areas in the footwall and hanging wall, respectively (*Figure 22c*). The total amount of average erosion and sedimentation for different values of diffusion constant (k_D) and fluvial erosion constant ($K_f \cdot p$) are shown in *Table 4.4*. Similar to fault displacement described above both erosion and sedimentation increase for higher diffusion constant and fluvial erosion for each fault. Note that in experiments on diffusion constant the fluvial erosion is 0.03 m/a. In experiments on the fluvial erosion constant the diffusion constant is 0.3 m²/a.

The total erosion of 84 to 110 m for fault 6 is the highest in the fault array for all diffusion constants k_D . This results in an erosion rate of 0.035 mm/a to 0.046 mm/a. The corresponding amounts for faults 3 and 4 (82 m to 103 m, 0.034 mm/a and 0.043 mm/a) in the middle of the horst structure are lower. Conversely, the total sedimentation in the hanging wall of fault 6 increases from 61m to 98 m with higher diffusion constant k_D but remains the lowest in the array with corresponding erosion rates of 0.025 mm/a - 0.041 mm/a. In general, for all diffusion constants k_D fault 5 experiences the lowest average erosion rates in the footwall (79 m to 96 m) and the highest average sedimentation in the hanging wall (91 m to 125 m). The erosion rates vary between 0.033 mm/a and 0.040 mm/a and the corresponding sedimentation rate is 0.038 mm/a - 0.052 mm/a.

In the model run with prescribed canyon the sedimentation in the hanging wall of fault 4 is reduced by around 12 m for diffusion constant $k_D = 0.3$ m²/a and $k_D = 0.5$ m²/a as well as increased by 1 m for diffusion constant $k_D = 0.1$ m²/a when compared with the model run without prescribed canyon. The corresponding total erosion in the footwall of fault 4 varies for different diffusion constants k_D from 88 m to 112 m whereas the highest amount of erosion is obtained by the model run with diffusion constant $k_D = 0.3$ m²/a. Within 2.4 Ma of model time the erosion rate on the footwall of fault 4 increases from 0.037 mm/a to 0.047 mm/a. In the presence of the prescribed river the total erosion in the footwall of fault 6 remains almost unaffected when compared with the model run without prescribed canyon but the highest sedimentation in the hanging wall of fault 6 results in 179 m and is obtained by diffusion constant $k_D = 0.3$ m²/a. Thus, the sedimentation rate in the hanging wall of fault 6 increases from 0.038 mm/a to 0.076 mm/a. The amount of sedimentation and erosion for fault 6 is the lowest for diffusion constant $k_D = 0.1$ m²/a, both resulting in 84 m (0.035 mm/a). Lower fluvial erosion constant leads to decreasing erosion and sedimentation rates.

The all-over pattern within the array remains similar for experiments with lower fluvial erosion constant, i.e., the erosion on the footwall of fault 6 exceeds the corresponding amounts of the other faults by up to 13 m and the sedimentation is the

Chapter 4

lowest with up to 10 m less. For higher fluvial erosion the total amount of erosion and sedimentation for different faults increases by up to 20 m and 30 m, respectively, when compared to the model run with fluvial erosion constant = 0.03 m/a.

Table 4.4: Cumulative amount of erosion (-) and sedimentation derived from the footwall and the hanging wall, respectively, for the array with 6 faults. Also shown are the results for the model run with predefined river redirecting the sediment flow to the hanging wall of fault 6. In the experiments on the diffusion constant the fluvial erosion constant is 0.03 m/a In the experiments on fluvial erosion constant the diffusion constant is 0.3 m²/a.

Total amount of erosion (-) and sedimentation [m]					
Fault	Diffusion constant k_D [m ² /a]			fluvial erosion constant $K_f \cdot p$ [m/a]	
	0.1	0.3	0.5	0.01	0.05
1	-79/73	-95/99	-101/108	-74/83	-115/110
2	-83/80	-99/109	-104/115	-80/83	-119/126
3	-84/89	-97/109	-103/117	-73/87	-126/129
4	-82/76	-92/101	-97/109	-71/81	-118/118
5	-79/91	-92/116	-96/125	-71/90	-113/136
6	-84/61	-100/92	-110/98	-84/80	-118/97
<i>with prescribed canyon</i>					
4	-88/77	-112/89	-106/97	-	-
6	-84/84	-100/179	-109/141	-	-

4.4 Discussion

Fault array with 4 faults

Figures 23a and *b* show the Earth's surface after 2.4 Ma for model runs without surface processes and with surface processes for diffusion constant $k_D = 0.3$ m²/a, respectively. If the model surface is not subject to mass redistribution related to surface processes, the symmetry of slip distribution is similar for each fault, e.g., both the footwall and the hanging wall basin of each fault experience uniform uplift and deepening (*Figure 23a*). Surface processes lead to lowering of the highest areas in the footwall due to erosion and to formation of river networks that incise the horst structure and transport eroded material from the footwall either out of the model or into the hanging wall basins (*Figure 23b*). The river network evolution is imposed by further uplift and subsidence. While the subsidence of the hanging-wall basins of

Chapter 4

faults 1 and 4 is almost symmetrical, the hanging walls of faults 2 and 3 experience non-uniform loading. A relay ramp generated due to surface processes between faults 1 and 3 as well as between faults 2 and 4 controls the river direction from the footwall into the hanging wall basin. Due to increased sediment supply more than half of the hanging wall basin of fault 2 is filled with sediments mostly from the footwall of fault 4 after 2.4 Ma of model time. During the same time span sediments from the footwall of fault 1 are deposited in the hanging wall basin of fault 3 but do not yet reach the centre of the depression (*Figure 23b*). The model runs with diffusion constant $k_D = 0.1 \text{ m}^2/\text{a}$ and $k_D = 0.5 \text{ m}^2/\text{a}$ show similar morphology but the latter leads to relatively smooth model surface with less branched rivers and the former results in a more pronounced river network until 1.62 Ma of model time (*not shown*), which is in accordance with the earlier results of this study. In *Figure 24*, the experiments with different fluvial erosion constants show that the number of rivers significantly decreases for lower fluvial erosion constant but the channels are broader. For higher fluvial erosion constant the horst is cut by several branched rivers that lead to increased erosion, which is also shown in *Table 4.2*.

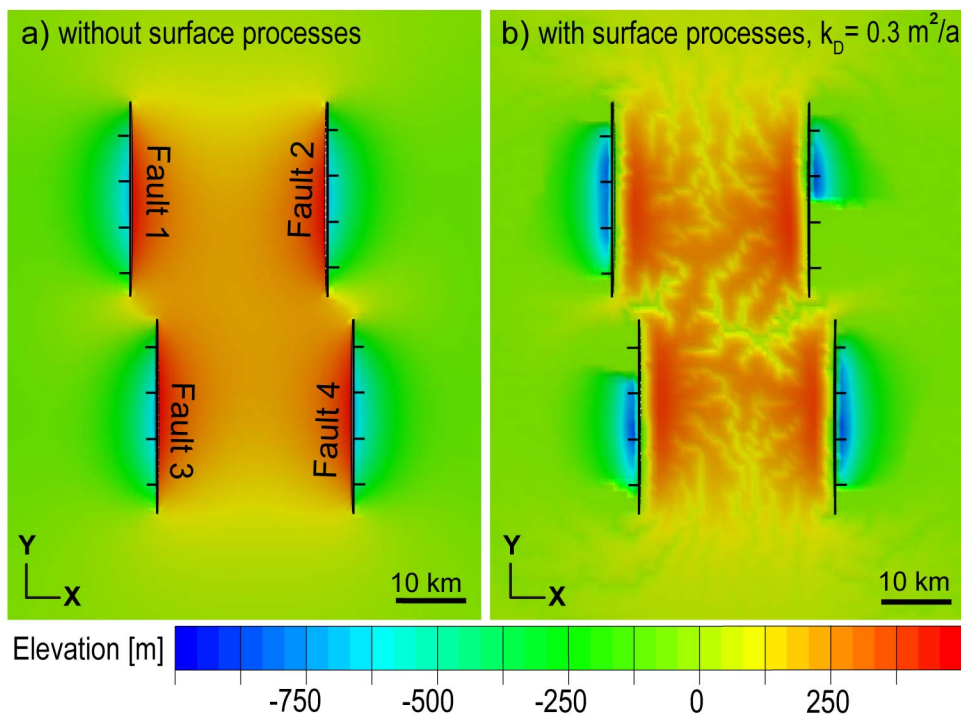


Figure 23: Central part of the model surface at 2.4 Ma of model time for a model a) without surface processes and for b) diffusion constant $k_D = 0.3 \text{ m}^2/\text{a}$. Figure a) also shows the disposition of the faults. These apply for all figures illustrating the fault array with four faults.

Chapter 4

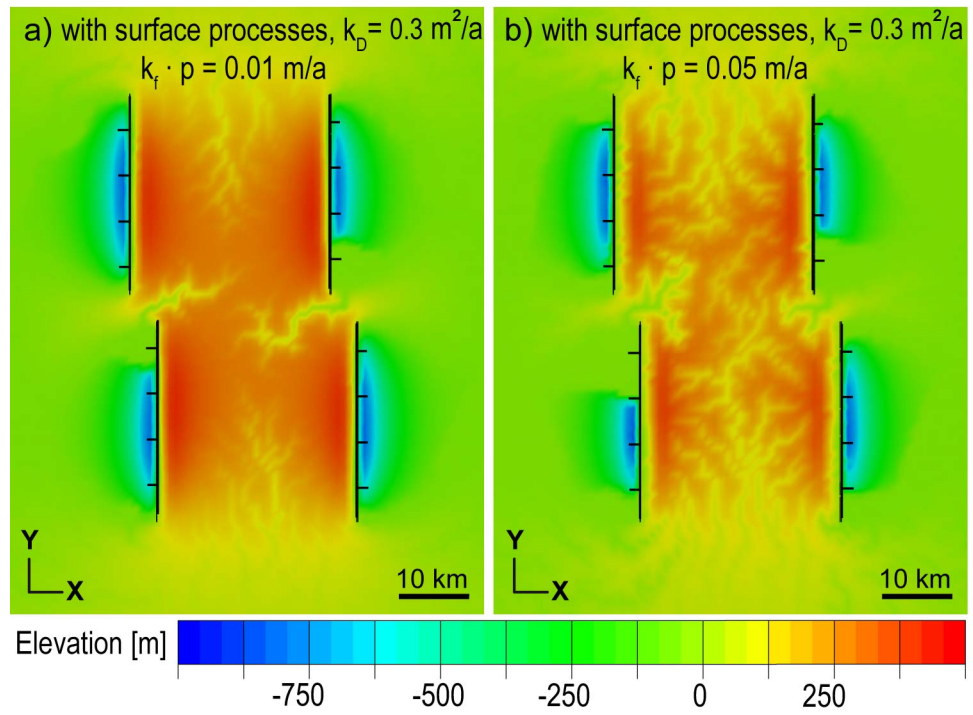


Figure 24: Central part of the model surface at 2.4 Ma of model time for diffusion constant $k_D = 0.3 \text{ m}^2/\text{a}$ and with fluvial erosion constant *a*) 0.01 m/a and *b*) 0.05 m/a.

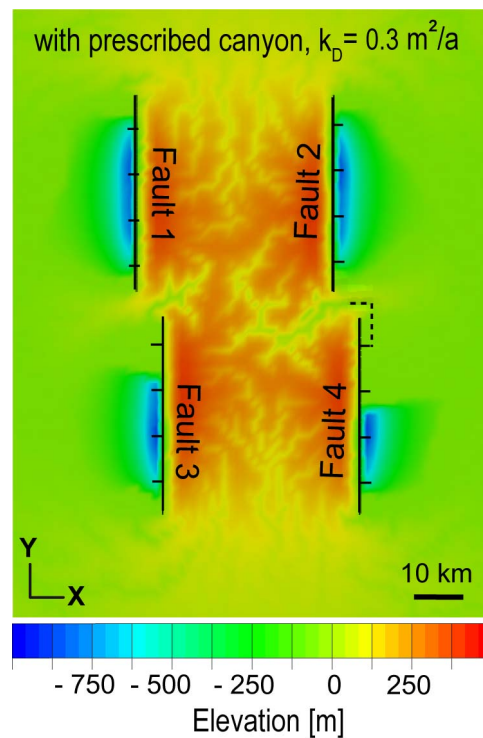


Figure 25: Central part of the model surface at 2.4 Ma of model time for diffusion constant $k_D = 0.3 \text{ m}^2/\text{a}$ and prescribed canyon between faults 2 and 4 (dashed black line). The fluvial erosion constant is 0.03 m/a.

Chapter 4

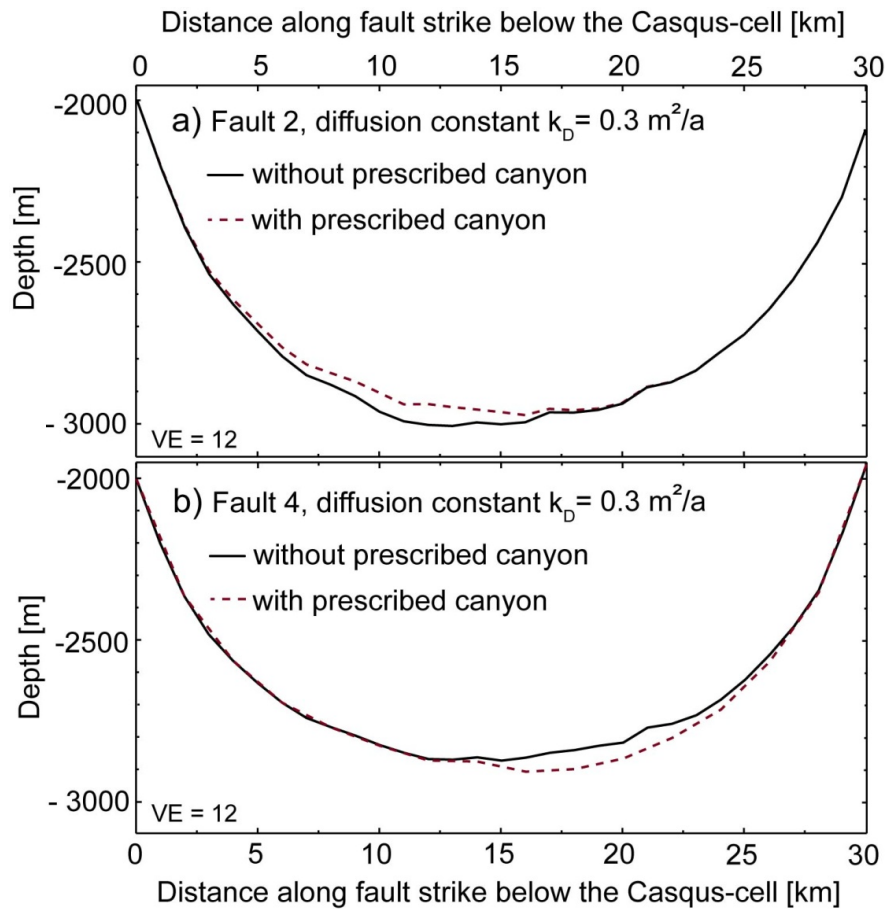


Figure 26: Paths along the fault in the hanging wall at around 2 km depth below the Casqus layer at 2.4 Ma of model time for diffusion constant $k_D = 0.3 \text{ m}^2/\text{a}$ with and without a prescribed canyon between faults 2 and 4. *a)* Effect of the predefined river on the hanging wall of fault 2. *b)* Effect on the hanging wall of fault 4. The black lines correspond to the model run without predefined canyon and the dashed red lines indicate the resulting path along the fault for model runs with prescribed canyon between faults 2 and 4. The vertical exaggeration (VE) is 12. The fluvial erosion constant is 0.03 m/a.

In the model run with the prescribed canyon the sediment flow is redirected into the hanging wall basin of fault 4, where the additional fault displacement results in around 11 m (*Table 4.1, Figure 25*). In contrast to that the fault slip accumulation of fault 2 is decreased by 23 m when compared with the model run without predefined river. It is to note that the fault slip accumulation is derived from the middle of the fault in the hanging wall at 2 km depth for each fault. Since some hanging wall basins are subject to asymmetrical loading the highest fault displacement is shifted towards the river mouth supplying the basin with sediment. This is illustrated for faults 2 and 4 in *Figure 26* showing the paths along the fault at 2 km depth. The prescribed canyon leads to an additional fault displacement of 62 m for fault 4 while fault 2 accumulates around 65 m less fault slip. This observation is confirmed by the amounts of erosion and sedimentation shown in *Table 4.2*. In the presence of the

Chapter 4

prescribed river the total amount of sedimentation is increased by 74 m in the model run with diffusion constant $k_D = 0.3 \text{ m}^2/\text{a}$ for the hanging wall of fault 4 and decreased by 73 m for fault 2.

Fault array with 6 faults

The model surface in *Figures 27a-c* and the corresponding profiles in *Figures 27d-f* show that the overall patterns of erosion, deposition and river network reflect the symmetry of the fault array in the end of a model run for all diffusion constants. The sediment supply from a footwall into a hanging wall of an adjacent fault leads to formation of alluvial fans, which are indicated by red arrows in *Figure 27a-c*. In the reference model with diffusion constant $k_D = 0.3 \text{ m}^2/\text{a}$ (*Figure 27b*), there are some smaller rivers incising the model surface between faults 1 and 2. The highest area adjacent to footwall of fault 2 is wider, higher and steeper than at fault 1 but the hanging wall basin is smaller since it has been filled with sediments mostly from the footwall of fault 4. In the middle of the horst between faults 3 and 4 the model surface is cut by some relatively wide valleys. Sediments from the footwall 1 and 6 have been transported into hanging wall basin of fault 3 and 4, respectively. At last, between faults 5 and 6 the landforms are sinuous and the highest area on the footwall of fault 5 is wider than on the footwall of fault 6. Similar to faults 1 and 2 the hanging wall basin of fault 5 is smaller than for fault 6 due to additional sediment flow from footwall 3. The elevation on the footwall 5 is higher and wider than for fault 6, which in contrast has a wider hanging wall basin. *Figures 27c-f* show the effect of increasing diffusion constant k_D , i.e. diffusion constant k_D is set to $0.5 \text{ m}^2/\text{a}$. The landscape becomes smoother and the valleys are less branched than in the reference model. The elevation on each footwall is slightly lowered and the highest point is moved away from the fault scarp. The hanging wall basins are in general less deep. The change in the morphology on the model surface is most pronounced in the footwall of fault 5 and fault 2, where the morphology becomes less steep as seen in profiles *27d* and *f* and the canyons disappear in the vicinity of the fault scarp. While the hanging wall basin of fault 6 widens, the rim of the hanging wall basin of fault 1 is shifted towards the depression. For diffusion constant $k_D = 0.1 \text{ m}^2/\text{a}$ the number of small rivers cutting the footwall increases (*Fig. 27a, d-f*) The valleys are narrowed and deepened. In general, the landscape becomes steeper and the hanging wall basins narrower. The highest points in each footwall are lifted.

The difference between model runs with and without surface processes for each fault show that surface processes lead to accelerated fault slip (cf. *Maniatis et al., 2009*). It is also shown that for all faults the fault slip increases with increasing diffusion constant k_D . In general, faults 1 and 6 experience the lowest fault displacement in all model runs, the total slip accumulation varying from 1124 m without surface processes to around 1284 m with diffusion constant $k_D = 0.5 \text{ m}^2/\text{a}$. Since faults 3 and

Chapter 4

4 are comparable with the central parts of a segmented fault their fault displacement results in around 1167 m - 1319 m and is hence the highest and very close to each other in each model run (*Cowie and Roberts, 2001; Roberts et al., 2002*). It is also shown, that faults 1 and 5 generally obtain a higher displacement than the opposed faults 2 and 6, respectively. There is also a reversed correlation between the four faults representing the edges of the array. Fault 1 that has no relay ramp inclined into its hanging wall accumulates less fault slip than fault 5 which is the other distal member of the left stepping array but has such a ramp. Fault 2 that also is a distal member of the array and has a relay ramp inclined towards its hanging wall experiences faster fault slip than fault 6. These findings from model runs with and without surface processes indicate that the evolution of individual faults depends on the position in a fault array. Faults 3 and 4 have the same characteristics in terms of relay ramps and both are at the centre of the fault array. Therefore, only the distal faults 1, 2, 5 and 6 are taken into account for further evaluation of the results since they provide better opportunity to investigate the effect of the fault position.

Both erosion and sedimentation increase for all faults with increasing diffusion constant k_D (*Table 4.4*). For all diffusion constants k_D , fault 6 experiences more erosion on the footwall than sedimentation on the hanging wall. In contrast, the sediment accumulation on the hanging wall of fault 5 exceeds the amount of erosion in the footwall. When the diffusion constant k_D is set to $0.1 \text{ m}^2/\text{a}$, the sedimentation rates are lower than the amount of erosion for faults 1, 2 and 6. An inverted effect is observed for diffusion constants $k_D = 0.3 \text{ m}^2/\text{a}$ and $k_D = 0.5 \text{ m}^2/\text{a}$, where the sedimentation exceeds the erosion rates for all faults. The reason is the increased sediment supply from the footwalls into the adjacent hanging wall basins due to evolved river network. An important note is that since material is allowed to leave the model via boundaries, not all of the eroded material from the footwall is deposited in the hanging wall basins.

The model runs with a prescribed river from footwall of fault 4 into the hanging wall basin of fault 6 corroborate the results of models without prescribed canyon. The presence of the induced canyon leads to increased erosion in the footwall of fault 4 and the erosion of the footwall of fault 6 remains less affected (*Table 4.4*). In addition, instead of sediment transport into the hanging wall basin of fault 4, the predefined canyon redirects the flow of sediments throughout the model run into the hanging wall basin of fault 6. The model surfaces for different diffusion constants k_D in the end of the model run and the corresponding profile for diffusion constant $k_D = 0.3 \text{ m}^2/\text{a}$ are shown in *Figure 28b* and *d*. The results show that for the model run with an induced canyon and diffusion constant $k_D = 0.3 \text{ m}^2/\text{a}$ more than half of the hanging wall basin of fault 6 is filled with large amounts of sediments from footwall of fault 4. This leads to rather asymmetric loading of the hanging wall basin of fault 6.

Chapter 4

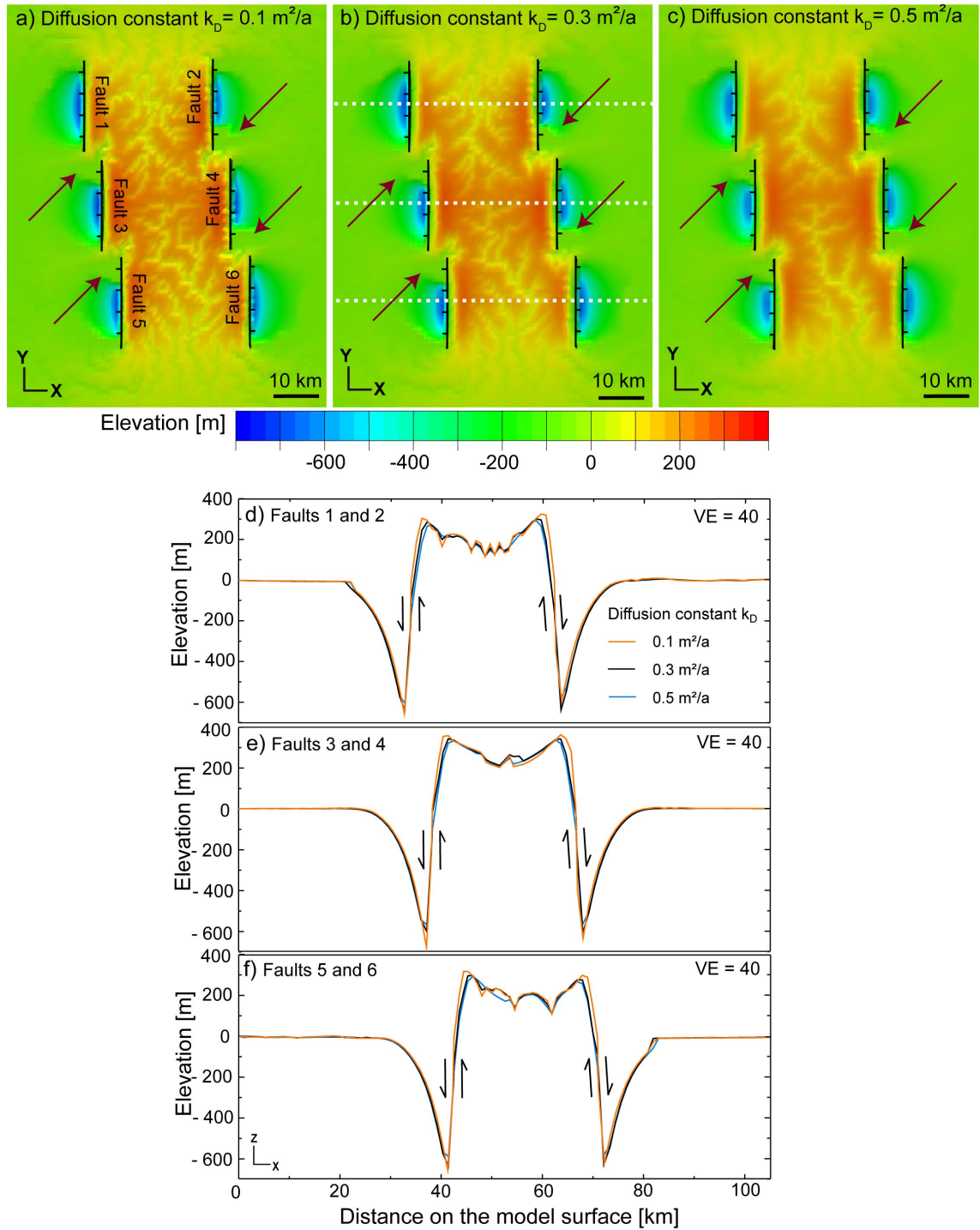


Figure 27: Central part of the model surfaces at 2.4 Ma of model time for different diffusion constants k_D are shown in *Figures a - c*. *a)* Diffusion constant $k_D = 0.1 \text{ m}^2/\text{a}$, *b)* diffusion constant $k_D = 0.3 \text{ m}^2/\text{a}$ and *c)* diffusion constant $k_D = 0.5 \text{ m}^2/\text{a}$. *Figure a)* also illustrates the disposition of the faults in the array. *b)* Shows the position of the profiles illustrated in *Figures d-f*. The alluvial fans that are generated in all model runs are indicated by red arrows. The profiles on the model surface at 2.4 Ma of model time for different diffusion constants k_D are shown in *Figures d-f* where the orange line corresponds to diffusion constant $k_D = 0.1 \text{ m}^2/\text{a}$, the black line represents the diffusion constant $k_D = 0.3 \text{ m}^2/\text{a}$ and the blue curve shows the profile for experiments with diffusion constant $k_D = 0.5 \text{ m}^2/\text{a}$. The vertical exaggeration (VE) is 40. The mode of movement is indicated by black arrows.

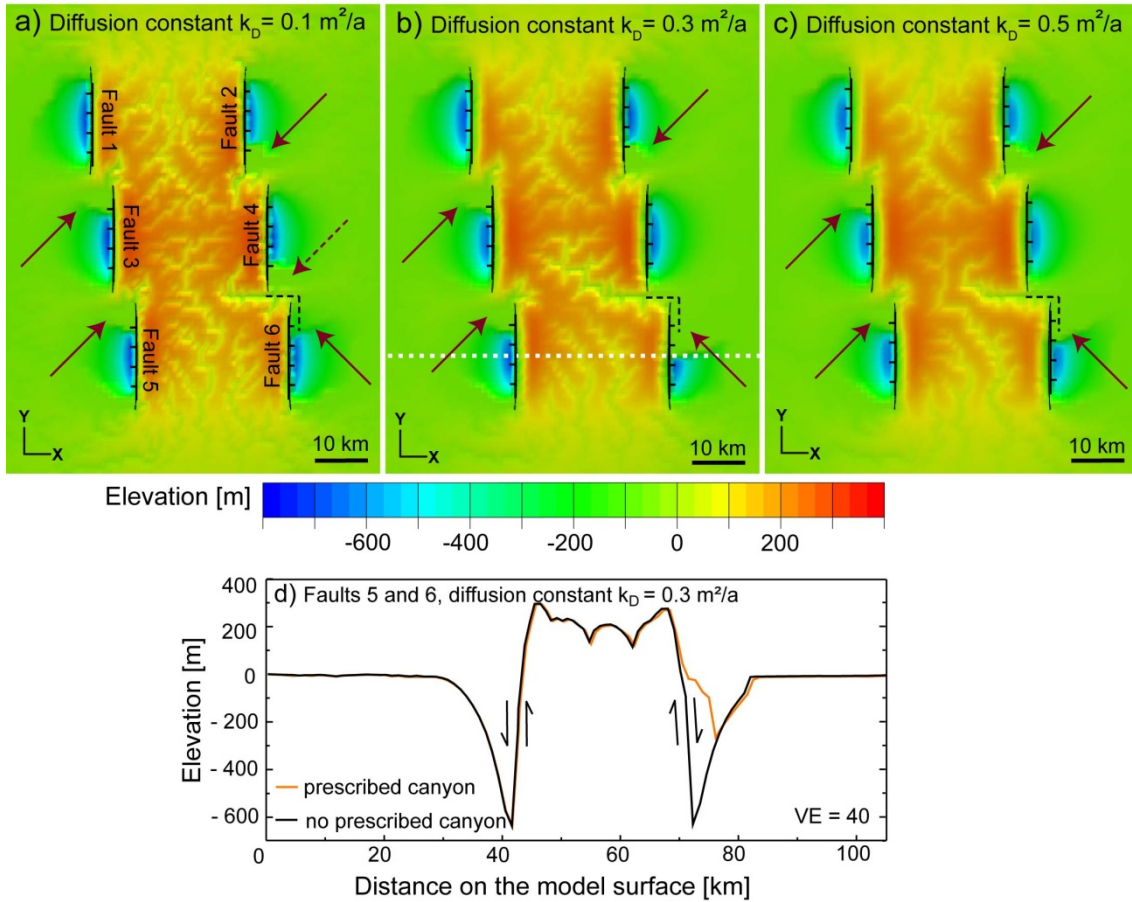


Figure 28: Central part of the model surfaces at 2.4 Ma of model time with a prescribed canyon between faults 4 and 6 (dashed black line). *a)* Model surface for diffusion constant $k_D = 0.1 \text{ m}^2/\text{a}$, *b)* for diffusion constant $k_D = 0.3 \text{ m}^2/\text{a}$ and *c)* for diffusion constant $k_D = 0.5 \text{ m}^2/\text{a}$. *d)* Profiles on the model surface cutting faults 5 and 6 at 2.4 Ma of model time for diffusion constant $k_D = 0.3 \text{ m}^2/\text{a}$. The orange profile indicates the model run with predefined river between faults 4 and 6, the black curve shows the resulting profile for the model run without prescribed canyon. The vertical exaggeration (VE) is 40. The major alluvial fans feeding the hanging wall basins are indicated by red arrows. The position of the profile on the model surface is marked by the dashed white line in Figure *b*.

The fault slip accumulation in the middle of the fault at 2 km depth amounts to around 16 m more than in a model run without prescribed canyon. Due to non-uniform loading of the hanging wall of fault 6 the highest fault displacement is shifted towards fault 4 and results in 25 m which is illustrated in *Figure 29*. These amounts of additional displacement correspond to around 20 to 30 earthquakes of magnitude 6 when the fault is considered to show stick slip behaviour. The fault slip accumulation is in accordance with the total amount of sedimentation, which is almost doubled from around 92 m to some 179 m, when the canyon is induced (*Table 4.4, Figure 28d*). For diffusion constant $k_D = 0.5 \text{ m}^2/\text{a}$ and $k_D = 0.1 \text{ m}^2/\text{a}$ the fault slip in the middle of the fault at 2 km depth is barely affected by mass

Chapter 4

redistribution due to the prescribed canyon since the sediment filling in the hanging wall of fault 6 does not reach the centre of the hanging wall basin (*Figure 28a, c; Figure 29a, c*). Thus, the highest fault slip accumulation of fault 6 is shifted towards fault 4 and results in around 13 m for diffusion constant $k_D = 0.1 \text{ m}^2/\text{a}$ and 12 m for diffusion constant $k_D = 0.5 \text{ m}^2/\text{a}$. Also fault 4 is affected, since the erosion on the footwall increases and the sediment accumulation in the hanging wall basin decreases but the fault slip rate remains the same than for the model run without prescribed canyon. The change in loading of the hanging wall of fault 4 leads to only marginal lateral shifting along strike of the maximum fault slip accumulation at the end of the model run for all diffusion constants k_D (*not shown*).

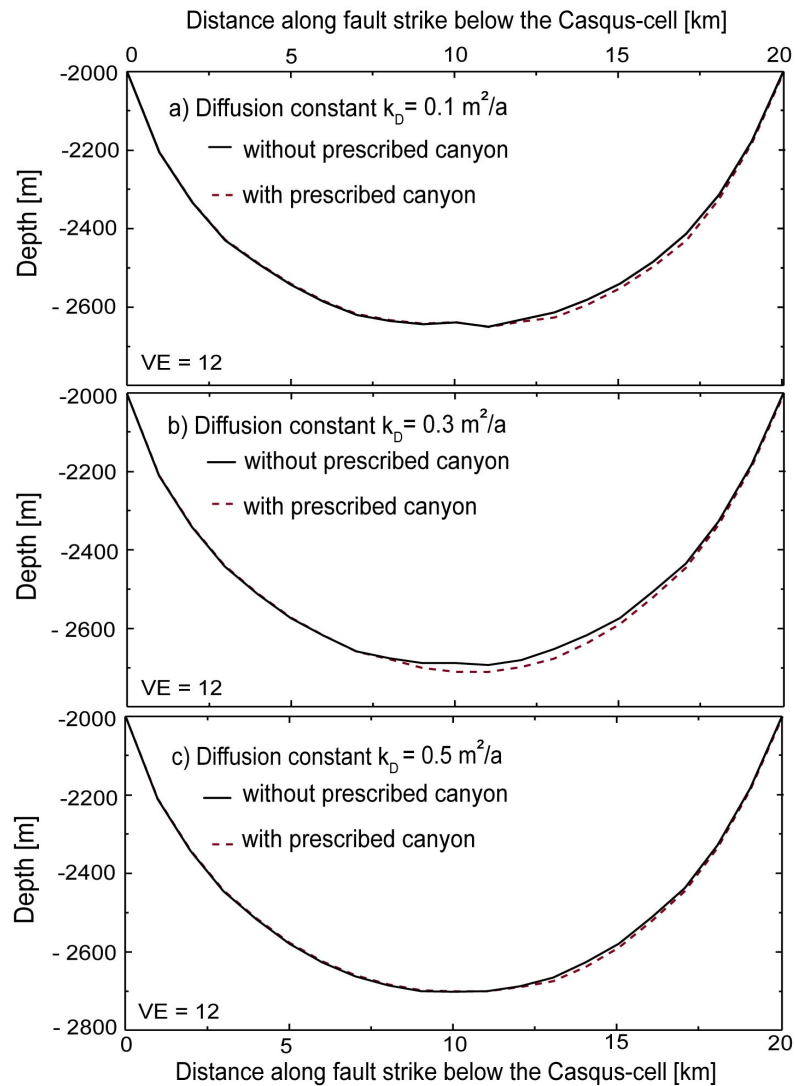


Figure 29: Paths along the fault strike in the hanging wall of fault 6 at 2 km depth at 2.4 Ma of model time for different diffusion constants k_D with and without a prescribed canyon between faults 4 and 6. *a)* shows the effect of the prescribed canyon in a model run with diffusion constant $k_D = 0.1 \text{ m}^2/\text{a}$, *b)* with diffusion constant $k_D = 0.3 \text{ m}^2/\text{a}$ and *c)* with diffusion constant $k_D = 0.5 \text{ m}^2/\text{a}$. The vertical exaggeration (VE) is 12.

Chapter 4

Similar to the experiments with an array of 4 normal faults the fluvial erosion constant affects the model surface by decreasing and increasing the number of streams. The effect is shown in *Figure 30*. For lower fluvial erosion constant (*a*) the footwall is incised by only a few rivers, for higher fluvial erosion constant (*b*) the rivers become branched and they propagate towards the centre of the horst. The sediment flow towards the hanging wall basin of faults 2, 3, 4 and 5 increases for higher fluvial erosion constant, which is obvious from *Figure 30b* and *Table 4.4*.

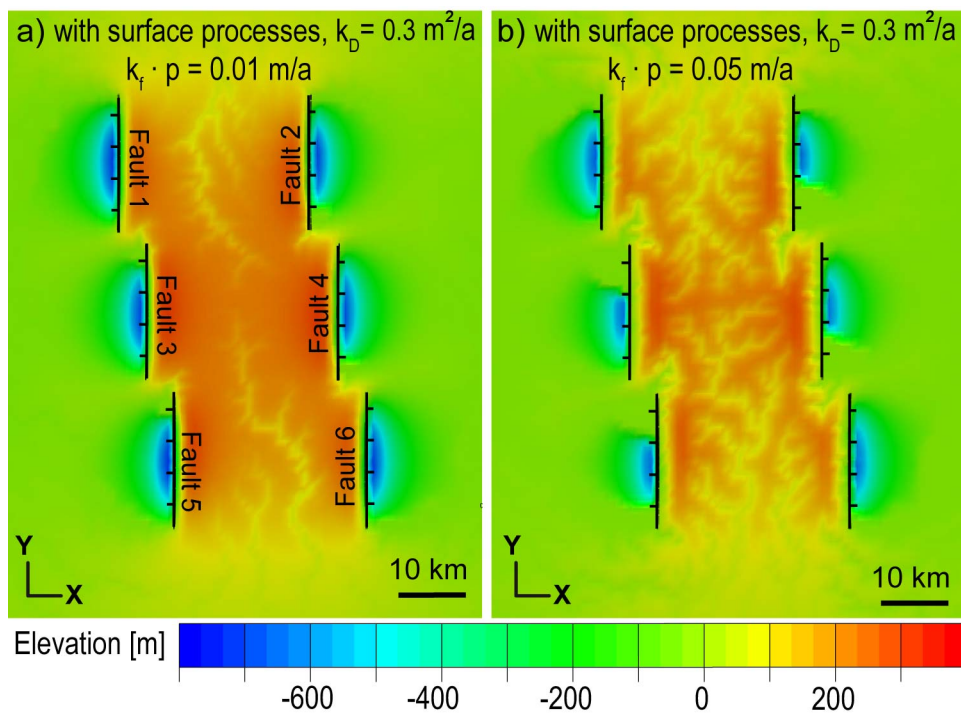


Figure 30: Central part of the model surface at 2.4 Ma of model time for diffusion constant $k_D = 0.3 \text{ m}^2/\text{a}$ and with fluvial erosion constant *a*) 0.01 m/a and *b*) 0.05 m/a.

The changes in erosion and sedimentation rates should affect the stress state in the crust which, in turn, may have an impact on the fault slip evolution. To investigate this, the differential stress was determined for an element in the middle of the fault at around 3 km depth and 1 km away from the fault plane in the footwall. Due to fault geometry the element in the footwall is partly situated below the hanging-wall basin. The differential stress derived from this element coincides with the fault slip accumulation, e.g., the differential stress at the element in the footwall increases with increasing fault displacement in the hanging wall. The evolution of the differential stress for faults 1, 2, 5 and 6 is illustrated for diffusion constant $k_D = 0.3 \text{ m}^2/\text{a}$ in *Figure 31*. The fastest increase of differential stress is derived for fault 5, which also has the highest fault slip accumulation at the end of the model run (*Table 4.3*), when

Chapter 4

only the distal faults are taken into account. The lowest differential stress and the lowest fault displacement are achieved by fault 6. From *Table 4.3* and *Figure 31* it is obvious that fault 2 receives higher differential stress and fault slip than fault 1.

Comparison between the models with and without prescribed canyon shows that the change of the highest fault slip accumulation in the middle of the fault for some hanging wall basins is relatively small but shifted due to non-uniform slip distribution along fault induced by inhomogeneous spatial distribution of sediments (*Figures 26* and *29*). Since the cumulative amounts of erosion in the footwall and sedimentation in the hanging wall are averaged over specific areas they do not consider local variations of sediment distribution. It is also to note that the mesh density in the model is rather rough to be able to determine changes in the stress field caused by relatively small local changes of loading.

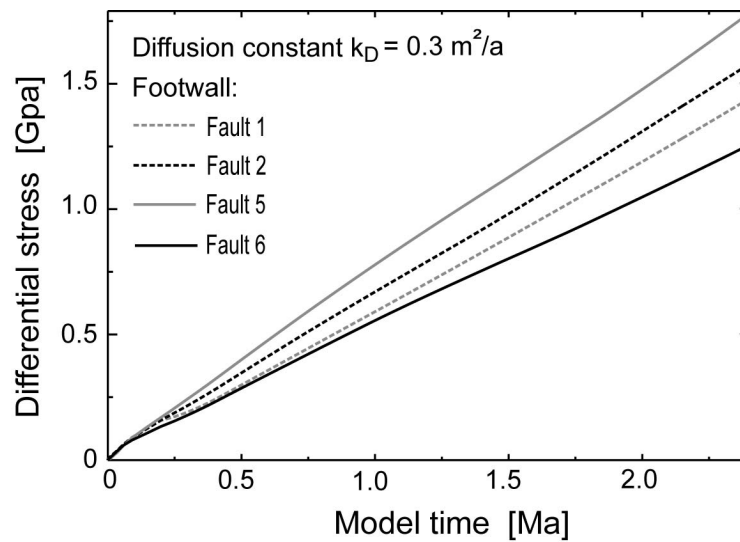


Figure 31: Complete evolution of differential stress in an element in the footwall of the distal faults 1, 2, 5 and 6 for the model run with diffusion constant $k_D = 0.3 \text{ m}^2/\text{a}$. The dashed grey line represents the evolution of the differential stress for fault 1, the dashed black line for fault 2, the grey line indicates the differential stress evolution for fault 5 and the black line for fault 6.

Fault slip evolution after cessation of extension

Since the effect of surface processes on a fault array during active extension is shown, the next step is to investigate further effects of surface processes on fault slip when the far-field extension is stopped but erosion and sedimentation remain active. Model runs were performed for the horst structure with 6 faults for all diffusion constants k_D . The point in time for the end of far-field extension was determined from model runs without prescribed canyon executed for the study described above. By using the fault scaling law $D_{\max} = 0.03L^{1.06}$ after *Schlische et al. (1996)* ($D_{\max} =$

Chapter 4

maximum natural displacement, L = fault length in metres) the end of far-field extension was set at 2.02 Ma of model time, where the 20-km-long faults reach the natural amount of cumulative displacement. The model runs converge for around 70 ka - 560 ka, depending on the diffusion constant k_D . The model run for diffusion constant $k_D = 0.1 \text{ m}^2/\text{a}$ in *Figure 32a* shows that the fault slip accumulation continues throughout the model run. The highest amount of more than 11 m additional displacement after cessation of far-field extension is obtained by faults 2 and 5. Fault 1 and 6 show a mirrored behaviour by accumulating fault slip up to around 9 m. Thus, in contrast to the study above with continuous extension the highest fault slip accumulation after the end of far-field extension seems not to be obtained by faults 3 and 4 in the middle of the array.

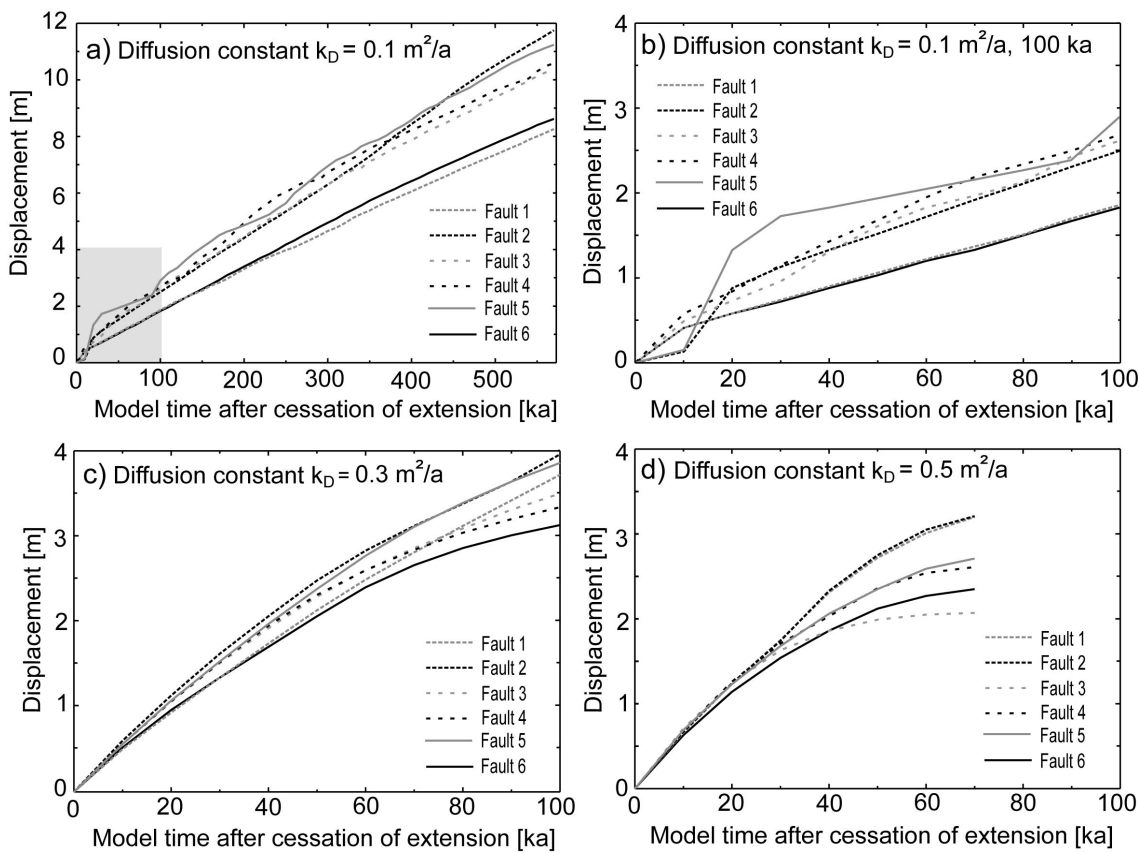


Figure 32: Fault slip evolution after cessation of extension for different diffusion constants k_D . Note that the model runs converged for different time spans and therefore have different scales. *a)* Model run with diffusion constant $k_D = 0.1 \text{ m}^2/\text{a}$ for 570 ka. The grey area indicates the curves until 100 ka after the end of far-field extension shown in figure *b)*. The corresponding results for diffusion constant $k_D = 0.3 \text{ m}^2/\text{a}$ are shown in figure *c)*. *d)* Fault slip evolution for diffusion constant $k_D = 0.5 \text{ m}^2/\text{a}$.

To compare the results of this model run with the results from the model runs with diffusion constant $k_D = 0.3 \text{ m}^2/\text{a}$ (*Figure 32c*) and $0.5 \text{ m}^2/\text{a}$ (*Figure 32d*), the first 100

Chapter 4

ka of the model run are also shown in *Figures 32b-d*. From these diagrams it is clear that although the model run with the lowest diffusion constant $k_D = 0.1 \text{ m}^2/\text{a}$ leads to temporary decrease of the fault slip rates immediately after the cessation of extension the fault slip accumulation generally cease earlier for higher diffusion constant k_D . For example, for diffusion constant $k_D = 0.5 \text{ m}^2/\text{a}$ the fault slip accumulation of all faults is decelerated already from around 40 ka after cessation of extension (*Figure 32d*). Due to the very slow fault slip rate the amount of displacement does not reach the fault displacement accumulated with diffusion constant $k_D = 0.3 \text{ m}^2/\text{a}$, which is shown in *Figure 32c*. The decrease in fault slip rates for diffusion constant $k_D = 0.3 \text{ m}^2/\text{a}$ begins for the most faults at around 50-60 ka but is not that pronounced than for diffusion constant $k_D = 0.5 \text{ m}^2/\text{a}$ (*Figure 32d*). In general, the lowest fault slip rate after cessation of extension is obtained for the model run with diffusion constant $k_D = 0.1 \text{ m}^2/\text{a}$. It is also shown that the opposed faults on each side temporarily show similar behaviour when the changes in fault slip evolution are taken into account.

The corresponding changes in the differential stress determined from an element in the footwall for diffusion constant $k_D = 0.1 \text{ m}^2/\text{a}$ and the distal faults 1, 2, 5 and 6 are shown in *Figure 33*. For all faults the differential stress decreases immediately after cessation of far-field extension but the fault slip accumulation continues. The model is not subject to external tensional forces anymore but the stress accumulated during previous extension still resides in the model. Since the fault array consists of weakness zones the differential stress that was built up in the model is reduced by a stress drop in the vicinity of the faults while fault slip accumulation occurs. Although the differential stress apparently decreases, it still remains above the Mohr-Coulomb failure criterion which enables ongoing accumulation of fault displacement. When the evolution of differential stress shown in *Figure 33* is compared with the evolution of fault slip accumulation (*Figure 32a*) it is clear that the changes in both curves coincide. In other words, during rapid stress drop the fault also slips faster. This is obvious especially for faults 2 and 5 where the changes during the model run are the most pronounced. The opposed faults 1 and 6, respectively, evolve at almost constant rates. Due to lack of convergence the models do not reach the point where the differential stress around the faults drops below Mohr-Coulomb failure criterion and the faults are expected lock, as seen for example in the model run without surface processes (*see Chapter 3; Figure 10a*).

On the basis of this study it is shown that the findings can be applied to regions where the main tectonic activity has shifted from one area to another. One natural example is the Gulf of Corinth, where the present-day extension rate is higher in the west than in the eastern part of the Gulf (*Briole et al., 2000; Avallone et al., 2004; Floyd et al., 2010*). However, the eastern part also remains seismically active (e.g. *Jackson et al., 1982*). As the southern coast of the gulf is characterized by a steep morphology enclosing easily erodable lithologies (*Lykousis et al., 2007; Sakellariou et al., 2007*), the high activity of the normal faults in the eastern gulf may be

Chapter 4

supported by the transport of substantial amounts of sediment from the southern graben shoulder into the eastern part. In the present study a similar effect can be observed by comparing the model runs with and without predefined river. Increased sediment flow affects the fault slip accumulation and hence the subsequent activity of the faults concerned.

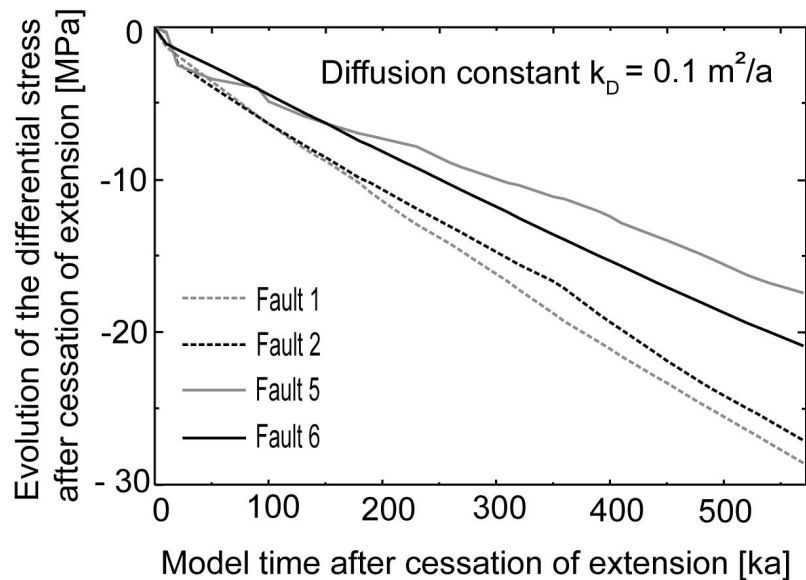


Figure 33: Evolution of the differential stress after cessation of extension for diffusion constant $k_D = 0.1 \text{ m}^2/\text{a}$ and the distal faults 1, 2, 5 and 6. The dashed grey line represents the evolution of the differential stress for fault 1, the dashed black line for fault 2, the grey line indicates the differential stress evolution for fault 5 and the black line for fault 6.

The results from the array with 6 faults also indicate that en echelon faults may behave as a single fault, since the throw is the highest in the central faults and decreases towards the distal faults in the array. This is also the assumption of *Cowie and Roberts (2001)* as well as *Roberts and Michetti (2004)*, when the investigations in the Lazio-Abruzzo region of the central Apennines are considered. In addition, *Roberts and Michetti (2004)* describe this area as a soft-linked array since the faults are not physically linked but still interact with each other both as individual faults and a fault array. This is also the case in the models in the present study, where the faults are not allowed to propagate laterally and thus are prohibited to link with the adjacent faults.

Chapter 4

4.5 Conclusions

Experiments with normal fault arrays indicate that the fault slip evolution depends on the position in an array so that the central faults obtain up to tens of meters more displacement than the distal faults. The increase of diffusion constant k_D leads to higher average sedimentation and erosion rates on each fault subsequently increasing the fault displacement. In general, apart from the central faults there is also an inverse behaviour when the fault slip accumulation and morphology of the en echelon faults on both sides are taken into account. As seen from the experiments with and without a predefined river, changing the amount of sediment flow into the hanging wall basin affects also the maximum fault slip accumulation expected in the centre of the fault. For some faults, this change may be relatively small in the middle of the fault but the highest fault slip accumulation is shifted along strike towards the source of sediments. The determined stress state in the vicinity of the faults after the end of far-field extensions suggests that despite of a stress drop the faults may slip further. The subsequent fault slip evolution coincides with the evolution of the differential stress. The findings concerning the distribution of sediments and fault slip accumulation can be applied to natural complex structures bounded by active normal faults. Hence, the results corroborate the outcome of some earlier studies (*references named in the text*).

5. Blind thrusts: slip behaviour and landscape evolution

5.1 Motivation

After studying the evolution of single normal faults as well as the fault behaviour in arrays, the following investigations evaluate the potential effect of surface processes due to mass redistribution on the earth's surface in the case of crustal shortening and more precisely on blind thrust faults. Blind faults have not yet accommodated enough fault slip to initiate a surface rupture. Sometimes faults remain blind beneath the sediments (e.g. *Hardy and Finch, 2006*). The way by which faults propagate within the rocks depend on the mechanical properties of the surroundings as well as the initial fault geometry such as fault dip and length (*Hardy and Finch, 2006; Albrecht and Lingrey, 2012*). Slip accumulation on blind thrusts may induce a growing fold on the Earth's surface (*Stein and Ekström, 1992; Avouac et al, 1993; Shaw and Suppe, 1994, 1996; Berberian, 1995; Burbank et al., 1996; Cooley et al., 2011; Burrato et al., 2012*). In general, blind faults are widespread in thrust systems (*Dunne and Ferrill, 1988*) and represent a hazard in densely populated areas especially when they remain undetected. Typical cases include the fold-and-thrust belt of the Apennines (e.g. *Burrato et al., 2003; D'Agostino et al., 2011; Burrato et al, 2012; Bonini et al., 2013*), beneath the Los Angeles basin and surroundings (e.g. *Shaw and Suppe, 1994, 1996; Shaw and Shearer, 1999; Pratt et al, 2002; Dolan et al., 2003; Lin and Stein, 2006*), in the East Anatolian region (e.g. *Arpat and Şaroğlu, 1972; Dogan and Karakas, 2013*) as well as beneath the Tibetan plateau and Sichuan basin (e.g. *Xu et al., 2009; de Michele et al., 2010; Jia et al., 2010*).

The Big Bend in the San Andreas fault adjacent to the Mojave Desert is subjected to convergence between the Pacific and North American plate and hence leads to north-south shortening at a rate of 6 mm/a in the Los Angeles area (*Argus et al., 1999*). Therefore, beneath the metropolitan area several thrusts occur that form among others the Compton-Elysian Park blind-thrust system as well as the Puente Hills thrust fault system (*Shaw and Suppe, 1994, 1996; Shaw and Shearer, 1999; Pratt et al., 2002; Dolan et al., 2003; Fuis et al., 2003; Lin and Stein, 2006*) (*Figure 34*). Some of the blind thrust faults are observable as surface folding and estimated to be able to trigger earthquakes of $M_w \sim 6.3$ to more than $M_w 7.0$, either as individual faults or as multiple segments, respectively (*Shaw and Suppe, 1996; Shaw and Shearer, 1999*). Indeed, a prominent earthquake of $M_w 6.0$ occurred in 1987 in Whittier Narrows along the Puente Hills Thrust (e.g. *Dolan et al., 2003*). Most recently also an earthquake of $M_w 6.7$ ruptured in Northridge beneath the San Fernando Valley on a till then unknown blind thrust without previous deformation on the surface. The mainshock occurred at depth of around 18 km on a fault plane dipping at $35\text{-}40^\circ$ (e.g. *Davis and Namson, 1994; Hauksson et al., 1995*).

Chapter 5

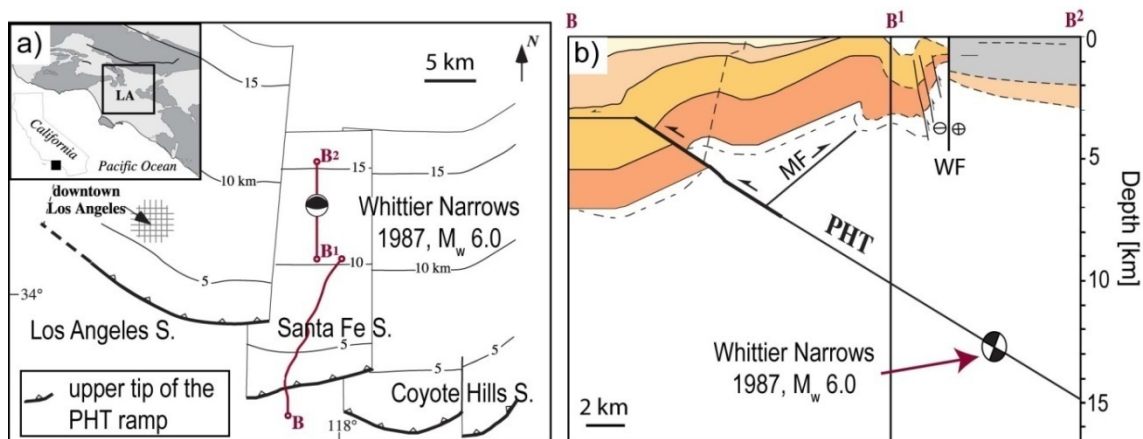


Figure 34: Puente Hills Thrust (PHT) in the Los Angeles area (*modified after Dolan et al., 2003*). Figure *a*) shows the overview of the Los Angeles Area in the small figure and the location of the Puente Hills Thrust in the enlarged figure. The Thrust comprises three segments, which are indicated from West to east as the Los Angeles, Santa Fe Springs and the Coyote Hills segment. The depth of the PHT in each segment is indicated by thin lines. The location of the Whittier Narrows Earthquake is marked on the Santa Fe Springs segment. Red lines indicate the profiles shown in figure *b*. PHT indicates the Puente Hills Thrust, MF refers to the Montebello fault and WF to the Whittier fault.

Another example in a different tectonic setting is provided by the Longmen Shan thrust belt between the eastern Tibetan plateau and the Sichuan basin. The thrust belt is constrained by several faults including relatively shallow (< 10 km) blind thrusts and folds (*Xu et al., 2009; Jia et al., 2010*) (Figure 35). A destructive earthquake of $M_w 7.9$ occurred in 2008 simultaneously along the Yingxiu-Beichuan and Pengguan (*also "Guanxian-Anxian"*) thrust faults inducing fault scarps of ~ 250 km and ~ 70 km length, respectively (e.g. *Xu et al., 2009; de Michele et al., 2010; Jia et al., 2010*). A surface deformation adjacent to the Penguan fault trace is assumed to be generated by a blind thrust during the earthquake (*Xu et al., 2009; de Michele et al., 2010*). *Jia et al. (2010)* also argue that since the crustal shortening in the Longmen Shan thrust belt is not transferred into the western Sichuan basin, it supports the idea of a blind thrust in the eastern front of the thrust belt accommodating the most of the crustal contraction at depth. The modelling results of *de Michele et al. (2010)* corroborate that the observed surface displacements coincide with models including a blind thrust. In their study the blind fault length was varied between 30 -50 km, fault dip from 30° to 70° and the fault top edge depth was set to 2 km - 5 km.

Analogue to the findings described above the aim of the present study was to build a model that exhibits an equivalent surface deformation and landscape evolution. The initial geometry of the fault in the present study was chosen so that it is in accordance with the model setup of *de Michele et al. (2010)*. The fault length of 30 km and the fault dip of 30° set in the model are also similar to the fault dip

Chapter 5

determined for a blind thrust by *Davis and Namson (1994)* and *Hauksson et al. (1995)*. In addition, to investigate the effect of the depth of the fault top edge below the overlaying sediments, the thickness of the Casqus layer above the fault was varied between 1 and 2 km. In the following the evolution of a blind thrust and the adjacent landscape deformation are studied by applying different values of diffusion constant k_D on the model surface for model runs with different depths of the fault top edge.

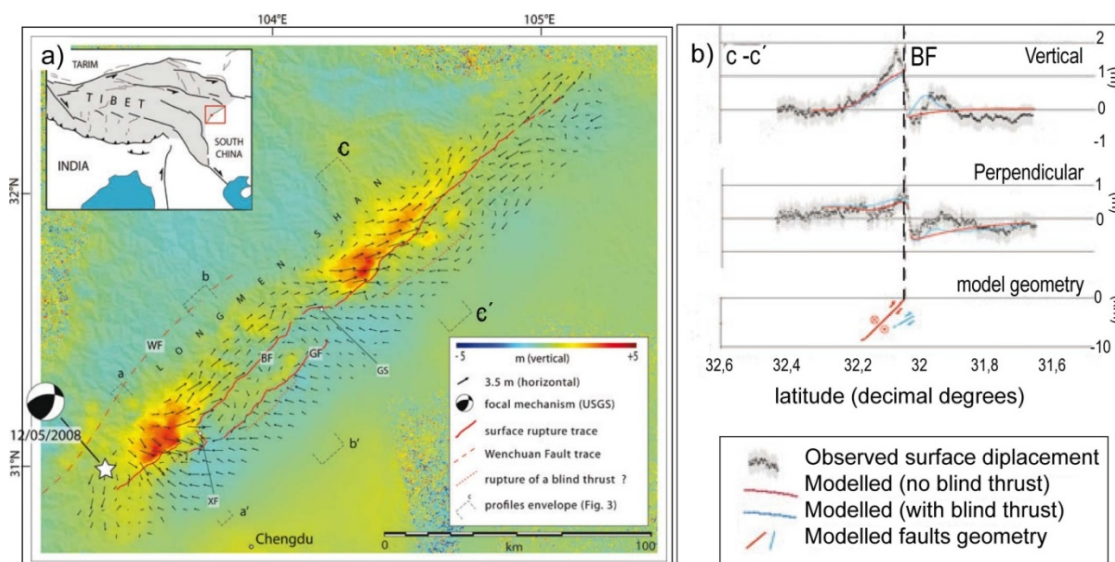


Figure 35: Overview of the Longmen Shan area (*from de Michele et al., 2010*). a) Location of the Longmen Shan and the Sichuan basin as well as the locations of the Earthquake ruptures. BF, Beichuan Fault; GF, Guanxian–Anxian Fault; WF, Wenchuan Fault; XF, Xiaoyudong Tear Fault; GS, Gaochuan Segment. Also the location of the profiles shown in figure b) are indicated by alphabetic characters. b) Pprofile c-c' vertical and perpendicular to fault strike and the corresponding model geometry (*modified after de Michele et al., 2010*).

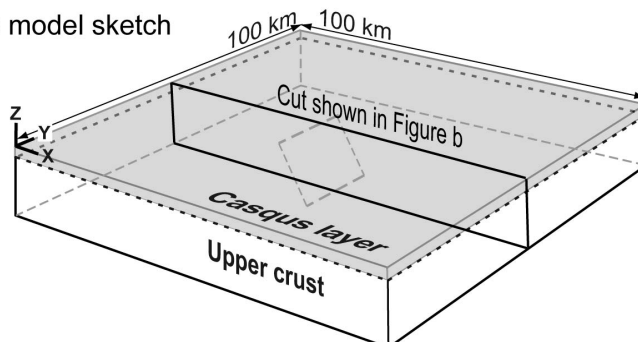
5.2 Model setup

The models consist of a 100 km by 100 km wide lithosphere representing the elastic upper crust (*Figure 36a,b*). To induce thrust faulting, the model is shortened by applying velocity boundary conditions at yz-sides. The total rate of shortening in the model is 4 mm/a (*Figure 36b*). The duration of deformation without surface processes needed to create an initial morphology for the Casqus routine is 100 ka. The setup of the boundary conditions on the bottom of the model as well as on the model surface remains the same as for the models with normal faults. Hence a lithostatic pressure, gravitation and an elastic foundation are applied in an identical way as in the models with normal faults (*see Chapter 2 for details*). The edge size of the mesh-elements in the model decreases from 6000 m on the bottom of the model to 1000 m at the model surface. A 30°-dipping and 30-km-long thrust fault is

Chapter 5

embedded in the middle of the model so that its top edge reaches the bottom of the overlying Casqus cell

a) Overview of the model sketch



b) Cross-section in the middle of the model

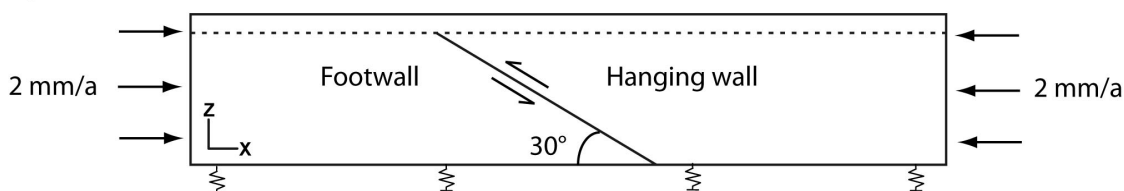


Figure 36: Schematic sketch of the model setup. *a)* The 3D-setup of the model. The boundary conditions remain the same as for the extensional models with exception of the parameters shown in *figure b*. The black rimmed rectangle in the middle of the model marks the cut shown in *figure b*. The boundary conditions on *zy*-sides induce shortening on the model, which is indicated by the black arrows. The 30-km-long blind thrust dips with 30° and the depth of the fault top edge is varied from 1 km to 2 km by using corresponding thicknesses for the Casqus layer.

The thickness of this Casqus layer is varied from 1 km to 2 km in different experiments. To avoid a biased evolution of the river network along straight lines, i.e. element edges, on the model surface the horizontal noise applied on the surface nodes is up to 100 m. The vertical noise of up to 20 m exceeds the vertical noise (2 m) used in the extensional models. This is necessary for the Casqus routine to initiate the simulation of landscape evolution, since there is not any initial rupture on the model surface and hence the initial topography would have been otherwise still too low. A fluvial erosion constant $K_f \cdot p = 0.03$ m/a remains stable in all model runs and hence is used in all experiments described below. This is also the typical reference value throughout the experiments in this thesis.

5.3 Model results

The resulting model surfaces show that a fold grows above the thrust fault with a steep forelimb on the footwall and a shallower backlimb on the hanging wall (*e.g.*

Chapter 5

Figure 38). The morphology above the fault is similar for all model runs with and without surface processes. The general landscape evolution for different diffusion constants k_D shows the same characteristics as in the model runs for normal faults with the exception of the fault slip evolution, which is not affected by the parameters controlling the surface processes. The fault slip evolution determined ~2 km below the Casqus layer is shown in Figure 37 for experiments on a model with 1-km- and 2-km-thick Casqus layer. Note that the model runs ran until ~400 ka and ~800 ka of model time for model runs with a 1-km-thick and 2-km-thick Casqus layer above the blind thrust, respectively.

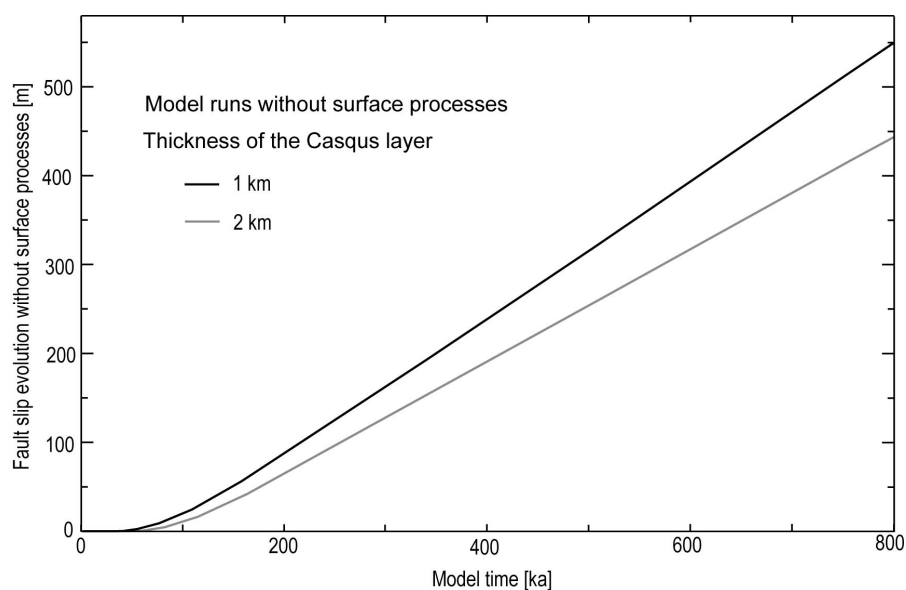


Figure 37: Fault slip evolution ~ 2 km below the Casqus layer for blind thrusts beneath a 1 -km- (black) and 2-km (grey) thick Casqus layer.

Effect of diffusion constant k_D

Table 5.1 shows the cumulative fault slip accumulation at the end of each model run. The fault slip accumulation was derived from a node in the hanging wall in the middle of the fault ~ 2 km below the Casqus layer, i.e. at a depth of 3 km for the 1-km-thick Casqus layer and at a depth of around 4 km for model runs with a 2-km-thick Casqus layer. The model runs without surface processes result in a fault displacement of 551 m for the model with a 1-km-thick Casqus layer and in 446 m for the 2-km-thick Casqus layer after 800 ka. The resulting slip rates are 0.69 mm/a and 0.56 mm/a, respectively. During the same time span and with surface processes the fault displacement for the thicker Casqus layer remains the same as for the model run without surface processes also for all model runs with varying diffusion constant k_D . The model runs with surface processes for a 1-km-thick Casqus layer run until around 400 ka and the fault displacement accumulates at a rate of 0.60 mm/a

Chapter 5

resulting in 239 m irrespectively of the diffusion constant k_D . It is also identical with the fault displacement in the respective model run without surface processes after 400 ka. The corresponding cumulative fault displacement for the 2-km-thick Casqus layer at 400 ka of model time is ~192 m (0.48 mm/a) for model runs with and without surface processes.

Table 5.1: Overview of the total displacement in the middle of the fault after 400 and 800 ka of model time at 2 km depth below the Casqus layer in the hanging wall with and without surface processes. The fault displacement was derived ~ 2 km below the Casqus cell in each model setup, i.e. at a depth of around 3 km and 4 km for the model run with the thinner Casqus layer and thicker Casqus layer, respectively. The fault displacement after 800 ka is indicated by grey italic type. Note that the model with 1-km-thick Casqus layer ran until 400 ka with surface processes. To investigate the potential effect of depth on the fault slip accumulation an additional node for the fault slip was determined for the model with the thicker overburden at a depth of ~3 km below the model surface.

Total fault displacement [m]				
Thickness of the Casqus layer [km]	<i>without surface processes</i>	<i>with surface processes</i>		
		Diffusion constant k_D [m ² /a]		
		0.1	0.3	0.5
1	239	239	239	239
	<i>551</i>	-	-	-
2	192	192	192	192
	<i>446</i>	<i>446</i>	<i>446</i>	<i>446</i>
<i>At 3 km depth below the surface</i>	139	-	139	-
	<i>314</i>	-	<i>314</i>	-

Erosion and sedimentation on the model surface

To evaluate the local landscape formation above the top edge of the blind thrust, the amount of erosion and sedimentation was determined along the profiles on the model surface. The profiles were sub-divided into three 16 km long segments across the surface expression of the blind thrust. These segments represent the forelimb, the backlimb and the hinterland basin. In each segment along the profile 9 points were considered for the evaluation of the cumulative amount of erosion and sedimentation, which implies one point every 2 km per segment within a segment length of around 16 km. The derived mass redistribution on each point for each segment was summed up to obtain the average amount of erosion or sedimentation per segment. The points used for the determination of the amount of sedimentation and erosion along the profile are illustrated in *Figure 38* on an example of the model run with the 2-km-thick Casqus layer after 400 ka. The three segments along the profile (forelimb,

Chapter 5

backlimb and the hinterland basin) are indicated by dashed lines. The nodes used are indicated by black rectangles. The diffusion constant k_D was set at $0.3 \text{ m}^2/\text{a}$ which is the typical reference value throughout the experiments.

Table 5.2 shows the total amounts of erosion and sedimentation for each segment at the end of each model run. The values of erosion are negative, implying removal of material. The erosion on the backlimb vary through time for model runs with both Casqus layer thicknesses but the erosion on the forelimb as well as the sedimentation in the hinterland basin remains relatively constant. For the model setup with the 1-km-thick Casqus layer the average cumulative erosion on the forelimb is -0.4 m and -1 m (-0.001 mm/a and -0.003 mm/a) on the backlimb until 400 ka of model time. The accumulated sedimentation in the hinterland basin amounts to 2 m (0.005 mm/a). After 400 ka the erosion on the forelimb and on the backlimb in the model run with 2-km-thick Casqus layer is -0.4 m and -1.6 m (-0.001 mm/a and -0.004 mm/a), respectively. The sedimentation in the hinterland basin is 2.6 m (0.007 mm/a). When the model run time is extended to 800 ka for the model run with 2-km-thick Casqus layer the total erosion on the forelimb results in -5 m (-0.006 mm/a). The total erosion on the backlimb increases to -13 m (-0.016 mm/a) which is similar to the amount of sedimentation in the hinterland basin resulting in 15 m (0.019 mm/a) along the profile.

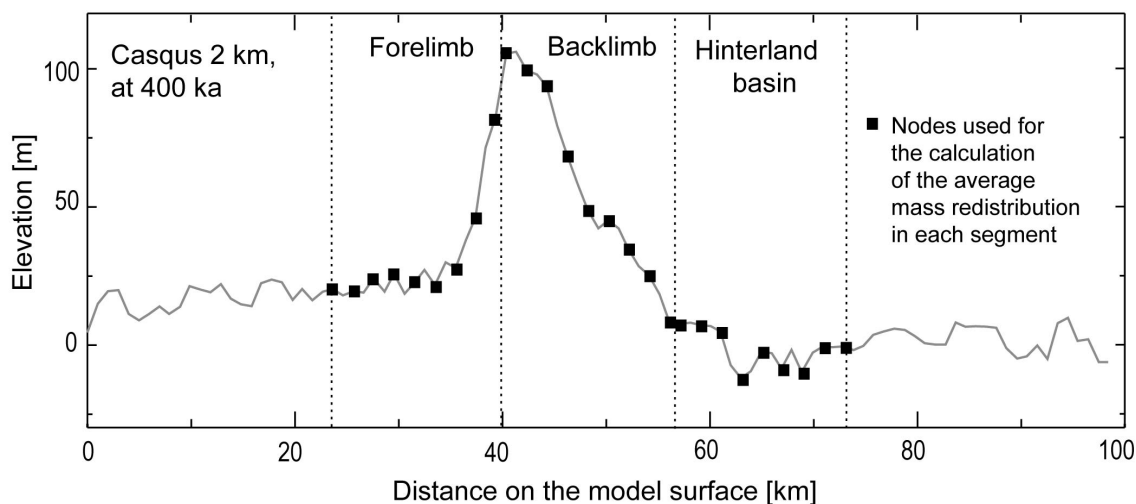


Figure 38: Schematic sketch showing the nodes used (black rectangles) to determine the local effect of erosion and sedimentation along the profiles on the model surface. The example shows the profile at 400 ka with surface processes for the 2-km-thick Casqus layer and diffusion constant k_D is $0.3 \text{ m}^2/\text{a}$. Different segments are marked by dashed lines showing the forelimb, backlimb and the hinterland basin. Note that the axes are not scaled.

Chapter 5

Table 5.2: Overview of the local cumulative erosion and sedimentation along the profiles (*Figure 38*) above the fault for model runs with diffusion constant $k_D = 0.3 \text{ m}^2/\text{a}$ after 400 and 800 ka of model time for 1-km-thick and 2-km-thick layers covering the blind thrust. Negative values represent erosion and the positive values sedimentation. The results for the model runs until 800 ka are indicated by grey italic type. Note that the model with 1-km-thick Casqus layer ran until 400 ka with surface processes.

Average erosion and sedimentation along the profile				
Thickness of the Casqus layer [km]	Model time [ka]	Erosion and Sedimentation [m]		
		Forelimb	Backlimb	Hinterland basin
1	400	-0.4	-1	+ 2
	<i>800</i>	-	-	-
2	400	-0.4	-1.6	+2.6
	<i>800</i>	-5	-13	+15

5.4 Discussion

The models indicate that there is no significant interaction between the surface processes and the fault slip evolution of the blind thrust. The thickness of the Casqus layer above the blind thrust however affects the fault slip evolution and the subsequent surface deformation (*Table 5.1*). *Figure 39* shows the profiles after 800 ka of model time without surface processes for model runs with 1-km- (black curve) and 2-km-thick (orange curve) Casqus layer. Also shown is the position of the top edge of the blind thrust below the overlaying Casqus layer relative to model surface. The location of the fault clearly affects the shape of the subsequent surface deformation. In the model run with the 2-km-thick Casqus layer, the model surface on the footwall bounded by the forelimb is elevated but subsides in the model with the thinner Casqus layer. The hillslope on the forelimb of the latter is also steeper and almost planar in the profile. The fault slip accumulation without surface processes for the model with 1-km-thick Casqus layer is 551 m, which leads to a difference of almost 105 m in fault slip accumulation between the two model setups for different thicknesses of the Casqus layer (*Table 5.1*).

The surface expression of crustal deformation above the blind thrust in the middle of the model is listed in *Table 5.3a* for model runs without surface processes. The values represent the highest and deepest point along the profiles shown in *Figures 39, 41 and 42*, where the deepest point was chosen so that it marks the end of the backlimb. The total vertical extent of the surface deformation above the blind thrust comprises both values. For the thinner Casqus layer, in the model run without surface

Chapter 5

processes the total height of the surface expression is 140 m. The total height of the surface deformation on the thicker Casqus layer amounts to 123 m.

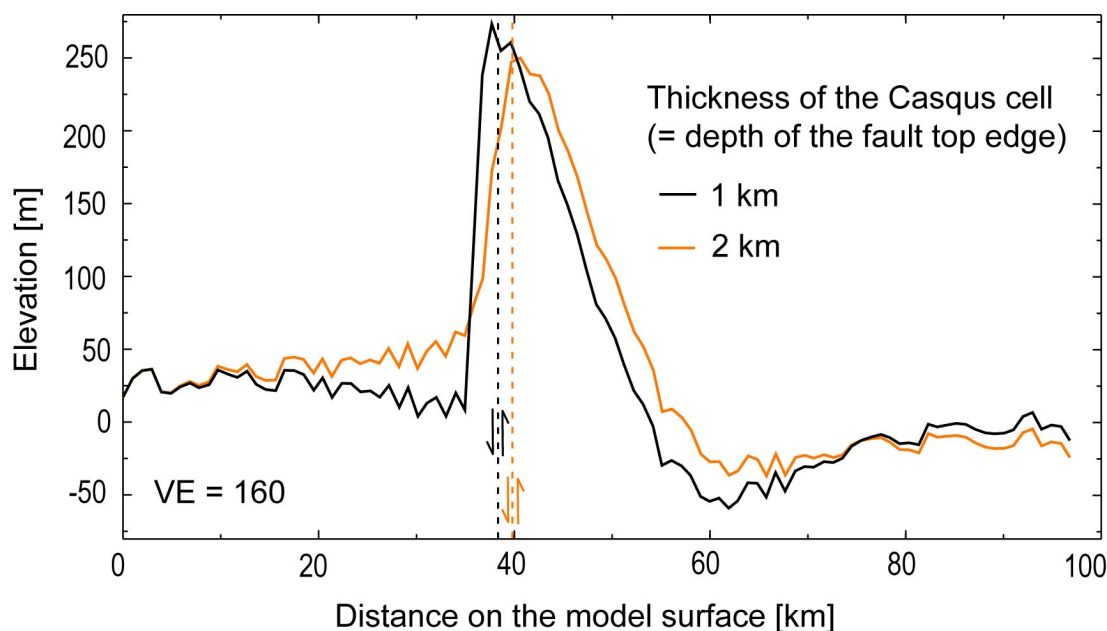


Figure 39: Profiles on the surface in the middle of the model at 800 ka without surface processes for the 1-km thick casqus layer (black) and the 2-km-thick Casqus layer (orange). The position of the blind thrust trace beneath the Casqus layer is indicated by the corresponding dashed lines and the corresponding relative movement is shown by the arrows. Note that the dashed lines do not consider the fault dip and only project the fault trace (fault top edge) on the model surface. The vertical exaggeration is 160.

The model surfaces after 400 ka of model time with surface processes for diffusion constant $k_D = 0.3 \text{ m}^2/\text{a}$ and varying thickness of the Casqus layer are shown in *Figure 39*. It is obvious that the hinterland basin is deeper and larger for the model with 1-km-thick Casqus layer (*Figure 40a*) than for the model with 2-km-thick Casqus layer (*Figure 40b*). The rivers and the river network incising the model surface and propagating towards the anticline are more pronounced for the model with the thicker Casqus layer, as seen in *Figure 40*.

A more detailed view is provided by the profiles in the middle of the model across the fault shown in *Figure 41*. In general, the surface deformation is steeper and more localized for the thinner Casqus layer above the blind thrust also for model runs with surface processes. On the 2-km-thick Casqus layer the model surface is morphologically affected by the fold in the footwall already further away from the forelimb (*Figure 41b*). In addition, the forelimb dips more gently and the morphology is rather rough when compared to the forelimb on the 1-km-thick Casqus layer (*Figure 41a, b*). According to the profiles the highest point is located

Chapter 5

on the backlimb for both 1-km- and 2-km-thick Casqus layers irrespectively of the diffusion constant k_D . For the 1-km- as well as for the 2-km-thick Casqus layer the elevation above the fault in the middle of the model surface experiences a slight decrease with increasing diffusion constant k_D . The highest elevation after 400 ka of model time is obtained by the model run with the thinner Casqus layer where the peak on the model surface results in up to 116 m while the corresponding node for a 2-km-thick Casqus layer reaches up to 106 m (*Table 5.3b*).

Table 5.3: Overview of the surface expression in the profiles (*Figure 39, 41 and 42*) above the fault after 400 and 800 ka of model time for 1-km-thick and 2-km-thick layers covering the blind thrust without surface processes (*a*) and with surface processes for diffusion constant $k_D = 0.3 \text{ m}^2/\text{a}$ (*b*). Crest corresponds to the peak along the profile and the deepest point is located in the hanging wall basin. The vertical extent comprises both values showing the total height of the surface folding. The results for the model run until 800 ka is indicated by grey italic type. Note that the model run with 1-km-thick Casqus layer converged only until 400 ka with surface processes.

a) Topography across the surface fold without surface processes				
Thickness of the Casqus layer [km]	Model time [ka]	Elevation along the profiles [m]		
		Crest	Deepest point	Vertical extent
1	400	118	-22	140
	<i>800</i>	<i>274</i>	<i>-59</i>	<i>333</i>
2	400	109	-14	123
	<i>800</i>	<i>250</i>	<i>-37</i>	<i>287</i>

b) Topography across the surface fold with surface processes ($k_D = 0.3 \text{ m}^2/\text{a}$)				
Thickness of the Casqus layer [km]	Model time [ka]	Elevation along the profiles [m]		
		Crest	Deepest point	Vertical extent
1	400	116	-20	136
	<i>800</i>	<i>-</i>	<i>-</i>	<i>-</i>
2	400	106	-12	118
	<i>800</i>	<i>249</i>	<i>5</i>	<i>244</i>

After 400 ka of model time the hinterland basin for both models with 1-km- and 2-km-thick layers above the blind thrust is bounded by a relatively flat and wide terrace towards the backlimb whereas the basin itself is wider for the thinner covering. The hinterland basin on the thicker Casqus layer is shifted further away from the backlimb due to a wider sediment terrace (*Figure 41b*). The hinterland basin is the deepest for the model runs without surface processes and becomes shallower with

Chapter 5

increasing diffusion constant k_D (Figure 41). In the profiles the deepest point in the hinterland basin is around 19 - 23 m on the model with the 1-km-thick Casqus layer and 13 - 18 m for the model with the 2-km-thick Casqus layer, depending on the diffusion constant k_D . Since the general effect of surface processes on the model surface remains similar for all diffusion constants k_D , Table 3b shows the resulting highest and the deepest points in model runs with surface processes for the diffusion constant $k_D = 0.3 \text{ m}^2/\text{a}$. Note that the models with the 1-km-thick Casqus layer converged only until 400 ka with surface processes and hence are not considered for evaluation of the effect of surface processes for model runs until 800 ka.

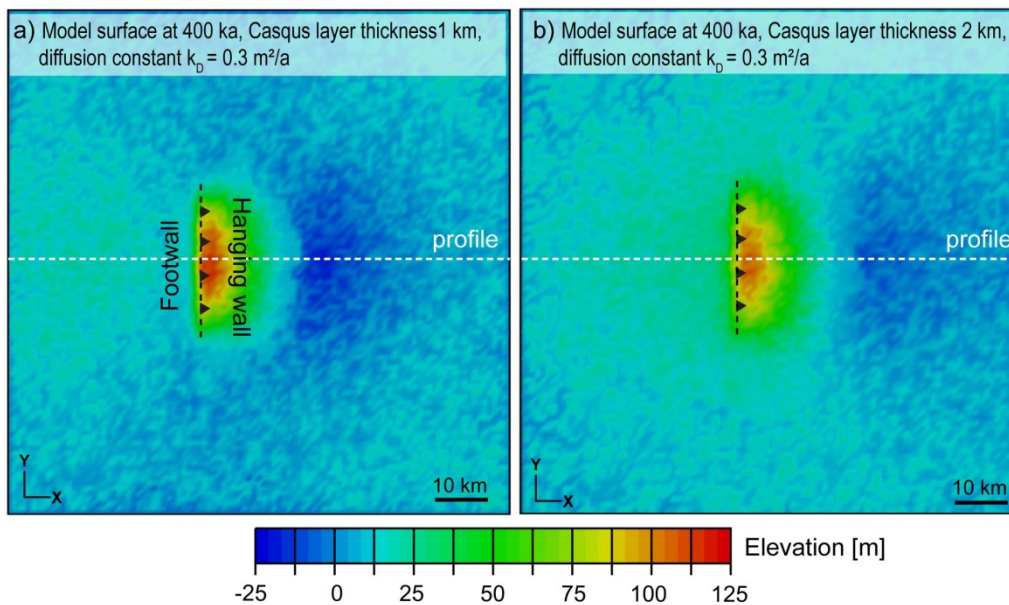


Figure 40: Model surface at 400 ka (a) for 1-km-thick Casqus layer and (b) for 2-km-thick Casqus layer. The diffusion constant k_D is $0.3 \text{ m}^2/\text{a}$ and the fluvial erosion constant $K_f \cdot p$ is set at 0.03 m/a in both model runs. The approximate position of the fault trace below the Casqus layer is indicated by the dashed black lines. The position of the profiles is marked by the white dashed line.

Figure 42 shows the model surface for the 2-km-thick Casqus layer after 800 ka of model time without surface processes (Figure 42a) as well as with surface processes for all diffusion constants k_D used in the present study (Figure 42b-d). As already shown by the study on normal faults the topography on the model surface becomes smoother when diffusion constant k_D increases. This is also the case in the models with blind thrusts. The respective profiles in the middle of the model surface are shown in Figure 43. After 800 ka of model time the highest point on the model surface is around 250 m for model runs with and without surface processes, whereas the highest elevation slightly decreases with increasing diffusion constant k_D . Due to erosion the crest becomes rounded and more symmetric. The surface expression of

Chapter 5

the blind thrust becomes narrower due to erosion of the backlimb, when surface processes are active (*Figure 40*). As seen in the profiles in *Figure 40b*, at 400 ka of model time the hinterland basin on the 2-km-thick Casqus layer is shifted away from the backlimb and becomes narrower when surface processes are active. The profiles in *Figure 43* indicate that at 800 ka of model time the previous hinterland basin is thoroughly filled with sediments which may have their origin on the backlimb. The cumulative amount of erosion on the backlimb (-13 m) along the profile corresponds to the cumulative amount of sedimentation in the hinterland basin (+15 m) are shown in *Table 5.3*.

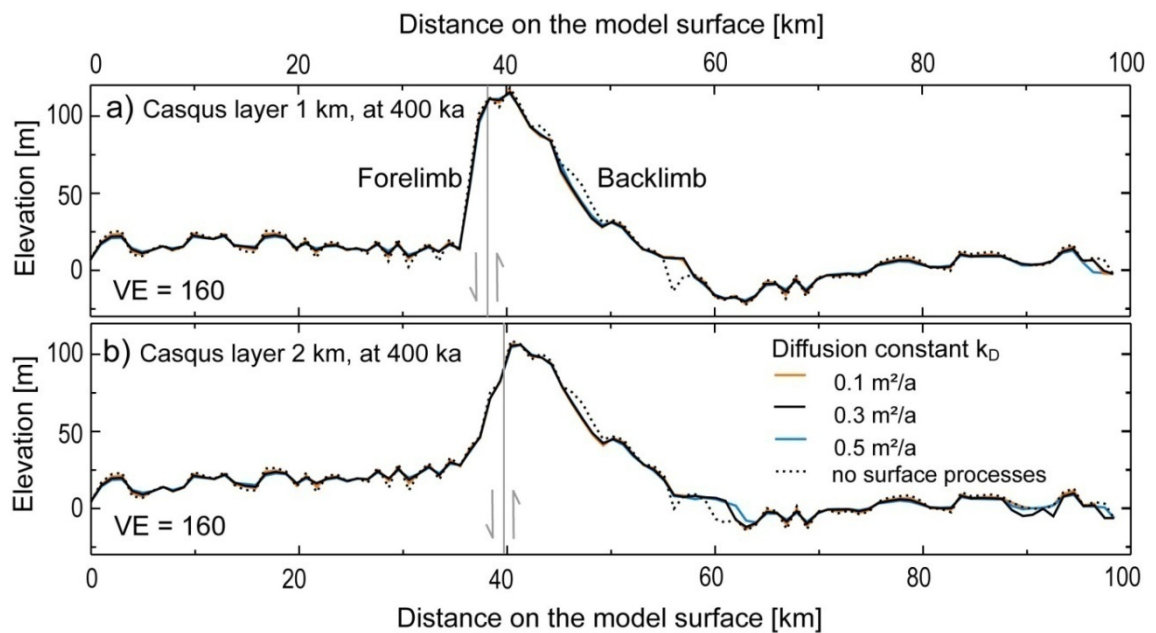


Figure 41: Profiles on the surface in the middle of the model at 400 ka with and without surface processes for the 1-km thick Casqus layer (*a*) and the 2-km-thick Casqus layer (*b*). The diffusion constant k_D is varied from $0.1 \text{ m}^2/\text{a}$ to $0.5 \text{ m}^2/\text{a}$, which is indicated in the legend in *Figure b*. The fluvial erosion constant $K_f \cdot p$ is set at 0.03 m/a in all model runs. The position of the blind thrust beneath the Casqus layer is indicated by the grey line and the corresponding relative movement is shown by the grey arrows. Note that the grey line does not consider the fault dip and only projects the fault trace on the model surface. The vertical exaggeration is 160 in both profiles.

Effect of depth along the fault plane on the fault slip rate

It was observed that for model runs with and without surface processes both the fault slip accumulation and the surface expression for the 1-km-thick Casqus layer the blind thrust exceed the corresponding values of the models with a 2-km-thick covering. The fault slip was derived from a node in the middle of the fault at a depth of $\sim 2 \text{ km}$ below the Casqus layer for each model setup with different thickness of the Casqus layer. Therefore, the fault slip for the model run with 1-km-thick Casqus

Chapter 5

layer was determined ~ 3 km below the model surface and the fault displacement for the 2-km-thick Casqus layer was derived at a depth of ~ 4 km.

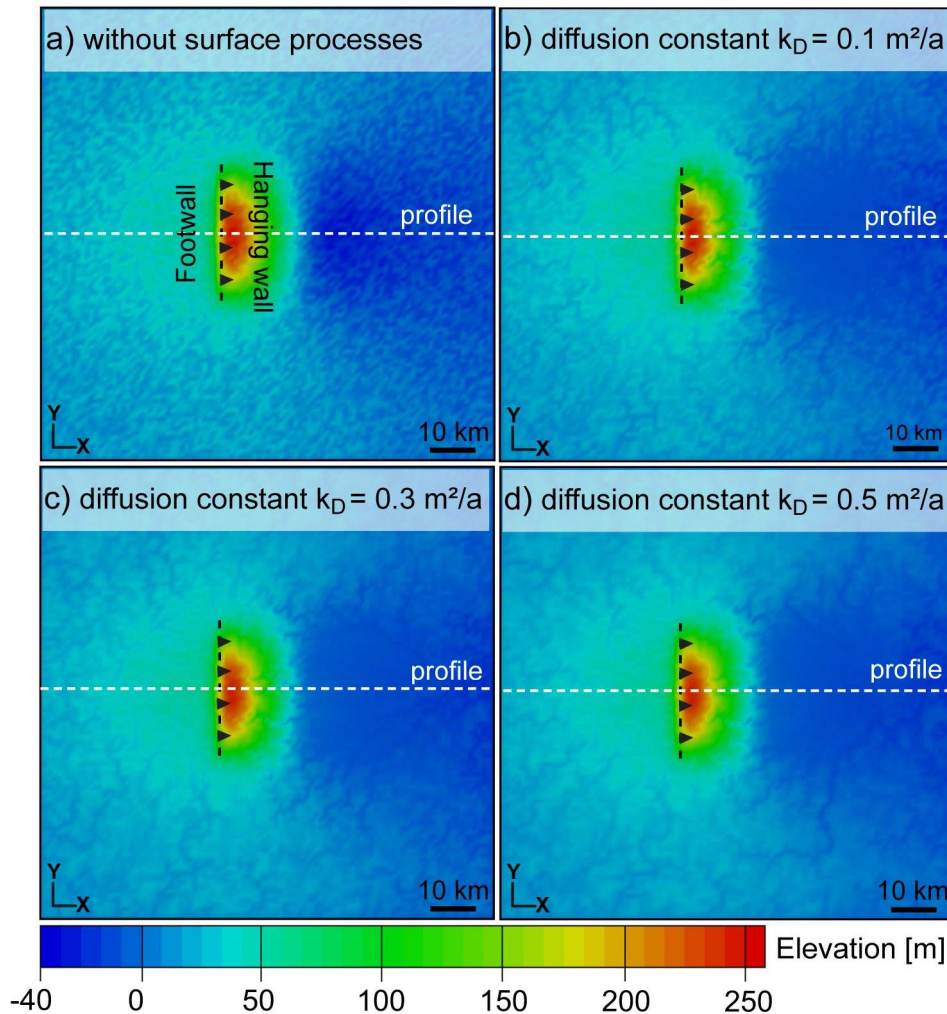


Figure 42: Model surface at 800 ka of model time *a*) without surface processes, *b*) with diffusion constant $k_D = 0.1 \text{ m}^2/\text{a}$, *c*) with diffusion constant $k_D = 0.3 \text{ m}^2/\text{a}$ and *d*) with diffusion constant $k_D = 0.5 \text{ m}^2/\text{a}$. The fluvial erosion constant $K_f \cdot p$ is 0.03 m/a in all model runs. The thickness of the Casqus layer is 2 km. The approximate position of the fault trace below the Casqus layer is indicated by the dashed black lines. The position of the profiles shown in *Figure 42* is marked by the white dashed line.

The model run with a 1-km-thick Casqus layer reaches a displacement of 551 m after 800 ka of model time without surface processes (*Table 5.1*). The corresponding surface fold obtains a peak at 274 m in the profile (*Figure 38*, *Table 5.3a*). In the same time span the model run without surface processes and with the thicker Casqus layer (2 km) accumulates fault slip for 446 m (*Table 5.1*) and the crest of the surface expression reaches ~ 250 m (*Table 5.3a*, *Figure 38*). When in each case the highest (crest) and the deepest point (hinterland basin) along the profiles across the surface

Chapter 5

fold are considered, the total height of the surface fold in the middle of the model is 333 m with the thinner Casqus layer and 287 m for the thicker Casqus layer (*Table 5.3a*).

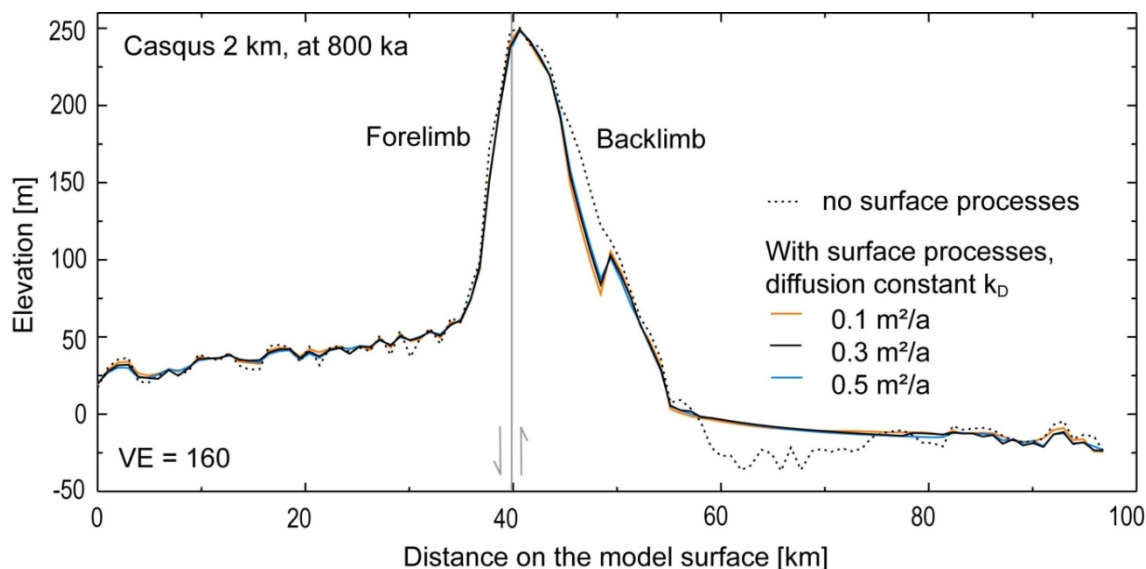


Figure 43: Profiles on the model surface in the middle of the model at 800 ka 2-km-thick Casqus layer. The position of the profiles is shown in Figure 42. The diffusion constant k_D is varied from 0.1 m^2/a to 0.5 m^2/a . The fluvial erosion constant $K_f \cdot p$ is set at 0.03 m/a in all model runs. The position of the blind thrust trace beneath the Casqus layer is indicated by the grey line and the corresponding relative movement is shown by the grey arrows. Note that the grey line do not consider the fault dip and only projects the fault trace on the model surface. The vertical exaggeration is 160.

In summary, in model runs without surface processes the fault slip accumulation after 800 ka for the model run with the 1-km-thick Casqus layer is around 105 m more than the fault displacement for the model run with the 2-km-thick Casqus layer. The difference between the elevation of the surface deformation for the 1-km-thick and 2-km-thick Casqus layer is 47 m, whereas the thinner Casqus layer leads to a higher maximum elevation point on the model surface.

For the model run with surface processes and with the thinner Casqus layer the fault displacement is 239 m and the peak on the model surface is 116 m after 400 ka (*Table 5.1, Table 3b*). The corresponding values for the model run with the thicker Casqus layer amount to a total fault slip accumulation of 192 m and the peak reaches 106 m (*Table 5.1, Table 3b*). Again, if along each profile the highest and the deepest point is considered, the surface displacement obtains a total height of 136 m for the model run with the 1-km-thick Casqus layer and 118 m for the model run with the 2-km-thick Casqus layer (*Table 5.3b*). Hence, in the model runs with surface processes

Chapter 5

the difference in fault slip accumulation is around 47 m and the corresponding difference between the surface deformations is 18 m after 400 ka of model time.

To enable a direct comparison of the fault slip evolution between the two model setups with a different thickness of the Casqus layer, a point at a depth of ~ 3 km below the model surface was selected for both model set ups (1-km- and 2 -km-thick Casqus layer). To do so, an additional point for fault slip was determined for the model with the thicker Casqus layer. The results comprised in *Table 5.1* show that at a depth of ~ 3 km the fault slip accumulation is 239 m beneath the thinner Casqus layer and 139 m for the model run with the thicker Casqus layer after 400 ka and without surface processes. After 800 ka of model time and without surface processes the cumulative fault slip is 551 m for the model with the thinner Casqus layer and 314 m for the thicker Casqus layer. *Table 5.1* shows that the fault slip accumulation at ~ 3 km depth remains the same also for the model run with surface processes and diffusion constant $k_D = 0.3 \text{ m}^2/\text{a}$. Hence, when the fault slip is determined at the same depth along the fault plane in the hanging wall in both model set ups, the fault slip accumulation in the model run with the 1-km-thick Casqus layer is still higher than in the model run with the 2-km-thick Casqus layer. In Summary, when a point at a depth of ~ 3 km is considered, after 400 ka the fault slip accumulation for the model with the 1-km-thick Casqus layer exceeds the corresponding fault displacement of the model run with the 2-km-thick Casqus layer by 100 m. In addition, after 800 ka of model time the fault displacement ~ 3 km below the model surface for the thinner Casqus layer is 237 m more than for the thicker covering.

The results discussed above imply that fault displacement beneath the thinner Casqus layer exceeds considerably the fault slip in the model with a 2-km-thick Casqus layer but the difference in the vertical extent of the associated surface expressions is only a fractional amount of the that difference (*Table 5.3*). The potential reason may be the distribution of the vertical displacement, which is shown in *Figure 44*. The figure shows the vertical displacement in the middle of the model for model runs with surface processes with diffusion constant $k_D = 0.3 \text{ m}^2/\text{a}$ at 400 ka. *Figure 44a* reveals that a part of the highest vertical displacement observed on the model surface above the fault is partially accommodated by the upper wedge of the hanging wall beneath the 1-km-thick Casqus layer. On the contrary, the highest vertical displacement on the 2-km-thick Casqus layer is locally concentrated in the uppermost Casqus layer above the fault tip (*Figure 44b*). The subsidence of the footwall is also more pronounced for the model run with a 1-km-thick Casqus layer. Hence, after 400 ka of model time the elevation on the model surface is induced by the fault slip for the model run with a 2-km-thick Casqus layer but rather restrained beneath the thinner Casqus layer. The distribution of the vertical displacement at 800 ka for the 2-km-thick Casqus layer shown in *Figure 45* is similar to that for the 1-km-thick Casqus layer at 400 ka. This indicates that for a shallower top edge of the blind thrust, i.e. at a depth of 1 km, or for a doubled time span for the model with a 2-km-thick Casqus

Chapter 5

layer more fault slip accumulation will be accommodated at depth and hence the growth of the surface expression above the blind thrust is not linearly proportional to fault slip.

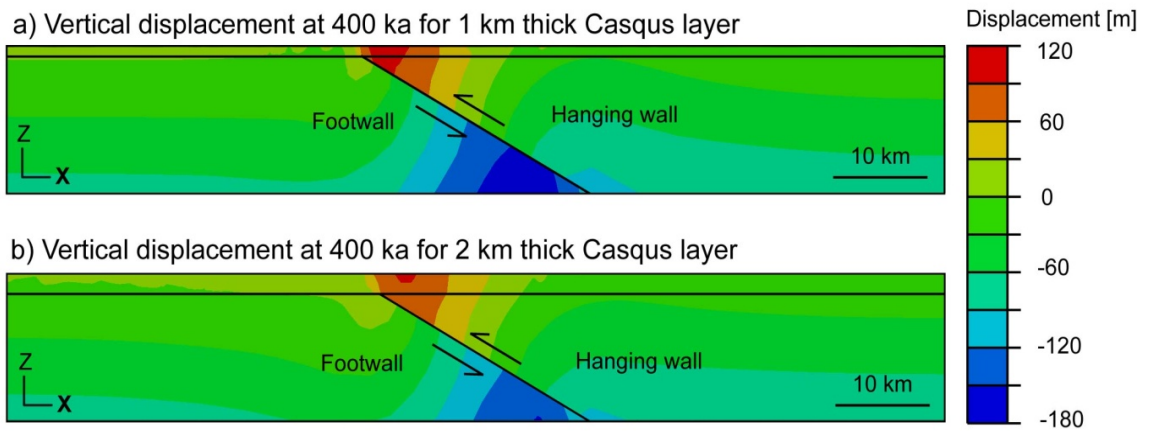


Figure 44: Vertical displacement in the middle of the model at 400 ka *a)* for 1-km-thick Casqus layer and *b)* for 2-km-thick Casqus layer. The diffusion constant k_D is $0.3 \text{ m}^2/\text{a}$ and the fluvial erosion constant $K_f \cdot p$ is set at 0.03 m/a in both model runs. The sense of movement is indicated by the arrows.

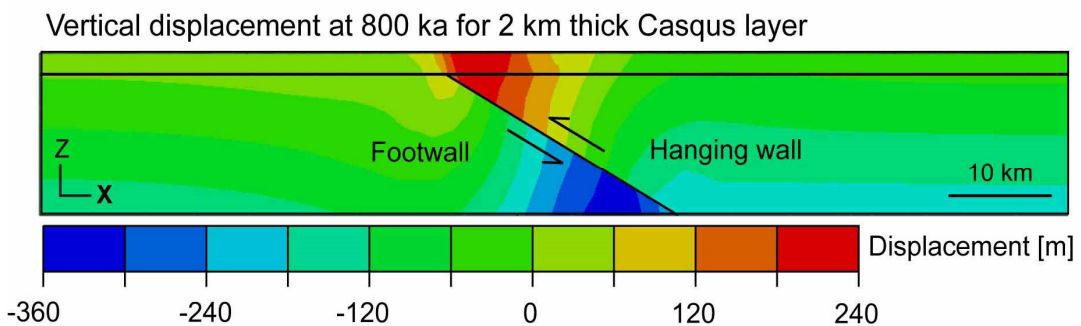


Figure 45: Vertical displacement in the middle of the model at 800 ka for 2-km-thick Casqus layer. The diffusion constant k_D is $0.3 \text{ m}^2/\text{a}$. The fluvial erosion constant $K_f \cdot p$ is set at 0.03 m/a . The sense of movement is indicated by the arrows.

5.4.1 Comparison with other studies

When the modelling results of the present study are compared with the findings from other numerical studies and field observations, a similar behaviour is obvious. For example, when erosion and sedimentation are not applied on the model surface, the resulting topography above the blind thrust corresponds to that of *Ellis and*

Chapter 5

Densmore (2006). In their study the fault top edge was initially set at 0.5 km below the model surface. For a 30°-dipping blind thrust the topography results in a steep and narrow forelimb whereas the backlimb has a shallower dipping hillslope and the subsidence is located mainly in the hanging wall. They also showed the effect of the depth of the fault top edge. With increasing depth the surface deformation becomes less pronounced and the fold becomes more symmetric. This leads to uplift of the foredeep on the basis of the forelimb and on the hanging wall. This is in accordance with the results of the present study (e.g. *Figure 37*). The cumulative fault slip accumulation of ~190 - 550 m obtained in this study is in accordance with the findings of *Davis et. al (2005)* that the maximum natural fault displacement in the middle of the thrust faults is up to around 2% of the fault length. This results in a maximum fault slip accumulation of 600 m for a fault of 30 km length.

Some studies about blind thrusts (e.g. *Albertz and Lingrey, 2012; Albertz and Sanz, 2012; Smart et al., 2012*), include a layered covering with varying material properties. In addition, in these studies the shortening of the model is limited to the hanging wall side only, i.e. the opposite side of the model is fixed. Although the model set up differ from the one used in the present study, the topography above blind thrust faults is similar to the 2-dimensional Abaqus-models by *Smart et al. (2012)*, when the profiles cutting the blind thrust in the middle of the models are considered (*Figure 45a*). This is also the case for the studies carried out by *Albertz and Lingrey (2012) (Figure 45b)* and *Albertz and Sanz (2012) (Figure 45b)*. Both studies are based on the finite element method as well.

To investigate the effect of potential blind thrust beneath the Sichuan Basin *de Michele et al. (2010)* used inverted Synthetic Aperture Radar data. The present study was executed with the Finite Element method by applying similar fault geometry such as a fault length of 30 km, fault dip of 30° and the depth of fault top edge at 1-2 km. Despite the different approaches the blind thrust faults investigated show similar behaviour. When the 30°-dipping blind thrust faults of each study are compared, the resulting profiles showing the characteristics of the vertical surface deformation adjacent to the blind thrust fault are in accordance (e.g. *Figure 35*). The forelimb is steep and the backlimb exhibits a shallower hillslope. Despite the fact that the blind thrust models of the present study include only a single fault, the surface deformation show similar overall behaviour. It is to note that the investigations of *de Michele et al. (2010)* concentrate on the single earthquake showing corresponding fault slip and surface evolution. The present study shows the results for time spans of up to 800 ka with subsequently higher amounts of fault displacement and surface folding. Also surface processes are applied on the model surface.

Chapter 5

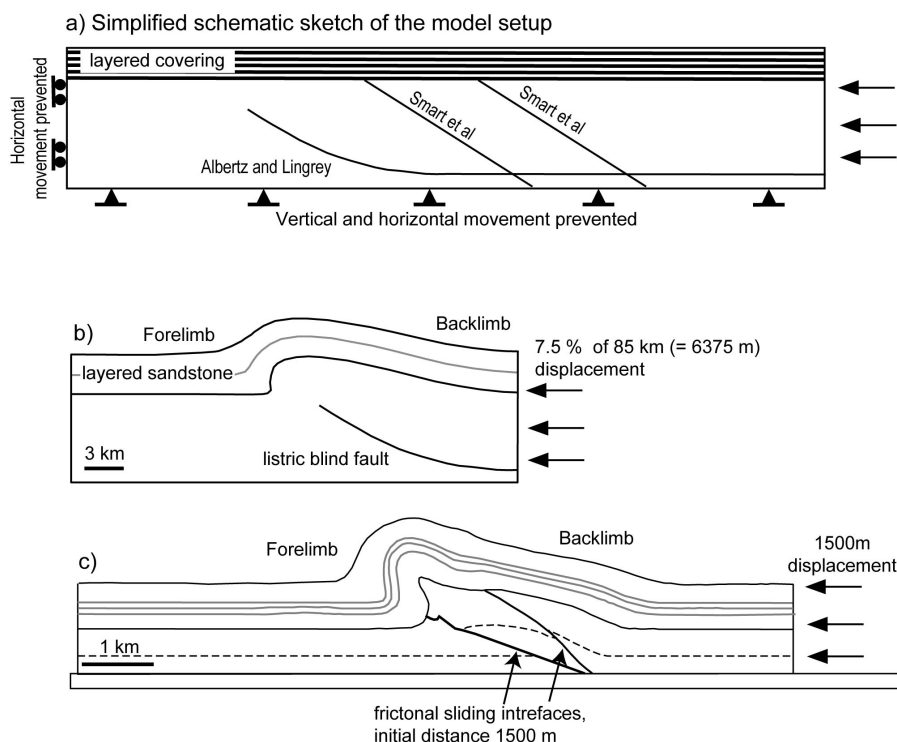


Figure 46: Examples of the model setup and resulting morphology from other studies. *a)* The simplified model sketch for the model setup which was similar in the experiments of *Albertz and Lingrey (2012)*, *Albertz and Sanz (2012)* and *Smart et al. (2012)*. Note that the sketch is only schematic and does not show the actual position of the faults. The sketch is not scaled, since the scale varies in different studies. In all models, the uppermost sediments are layered. The left side is fixed in horizontal direction and the shortening is limited to the right side. Both vertical and horizontal movement of the bottom of the model is prohibited. The faults are embedded either as parallel interfaces (*Smart et al., 2012*) or as a listric fault (*Albertz and Lingrey, 2012; Albertz and Sanz, 2012*). *b)* A part of the model after a certain amount of displacement for a model setup with a listric fault initially dipping with 30° . The uppermost ~ 3 km consist of 10 sandstone layers (*modified after Figure 41 in Albertz and Lingrey, 2012*). *c)* The results from *Smart et al. (2012)* after 1500 m displacement on the right side. The initial distance between the faults was 1500 m. The layers have different material properties and are separated by lines (*modified after Figure 6 in Smart et al., 2012*).

The blind thrust models presented in this study are applicable to the Los Angeles basin, where a fault dip of 30° was determined for several faults (e.g. *Davis and Namson, 1994; Hauksson et al., 1995; Dolan et al., 2003*). Neither the Whittier Narrows Earthquake in 1987 at around 13 km depth along the Puente Hills blind thrust (*Hauksson et al., 1988; Dolan et al., 2003*) nor the Northridge Earthquake in 1994 at depth of around 18 km triggered any surface rupture but induced near surface folding (e.g. *Davis and Namson, 1994; Shaw and Suppe, 1996*). The fault tip of the former reaches a depth of 3 km and the latter ends at a depth of around 7 km below the Earth's surface (*Davis and Namson, 1994; Hauksson et al., 1995*). Hence, this could corroborate the modelling results that with increasing depth of the fault top edge, i.e. increasing thickness of Casqus layer, the surface deformation diminishes.

Chapter 5

Fault-propagation folding

The surface deformation above the blind thrust in the experiments ran for this thesis is induced by fault-propagation folding. Such surface folds are described as asymmetrical fold pairs induced by propagating faults below the surface (*Hardy and Ford, 1997*). This kind of deformation occurs, when the fault tip is subject to compressive forces during upward propagation (*Suppe, 1983*) and the shortening rate exceeds the fault propagation rate (*Cooley et al., 2011*). The fault displacement beneath the fault-propagation fold decreases upwards along the ramp region (*Jamison, 1987*).

In nature, fault-propagation folding commonly occurs in fold-and-thrust belts as well as in forelands (e.g. *Suppe, 1983; Chester and Chester, 1990; Erslev and Mayborn, 1992; Bulnes and Aller, 2002; Wilson et al, 2009; Cooley et al., 2011; Calamita et al., 2012; Jabbour et al., 2012*). Some natural examples are known besides the Canadian thrust belt (e.g. *Erslev and Mayborn, 1992; Cooley et al., 2011; Jabbour et al. 2012*) also in the Colorado Plateau (e.g. *Kelley, 1955; Hilley et al., 2010*) and in the Apennines (e.g. *Wilson, 2009; Calamita et al., 2012*).

The Canadian thrust belt accommodates several regions with surface structures induced by fault propagation. Well exposed folds with fault traces exist in the Livingstone Range anticlinorium (*Cooley et al., 2011*), where the folds form an echelon array and are linked with each other. The relatively tight folding is chevron-like. The surface structures in the Livingstone Ridge are cut by very steep or almost vertical, so called tear faults that incise the folds perpendicular to fold strike (*Cooley et al., 2011*). One example of the exposed surface structures is shown in *Figure 47* illustrating the Centre Peak fold in southern Livingstone Ridge. The present Peak reaches an elevation of more than 2000 m. The Ernst Creek thrust beneath the fold extends 20 km northward from the Centre Peak (*Cooley et al., 2011*). The thrust faults are indicated by dashed white lines and the boundaries of different formations by black lines.

Other examples are provided by the Cline fold and the Elliot Peak fold (*Erslev and Mayborn, 1992*). The local relief of the folds analysed by *Erslev and Mayborn (1992)* exceeds 1000 m and allow distinct observation of the original deformation generated by fault-propagation folding. Also some faults are visible in the well exposed and preserved folds. The most spectacular exposure is observed at the Elliot Peak, where the 1100 m relief extends over an area of almost 2000 m. The Elliot Peak is described as a tight fold with a single axial plane (cf. *Erslev and Mayborn, 1992*).

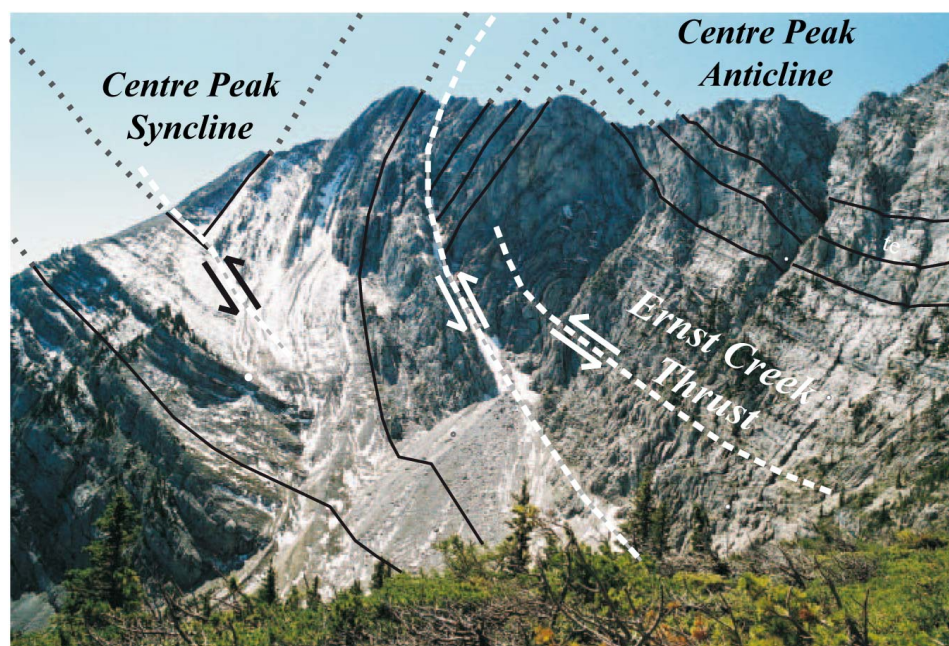


Figure 47: The >2000-m-high Centre Peak fold in the Livingstone Anticlinorium in Canada. Thrust faults are indicated by white dashed line. The black lines show the boundaries of different formations enclosed by the fold. The black lines with dots reflect the original folding (*modified after Cooley et al , 2011*).

In the Colorado Plateau in the western USA, the length of the surface folds vary between 24 - 240 km, the height is 60 - 2000 m and the dip is 15 - 80° for different monoclines (*Kelley, 1955*). The Comb Ridge, for example, is nearly 150 km long, up to ~910 m high and the maximum dip is 45° (*Kelley, 1955*). This structure coincides with the slip accumulation of a blind fault striking parallel to the elongation of the monocline (*Hilley et al., 2010*). The ~500-m-high Raplee Ridge fold west from the Comb Ridge monocline is around 14 km long and 2 km wide (*O'sullivan, 1965; Ziony, 1966*). The forelimb dips at <40°, whereas the dip on the backlimb is up to 5° (*Hilley et al., 2010*). Hence the shape with a steeper forelimb and gently dipping backlimb resembles the surface folds in the present study. The fault that generated the surface fold is unexposed (*Hilley et al., 2010*). *Figure 48* shows an aerial photograph of the monocline (*from Hilley et al., 2010*).

5.5 Conclusions

The investigations on a blind thrust indicate that surface processes do not affect fault slip evolution. Hence the mass redistribution only deforms the model surface. However, the depth of the fault top edge has an impact on the fault slip evolution. The fault slip accumulation is higher for the thinner Casqus layer. Also the shape and

Chapter 5

the height of the growing anticline depend on the thickness of the Casqus layer. In general, folding on the surface of the thinner Casqus layer is characterised by steeper morphology for model runs with and without surface processes. On the model surface of the thicker Casqus layer both the forelimb and the backlimb are less steep. When surface processes are active, the hinterland basin on the thicker Casqus layer is shifted towards the model boundaries further away from the backlimb. The average local amount of sedimentation and erosion after 400 ka on the forelimb derived along the profiles indicates that the erosion remains the same irrespective of the thickness of the layer Casqus layer the blind thrust fault. The erosion on the backlimb and the sedimentation in the hinterland basin is slightly more for the thicker covering. When the run time is doubled to 800 ka the hinterland basin on the thicker Casqus layer is flattened due to sediment filling for all diffusion constants k_D . The corresponding erosion is up to 10 times higher and the sedimentation around 6 times more than at 400 ka for the thicker covering. Since more of the fault slip is accommodated at higher depths for the thinner Casqus layer the vertical extent of the surface fold is not linearly proportional to fault slip, when the corresponding values for model runs with different thicknesses of the Casqus layer are compared.



Figure 48: Aerial photograph showing the 500-m-high Raplee Ridge monocline in southeast Utah. View from south (*modified after Hilley et al , 2010*).

6. Discussion

The experiments for this thesis were run by using the fully coupled modelling technique, where the software CASQUS (Kurfeß, 2008; Kurfeß and Heidbach, 2009) couples the landscape evolution tool CASCADE (Braun and Sambridge, 1997) with three-dimensional geomechanical finite element models (Abaqus FEA). This method enables the simulation of the feedback between fault activity and mass redistribution due to erosion and sedimentation. The total model run time is in the order of 10^5 - 10^6 years and vary in different experiments.

According to the model results, in an extensional tectonic regime with normal faults cutting the model surface the fault slip accumulation is affected by surface processes. This is shown by the comparison of cumulative fault slip both in model runs with and without surface processes. In different settings used in the experiments, i.e., single normal faults or fault arrays, the total fault displacement is increased by up to 200 m when erosion and sedimentation are applied on the model surface. The slip rates vary from ~ 0.6 mm/a to ~ 1.7 mm/a. The resulting amount of additional fault slip due to surface processes is controlled by the diffusion constant as well as fault dip and length. The fluvial erosion constant has a less pronounced effect on fault slip evolution when compared with other parameters varied throughout the experiments.

The results from experiments on an extensional tectonic regime with normal faults show that the topography developing on the uplifted footwall is subject to erosion whereas the subsiding hanging wall basin is gradually filled with sediments. Similar to fault slip evolution, also the cumulative amount of erosion and sedimentation depends on the run time and on the parameters used. In different extensional settings used in this study, the erosion rates on the footwall and the sedimentation rates on the hanging wall both vary from ~ 30 m/Ma to ~ 80 m/Ma. The erosion rates are in accordance with the rates of ~ 10 - 35 m/Ma determined for the Sweetwater footwall in the Basin-and-Range province (Densmore et al., 2009)(Figure 49).

In general, the effect of mass redistribution on the landscape evolution is obvious when the model surface is compared with the topography of a model run without surface processes. Due to surface processes, a river network evolves on the model surface adjacent to fault scarp throughout the model run. The number and depth of streams that transport sediments vary for different parameters controlling surface processes. For higher diffusion constant or lower fluvial erosion constant the topography becomes smoother and the number of rivers decreases when compared with model runs with a lower diffusion constant or higher fluvial erosion constant that generate a steeper landscape and a denser channel network.

Chapter 6

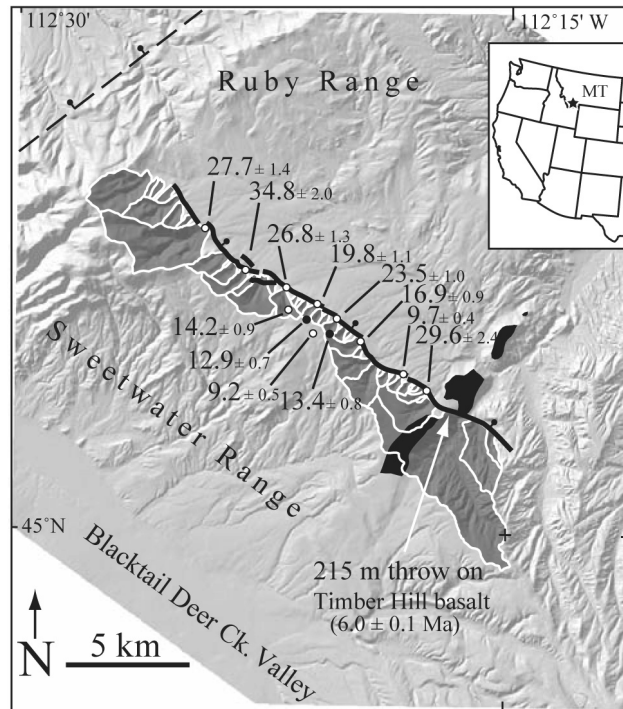


Figure 49: Catchment-wide averaged denudation rates (mm/ka) for the 18-km-long Sweetwater footwall in south-western Montana, USA. The rates were determined with cosmogenic radionuclide analysis (CRN). Figure modified after *Densmore et al. (2009)*.

The experiments on single normal faults show that the fault length and dip as well as the diffusion constant have a pronounced effect on the fault slip evolution and on the subsequent landscape evolution. The results from the experiments with single normal faults show that the fault slip increases for longer (40 km) and shallower dipping (45°) faults, whereas the cumulative amount of fault slip decreases for shorter (10 km) and steeper (75°) faults. The fault slip evolution is also affected by the diffusion constant and is slightly higher for higher diffusion constant ($k_D = 0.5\text{ m}^2/a$) and the fault accumulates less displacement for lower diffusion constant ($k_D = 0.1\text{ m}^2/a$). As described above, the impact of fluvial erosion constant on the fault slip evolution of single normal faults is relatively low but the topography on the model surface in different experiments is strongly affected when the fluvial erosion increases ($K \cdot p = 0.05\text{ m/a}$) or decreases ($K \cdot p = 0.01\text{ m/a}$).

The experiment on a horst structure with 6 faults show that in the model runs without surface processes, the central faults obtain up to $\sim 44\text{ m}$ more fault slip than the distal faults. In presence of surface processes due to erosion and sedimentation, the difference between central and distal faults is as high as 70 m , depending on the parameters controlling the intensity of surface processes. Such behaviour of faults in an array is also shown for example by *Willemse et al (1996)* and *Cowie and Roberts (2001)*. The modelling results from experiments with fault arrays corroborate, in

Chapter 6

general, the overall pattern of fault slip and landscape evolution shown in experiments on single normal faults. In the presence of erosion and sedimentation, the fault slip accumulation is up to ~160 m higher than in the model runs without surface processes, whereas the highest fault displacement is obtained by the 30-km-long faults in the array with 4 faults. For both model setups, the elevated horst structure is cut and modified by rivers, which erode material from the footwall. In addition, when surface processes are applied on the model surface, the loading of some hanging wall basins is asymmetric due to sediment flow via rivers. The direction of the rivers is controlled by relay ramps that develop between the faults. Experiments with a predefined canyon between two faults show that the additional sediment supply indeed affects the fault slip evolution by increasing it in the order of tenth of meters.

Considering the fault arrays, the supplementary material filling the hanging wall basins leads to shifting of the highest fault displacement along the fault plane. In the experiments ran for this thesis, the shifting is up to hundreds of meters towards the water mouth. The migration of the highest fault slip along fault strike towards the fault tip in a fault array was also observed by *Willemse et al. (1996)* and *Willemse (1997)*. They argue that especially overlapping faults contribute to the fault slip evolution of the adjacent fault and hence the maximum fault displacement is shifted away from the centre of the fault. According to *Willemse et al. (1996)* and *Willemse (1997)*, similar but not that pronounced behaviour is observed also for underlapping normal faults, which is the case in the fault arrays used in the present study. They also argue, that the migration of the maximum displacement is more pronounced for longer faults in arrays, whereas isolated normal faults experience symmetric fault displacement along fault strike.

To further investigate the effect of surface processes alone on the fault slip accumulation, the far-field extension was stopped but surface processes remained active. The point in time where cessation of extension takes place was chosen so that the morphology at cessation of regional extension is similar for all model runs with different parameters. Hence the point in time was determined by using the fault scaling law $D = 0.03L^{1.06}$, where D is the displacement at the fault centre in metres and L the fault length in metres (*Schlische et al., 1996*). The experiments show that although the far-field boundary conditions change, i.e. the extension of the model stops, surface processes may lead to prolonged fault slip accumulation for additional 10^5 - 10^6 years. For a low diffusion constant ($0.1 \text{ m}^2/\text{a}$), a shallow fault dip (45°) and a long fault (40 km) an almost constant rate of fault displacement for several million years is obtained. In the case of single normal faults, the former two lead to a prolonged fault slip for 6-7 Ma after cessation of extension. For opposed parameters, the fault slip ceases or is reversed after 0.5 - 1.5 Ma of normal sense of fault slip. In summary, the slip rates of 19 -89 m/Ma determined for single normal faults after the

Chapter 6

end of far-field extension indicate that in regions, where the regional extension has ceased, normal faulting may remain active and hence earthquake occurrence may continue.

A correlation between fault slip evolution, mass redistribution and the evolution of differential stress was observed throughout the experiments on faults in an extensional tectonic regime. This is obvious from experiments where the far-field extension ceases. The subsequent fault slip evolution reflects changes in rates of mass redistribution, which in turn correlate with the evolution of the differential stress.

The experiments on blind thrust faults show that surface processes do not significantly affect the fault slip evolution. However, the thickness of the Casqus layer has an impact on the fault slip evolution and the resulting surface deformation. Folding on the model surface is generated by the propagation of the fault due to slip accumulation along the fault plane, indicating that the deformation rate is faster than the fault slip rate (*Cooley et al., 2011*). If this is not the case, natural examples observed for instance in the Po plain, Italy, show that despite of blind thrusts, the surface deformation above them is negligible (*Burrato et al., 2003*). Although the fault slip evolution is not affected by surface processes, the growth fold and adjacent regions on the model surface are subject to erosion and sedimentation. In the present study, the forelimb of the surface fold dips steeper than the backlimb and the width of the hinterland basin is controlled by surface processes as well as by the thickness of the Casqus layer covering the blind thrust fault. On the thinner Casqus layer, the surface fold is more than 45 m higher than for the thicker Casqus layer after 800 ka of model time. When surface processes are active, the fold becomes narrower along-strike. Erosion modifies especially the backlimb and the hinterland basin may be thoroughly filled with sediments. It is to note, that in the present study a depth of 1 and 2 km were used in the experiments with blind thrusts and the results hence apply for the specific model setup.

The 500-m-high, 14-km-long and 2-km-wide Raplee Ridge monocline with the thrust fault beneath it in the Colorado Plateau were modelled by *Hilley et al (2010)*. For their inversion modelling technique, a three-dimensional Boundary Element modelling (BEM) was used, where the brittle upper crust is defined as homogeneous and elastic. This is also the case in the models constructed with the Finite Element method in the present study. *Figure 50a* shows the model setup used by *Hilley et al. (2010)* to model the fault geometry beneath the Raplee Ridge monocline. The fault is embedded as elliptically shaped and frictionless planar fault. The deformed surface is shown in *Figure 50b*. The best-fitting results from the inversion study indicate that the fault beneath the monocline most likely has a down-dip extent of up to ~14 km and an along-strike width of up to ~30 km. According to the results the

Chapter 6

fault top edge was at a depth of 2 - 9.5 km during deformation (Hilley *et al.*, 2010). In the experiments on blind thrusts for this thesis an along-strike fault length of 30 km and a depth of the fault top edge of 1-2 km were used. The resulting surface deformation is similar to that seen on the Raplee Ridge (see Figure 48 in Chapter 5).

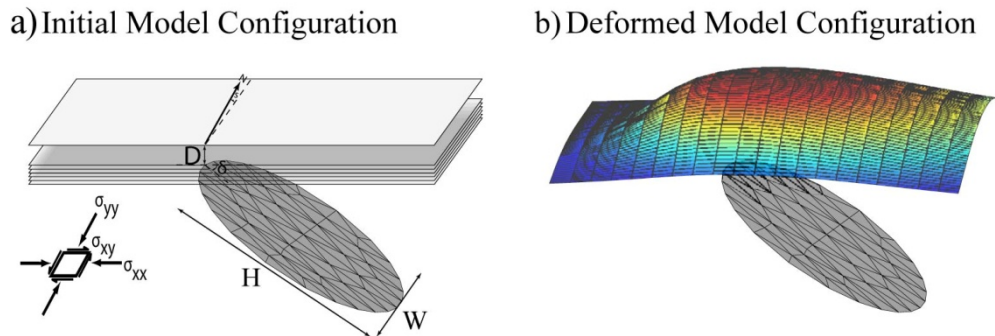


Figure 50: a) Initial setup of the Boundary Element model by Hilley *et al.*, (2010) for the inverse modelling of the Raplee Ridge monocline and thrust fault. b) Deformed model surface. H = down-dip length of the fault, W = along-strike width of the fault and D = depth of the fault below the surface (modified after Hilley *et al.*, 2010).

Although the models used in this thesis provide an insight into the interaction of surface processes and fault activity, to construct numerical models that are adjusted to specific natural landscapes on larger scales for example in continental rift systems (e.g. the Gulf of Corinth and the Basin-and-Range province) or in regions of crustal shortening (e.g. the Himalayas), spatially and temporally larger models are necessary. This requires for instance additional rheological properties such as the viscoelastic lower crust. Also a denser element mesh is required to resolve smaller-scale variations of deformation and landscape. In addition, by applying a geothermal gradient in the numerical models, the results could be compared with thermochronology data obtained by field observations.

7. Conclusions

The findings from the experiments with the fully coupled modelling technique used in this study indicate a feedback between surface processes and tectonics. According to the results, the mass redistribution due to erosion and sedimentation affects the fault slip evolution in extensional settings with a fault that initially ruptures on the model surface. The fault slip accumulation increases by up to ~200 m when surface processes are applied on the model surface, whereas the amount of additional fault displacement depends on different parameters. So, increasing diffusion constant simulating the diffusive hillslope processes (effect of e.g. rain splash and soil creep), fault dip and length lead to increased displacement accumulated by the fault. In contrast, the fluvial erosion constant (product of precipitation rate and the ability of rivers to transport material) has a less pronounced impact on the fault slip accumulation but the landscape is strongly affected for different intensity of the fluvial erosion. Hence, an increasing fluvial erosion constant leads to more rough model surface due to increasing number of deeper rivers, if the diffusion constant remains the same.

In an en echelon fault array, the fault slip accumulated by the central faults is significantly higher than for the distal faults. The experiments on fault arrays simulating settings where the far-field extension has ceased but surface processes remain active indicate that a normal fault may continue to accumulate fault slip due to mass redistribution on the Earth's surface. If a predetermined river transports sediments into a specific hanging wall basin, this leads to a more asymmetric loading in the hanging wall when compared with model runs without predefined initial channel. As a consequence, the highest fault displacement is shifted from the middle of the fault towards the stream mouth. Again, the amount of additional sediments accumulated via the initial canyon depends on the parameters controlling the surface processes.

The correlation of erosion and sedimentation with fault slip evolution was observed throughout the extensional experiments, where the fault scarp develops on the model surface. This is most obvious from experiments where the sediment flow was manipulated by constraining an initial canyon redirecting sediments into a specific hanging wall throughout the model run (fault arrays) or where the far-field extension ceased and surface processes remained active (single normal fault and fault arrays). Besides the findings that the rate of fault slip accumulations reflects changes in mass redistribution on the surface, also a correlation between fault slip evolution and changes in differential stress due to erosion and sedimentation was observed.

In the experiments where the regional extension ceases but surface processes remain active, the fault experiences normal sense of faulting for ~30 ka - 3 Ma and the additional normal fault slip vary from less than 1 m to ~90 m, respectively. An

Chapter 7

additional model run reveals, that the normal fault slip may continue for more than 7 Ma after cessation of far-field extension and the additional fault slip is ~160 m. Cessation of regional extension in the model leads to a transition to lower rates of mass redistribution on the surface and the duration of the transition to lower erosion and sedimentation rates coincides with the fault slip evolution. Slow transition reflects a prolonged normal faulting after cessation of extension, whereas a rapid change in erosion and sedimentation rates leads to a short period of normal sense of slip and subsequent transition to reverse slip. The former is the case for example for relatively low diffusion constant and shorter faults as well as for higher fault dip. Opposed parameter trends reflect inverse behaviour.

In contrast to an extensional tectonic regime, the experiments on blind thrusts show that surface processes may not have an impact on the fault slip evolution irrespectively of the depth of the fault top edge used in the experiments. The topography above the blind thrust as well as the fault displacement at depth is strongly affected by the depth of the fault. The surface fold is higher and steeper and the fault slip accumulation is higher for a blind thrust beneath a thinner covering layer. The anticline above the blind thrust on the thicker covering layer, however, experiences in general more pronounced erosion and sedimentation than on the thinner covering above the blind thrust.

Acknowledgements

The funding for this work was provided by the German Research Foundation (DFG) within the fellowship to Dr. Georgios Maniatis. I would like to thank Prof. Andrea Hampel, Prof. Ulrich Heimhofer and Prof. Jürgen Koepke for their support and reviewing this thesis as well as Prof. Francois Holtz for his support as a chairman of the examination committee. In particular I would like to thank Dr. Georgios Maniatis for many constructive discussions and ideas as well as for providing technical support with Abaqus and Casqus. I would also like to thank my colleague Tao Li for helpful discussions considering numerical modelling with Abaqus.

References

- Abaqus User's Manual, Versions 6.9.3, 6.11.1 and 6.12.1, 2009-2012. Dassault Systèmes Simulia, Providence, Rhode Island, USA. www.simulia.com.
- Albertz, M., Lingrey, S., 2012. Critical state finite element models of contractional fault-related folding: Part 1. Structural analysis. *Tectonophysics*, 576-577, 133-149. doi: 10.1016/j.tecto.2012.05.015.
- Albertz, M., Sanz, P.F., 2012. Critical state finite element models of contractional fault-related folding: Part 2. Mechanical analysis. *Tectonophysics*, 576-577, 150-170, doi:10.1016/j.tecto.2012.06.016.
- Anders, M.H., Spiegelman, M., Rodgers, D.W., Hagstrum J.T., 1993. The growth of fault bounded tilt blocks. *Tectonics* 12, 1451-1459.
- Anderson, O.L., 1952. Conditions for the Derivation of the Stress Deviator Tensor. *American Journal of Physics*, 20, 236. <http://dx.doi.org/10.1119/1.1933178>.
- Argus, D.F., Heflin, M.B., Donnellan, A., Webb, F.H., Dong, D., Hurst, K.J., Jefferson, D.C., Lyzenga, G.A., Watkins, M.M., Zumberge, J.F., 1999. Shortening and thickening of metropolitan Los Angeles measured and inferred by using geodesy. *Geology*, 27 (8), 703-706.
- Arpat, E., Şaroğlu, F., 1972. The East Anatolian fault system: Thoughts on its development. *Bulletin of Mineral Research and Exploration Institute of Turkey*, 78, 33-39.
- Avallone, A. Briole, P., Agatza-Balodimou, A.M., Billiris, H., Charade, O., Mitsakaki, C., Necessian, A., Papazissi, K., Paradissis, D., Veis, G., 2004. Analysis of eleven years of deformation measured by GPS in the Corinth Rift Laboratory area. *Comptes Rendus Geoscience* 336, 301-311.
- Avouac, J. P., Tapponnier, P., Bai, M., You, H., Wang, G., 1993. Active thrusting and folding along the northern Tien Shan and late Cenozoic rotation of the Tarim relative to Dzungaria and Kazakhstan. *Journal of Geophysical Research: Solid Earth* (1978-2012), 98(B4), 6755-6804.
- Avouac, J.-P., Burov, E.B., 1996. Erosion as driving mechanism of intracontinental mountain growth. *Journal of Geophysical Research*, 101, 17747-17769.
- Berberian, M., 1995. Master "blind" thrust faults hidden under the Zagros folds: active basement tectonics and surface morphotectonics. *Tectonophysics*, 241(3), 193-224. [http://dx.doi.org/10.1016/0040-1951\(94\)00185-C](http://dx.doi.org/10.1016/0040-1951(94)00185-C).
- Bishop, P., 2007. Long-term landscape evolution: linking tectonics and surface processes. *Earth Surface Processes and Landforms*, 32, 3, 329-365.
- Bonini, L., Di Bucci, D., Toscani, G., Seno, S., Valensise, G., 2013. A reversed hierarchy of active normal faults: the 6 April 2009, *Mw* 6.3, L'Aquila earthquake (Italy). *Solid Earth Discussions*, 5, 117-134, doi:10.5194/sed-5-117-2013.
- Bonnet, S., Crave, A., 2003. Landscape response to climate change: Insights from experimental modeling and implications for tectonic versus climatic uplift of topography. *Geology*, 31(2), 123-126, doi: 10.1130/0091-7613(2003)031<0123:LRTCCI>2.0.CO;2.
- Bosworth, W., Strecker, M.R., 1997. Stress field changes in the Afro-Arabian rift

References

- system during the Miocene to Recent period. *Tectonophysics* 278, 47-62.
- Bosworth, W.M, Strecker, M.R., Blisniuk, P.M., 1992. Integration of East-African paleostress and present-day stress data - implications for continental stress-field dynamics. *Journal of Geophysical Research* 97, B8, 11851-11865.
- Braun, J., Sambridge, M., 1997. Modelling landscape evolution on geological time scales: a new method based on irregular spatial discretization. *Basin Research* 9, 27-52. (for the CASCADE-code, contact Jean.Braun@univ-rennes1.fr)
- Braun, J., Thieulot, C., Fullsack, P., DeKool, M., Beaumont, C., Huismans, R., 2008. DOUAR: a new three-dimensional creeping flow numerical model for the solution of geological problems. *Physics of the Earth and Planetary Interiors*, 171, 76–91.
- Briole, P., Rigo, A., Lyon-Caen, H., Ruegg, J.-C., Papazissi, K., Mitsakaki, C., Balodimou, A., Veis, G., Hatzfeld, D., Deschamps, A., 2000. Active deformation of the Corinth Rift, Greece: results from repeated Global Positioning System surveys between 1990 and 1995. *Journal of Geophysical Research* 105, 25605-25625.
- Burov, E., Toussaint, G., 2007. Surface processes and tectonics: forcing of continental subduction and deep processes. *Global and Planetary Change*, 58(1), 141-164.
- Brooks, M., Ferentinos, G., 1984. Tectonics and sedimentation in the gulf of Corinth and the Zakynos and Kefallinia channels, western Greece. *Tectonophysics* 101, 25–54.
- Bulnes, M., Aller, J., 2002. Three-dimensional geometry of large-scale fault-propagation folds in the Cantabrian Zone, NW Iberian Peninsula. *Journal of structural geology*, 24 (4), 827-846.
- Burbank, D.W., Anderson, R.S., 2012. *Tectonic geomorphology*. Wiley-Blackwell.
- Burbank, D.W., Pinter, N., 1999. Landscape evolution: the interactions of tectonics and surface processes. *Basin Research*, 11,1, 1-6.
- Burbank, D., Meigs, A., Brozović, N., 1996. Interactions of growing folds and coeval depositional systems. *Basin Research*, 8: 199–223. doi: 10.1046/j.13652117.1996.00181.x
- Burrato, P., Ciucci, F., Valensise, G., 2003. An inventory of river anomalies in the Po Plain, Northern Italy: evidence for active blind thrust faulting. *Annals of Geophysics*, 46 (5), 865–882.
- Burrato, P., Vannoli, P., Fracassi, U., Basili, R., Valensise, G., 2012. Is blind faulting truly invisible? Tectonic-controlled drainage evolution in the epicentral area of the May 2012, Emilia-Romagna earthquake sequence (northern Italy). *Annals of Geophysics*, 55 (4), 525-531, doi:10.4401/ag-6182.
- Calamita, F., Pace, P., Satolli, S., 2012. Coexistence of fault-propagation and fault-bend folding in curve-shaped foreland fold-and-thrust belts: examples from the Northern Apennines (Italy). *Terra Nova*, 24 (5), 396-406.

References

- Cavinato, G.P., De Celles, P.G., 1999. Extensional basins in the tectonically bimodal central Apennines fold-thrust belt, Italy: response to corner flow above a subducting slab in retrograde motion. *Geology* 27,955–958.
- Chester, J.S., Chester, F.M., 1990. Fault-propagation folds above thrusts with constant dip. *Journal of Structural Geology*, 12 (7), 903-910.
- Chiarabba, C., Amato, A., Anselmi, M., Baccheschi, P., Bianchi, I., Cattaneo, M., Cecere, G., Chiaraluce, L., Ciaccio, M.G., De Gori, P., De Luca, G., Di Bona, M., Di Stefano, R., Faenza, L., Govoni, A., Improta, L., Lucente, F.P., Marchetti, A., Margheriti, L., Mele, F., Michelini, A., Monachesi, G., Moretti, M., Pastori, M., PianaAgostinetti, N., Piccinini, D., Roselli, P., Seccia, D. and Valoroso, L., 2009. The 2009 L'Aquila (central Italy) Mw 6.3 earthquake: mainshock and aftershocks. *Geophysical Research Letters*, 36, L18308.
- Cloetingh, S., McQueen, H., Lambeck, K., 1985. On a tectonic mechanism for regional sealevel variations. *Earth and Planetary Science Letters*, 75, 157–164.
- Cooley, M.A., Price, R.A., Dixon, J.M., Kyser, T.K., 2011. Along-strike variations and internal details of chevron-style, flexural-slip thrust-propagation folds within the southern Livingstone Range anticlinorium, a paleohydrocarbon reservoir in southern Alberta Foothills, Canada. *AAPG bulletin*, 95 (11), 1821-1849.
- Cowie, P.A., Roberts, G.P., 2001. Constraining slip rates and spacings for active normal faults. *Journal of Structural Geology* 23, 1901-1915.
- Cowie, P.A., Scholz, C.H., 1992a. Growth of faults by accumulation of seismic slip. *Journal of Geophysical Research* 97, 11085-11095.
- Cowie, P.A., Scholz, C.H., 1992b. Physical explanation for the displacement-length relation-ship of faults using a post-yield fracture mechanics model. *Journal of Structural Geology* 14, 1133-1148.
- Cowie, P.A., Scholz, C.H., 1992c. Displacement-length scaling relationship for faults: data synthesis and discussion. *Journal of Structural Geology* 14, 1149-1156.
- D'Agostino N., Mantenuto S., D'Anastasio E., Giuliani R., Mattone M., Calcaterra S., Gambino P., Bonci L., 2011. Evidence for localized active extension in the central Apennines (Italy) from global positioning system observations, *Geology*, 39, 291–294 first published on March 8, 2011, doi:10.1130/G31796.1.
- D'Agostino, N., Avallone, A., Cheloni, D., D'Anastasio, E., Mantenuto, S., Selvaggi, G., 2008. Active tectonics of the Adriatic region from GPS and earth-quake slip vectors, *Journal of Geophysical Research*, 113, B12413, doi:10.1029/2008JB005860.
- Davis, K., Burbank, D.W., Fisher, D., Wallace, S., Nobes, D., 2005. Thrust-fault growth and segment linkage in the active Ostler fault zone, New Zealand. *Journal of Structural Geology*, 27, 1528–1546. doi:10.1016/j.jsg.2005.04.011.
- Davis, T.L., Namson, J.S., 1994. A balanced cross section analysis of the 1994 Northridge earthquake and thrust fault seismic hazards in southern California. *Nature*, 372, 167–169.

References

- Dawers, N.H., Anders, M.H., Scholz, C.H., 1993. Growth of normal faults: displacement-length scaling. *Geology* 21, 1107-1110.
- de Michele, M., Raucoules, D., de Sigoyer, J., Pubellier, M., Chamot-Rooke, N., 2010. Three-dimensional surface displacement of the 2008 May 12 Sichuan earthquake (China) derived from Synthetic Aperture Radar: evidence for rupture on a blind thrust. *Geophysical Journal International*, 183, 1097–1103, doi: 10.1111/j.1365-246X.2010.04807.x
- DeCelles, P.G., Robinson, D.M., Zandt, G., 2002. Implications of shortening in the Himalayan fold-thrust belt for uplift of the Tibetan Plateau. *Tectonics*, 21(6), 1062. doi:10.1029/2001TC001322.
- Densmore, A.L., Dawers, N.H., Gupta, S., Guidon, R., Goldin, T., 2004. Footwall topographic development during continental extension. *Journal of Geophysical Research* 109, F03001, doi: 10.1029/2003JF000115.
- Densmore, A.L., Ellis, M.A., Anderson, R.S., 1998. Landsliding and the evolution of normal fault-bounded mountains. *Journal of Geophysical Research* 103, 15203-15219.
- Densmore, A.L., Hetzel, R., Ivy-Ochs, S., Krugh, W.C., Dawers, N., Kubik, P., 2009. Spatial variations in catchment-averaged denudation rates from normal fault footwalls. *Geology* 37, 1139-1142, doi:10.1130/G30164A.1.
- Doğan, B., Karakaş, A., 2013. Geometry of co-seismic surface ruptures and tectonic meaning of the 23 October 2011 Mw 7.1 Van earthquake (East Anatolian Region, Turkey). *Journal of Structural Geology*, 46, 99-114, doi:10.1016/j.jsg.2012.10.00.
- Dolan, J.F., Christofferson, S.A., Shaw, J.H., 2003. Recognition of paleo-earthquakes on the Puente Hills blind thrust fault, California. *Science*, 300 (5616), 115-118. doi: 10.1126/science.1080593.
- Dunne, W.M., Ferrill, D.A., 1988. Blind thrust systems. *Geology*, 16 (1), 33-36. 10.1130/0091-7613(1988)016<0033:BTS>2.3.CO;2.
- Eaton, G.P., 1982. The Basin and Range province: Origin and Tectonic Significance. *Annual Review of Earth and Planetary Sciences* 10, 409-440.
- Ellis, M.A., Densmore, A.L., 2006. First-order topography over blind thrusts. In *Tectonics, Climate, and Landscape Evolution*, edited by S. D. Willett et al., Special Paper Geological Society of America, 398, 251–266, doi:10.1130/2006.2398 (15).
- Ellis, M.A., Densmore, A.L., Anderson, R.S., 1999. Development of mountainous topography in the Basin Ranges, USA, *Basin Research* 11, 21-41.
- Erslev, E.A., Mayborn, K.R., 1997. Multiple geometries and modes of fault-propagation folding in the Canadian thrust belt. *Journal of Structural Geology*, 19 (3), 321-335.
- Fischer, K.D., 2006. The influence of different rheological parameters on the surface deformation and stress field of the Aegean–Anatolian region. *International Journal of Earth Sciences*, 95 (2), 239-249.
- Fischer, K.D., Jahr, T., Jentzsch, G., 2004. Evolution of the Variscan foreland-basin: modelling the interactions between tectonics and surface processes. *Physics and*

References

- Chemistry of the Earth, 29, 665–671.
- Floyd, M.A., Billiris, H., Paradissis, D., Veis, G., Avallone, A., Briole, P., McClusky, S., Nocquet, J.-M., Palamartchouk, K., Parsons, B., England, P.C., 2010. A new velocity field for Greece: Implications for the kinematics and dynamics of the Aegean. *Journal of Geophysical Research* 115, B10403, doi:10.1029/2009JB007040.
- Ford, M., Rohais, S., Williams, E.A., Bourlange, S., Jousset, D., Backert, N. and Malartre, F., 2013. Tectono-sedimentary evolution of the western Corinth rift (Central Greece). *Basin Research*, 25: 3–25. doi: 10.1111/j.13652117.2012.00550.x
- Fuis, G.S., Ryberg, T., Godfrey, N.J., Okaya, D. A., Murphy, J.M., 2001. Crustal structure and tectonics from the Los Angeles basin to the Mojave Desert, southern California. *Geology*, 29(1), 15-18. doi: 10.1130/0091-7613(2001)029<0015:CSATFT>2.0.CO;2
- Gabrielsen, R.H., Kyrkjebø, R., Faleide, J.I., Fjeldskaar, W., Kjennerud, T., 2001. The Cretaceous post-rift basin configuration of the northern North Sea. *Petroleum Geoscience* 7, 137-154.
- Garcia-Castellanos, D., 2002. Interplay between lithospheric flexure and river transport in foreland basins. *Basin Research*, 14: 89–104. doi: 10.1046/j.1365-2117.2002.00174.x
- Gautier, P., Brun, J.P., 1994. Ductile crust exhumation and extensional detachments in the central Aegean (Cyclades and Evvia islands). *Geodinamica Acta* 7, 57–85. *Geology* 34 (4), 225–228, doi:10.1130/G21963.1.
- Godard, V., Burbank, D.W., 2011. Mechanical analysis of controls on strain partitioning in the Himalayas of central Nepal. *Journal of Geophysical Research: Solid Earth* (1978–2012), 116 (B10).
- Guglielmino, F., Anzidei, M., Briole, P., Elias, P., Puglisi, G., 2013. 3D displacement maps of the 2009 L’Aquila earthquake (Italy) by applying the SISTEM method to GPS and DInSAR data. *Terra Nova*, 25: 79–85. doi: 10.1111/ter.12008
- Hampel, A., Hetzel, R., Maniatis, G., Karow, T., 2009. Three-dimensional numerical modeling of slip rate variations on normal and thrust fault arrays during ice cap growth and melting. *Journal of Geophysical Research* 114, B08406, doi:10.1029/2008JB006113.
- Harbor, D.J., 1997. Landscape evolution at the margin of the Basin and Range. *Geology* 25, 1111-1114.
- Hardy, S., Finch, E., 2006. Discrete element modeling of the influence of the cover strength on basement-involved fault propagation folding. *Tectonophysics*, 415, 225–238, doi: 10.1016/j.tecto.2006.01.002.
- Hardy, S., Ford, M., 1997. Numerical modeling of trishear fault propagation folding. *Tectonics*, 16(5), 841-854.

References

- Hauksson, E., Jones, L.M., Hutton, K., 1995. The 1994 Northridge earthquake sequence in California: Seismological and tectonic aspects. *Journal of Geophysical Research*, 100(B7), 12335–12355, doi:10.1029/95JB00865.
- Hendrie, D.B., Kusznir, N.J., Morley, C.K., Ebinger, C.J., 1994. Cenozoic extension in northern Kenya: a quantitative model of rift basin development in the Turkana area. *Tectonophysics* 236, 409-438.
- Hetzel, R., Tao, M., Stokes, S., Niedermann, S., Ivy-Ochs, S., Gao, B., Strecker, M.R., Kubik, P.W., 2004. Late Pleistocene/Holocene slip rate of the Zhangye thrust (Qilian Shan, China) and implications for the active growth of the northeastern Tibetan Plateau. *Tectonics* 23, TC6006, doi:10.1029/2004TC001653.
- Hilley, G.E., Mynatt, I., Pollard, D.D., 2010. Structural geometry of Raplee Ridge monocline and thrust fault imaged using inverse Boundary Element Modeling and ALSM data. *Journal of Structural Geology*, 32 (1), 45-58. doi:10.1016/j.jsg.2009.06.015
- Jabbour, M., Dhont, D., Hervouët, Y., Derooin, J.P., 2012. Geometry and kinematics of fault-propagation folds with variable interlimb angle. *Journal of Structural Geology*, 42, 212-226.
- Jackson, J., 1994. Active tectonics of the Aegean Region. *Annual Review of Earth and Planetary Sciences* 22, 239-271.
- Jackson, J.A., Gagnepain, J., Houseman, G., King, G.C.P., Papadimitriou, P., Soufleris, C., Virieux, J., 1982. Seismicity, normal faulting, and the geomorphological development of the Gulf of Corinth (Greece): the Corinth earthquakes of February and March 1981. *Earth and Planetary Science Letters* 57, 377-397.
- Jamison, W. R., 1987. Geometric analysis of fold development in overthrust terranes. *Journal of Structural Geology*, 9(2), 207-219.
- Jia, D., Li, Y., Lin, A., Wang, M., Chen, W., Wu, X., Ren, Z., Zhao, Y., Luo, L., 2010. Structural model of 2008 Mw 7.9 Wenchuan earthquake in the rejuvenated Longmen Shan thrust belt, China. *Tectonophysics*, 491 (1–4), doi:174-184, 10.1016/j.tecto.2009.08.040.
- Kelley, V. C., 1955. Monoclines of the Colorado Plateau. *Geological Society of America Bulletin*, 66 (7), 789-804. doi: 10.1130/0016-7606(1955)66 [789: MOTCP]2.0.CO;2
- King, G., Ellis, M., 1990. The origin of large local uplift in extensional regions. *Nature* 348, 689-693.
- Kirby, E., Whipple, K.X., 2012. Expression of active tectonics in erosional landscapes. *Journal of Structural Geology*, 44, 54-75, doi: 10.1016/j.jsg.2012.07.009.
- Kooi, H., Beaumont, C., 1994. Escarpment evolution on high-elevation rifted margins: insights derived from a surface processes model that combines diffusion, advection, and reaction. *Journal of Geophysical Research* 99, 12191-12209.
- Koons, P.O., 1989. The topographic evolution of collisional mountain belts: a

References

- numerical look at the Southern Alps, New Zealand. *American Journal of Science* 289, 1041-1069.
- Koons, P. O., Hooks, B. P., Pavlis, T., Upton, P., Barker, A. D., 2010. Three-dimensional mechanics of Yakutat convergence in the southern Alaskan plate corner. *Tectonics*, 29(4).
- Kurfeß, D., 2008. Crustal uplift and subsidence due to the interaction between tectonic and surface processes - an integrated 3D numerical approach for spatial quantification. Doctoral thesis. Geophysikalisches Institut, Universität Karlsruhe. (TH). <http://digbib.ubka.uni-karlsruhe.de/volltexte/1000009996>.
- Kurfeß, D., Heidbach, O., 2009. CASQUS: a new simulation tool for coupled 3d finite element modeling of tectonic and surface processes based on ABAQUS™ and CASCADE. *Computers and Geosciences* 35, 1959-1967, doi: 10.1016/j.cageo.2008.10.019.
- Lee, J., Lister, G.S., 1992. Late Miocene ductile extension and detachment faulting, Mykonos, Greece. *Geology* 20, 121-124.
- Lin, J., Stein, R.S., 2006. Seismic constraints and Coulomb stress changes of a blind thrust fault system, 1: Coalinga and Kettleman Hills, California. U.S. Geological Survey Open-File Report 2006-1149 17 p. [available on the World Wide Web at URL <http://pubs.usgs.gov/of/2006/1149/>].
- Lister, G.S., Banga, G., Feenstra, A., 1984. Metamorphic core complexes of Cordilleran type in the Cyclades, Aegean Sea, Greece. *Geology* 12, 21-25.
- Long, S., McQuarrie, N., Tobgay, T., Grujic, D., 2011. Geometry and crustal shortening of the Himalayan fold-thrust belt, eastern and central Bhutan. *Geological Society of America Bulletin*, 123(7-8), 1427-1447. doi: 10.1130/B30203.1
- Lykousis, V., Sakellariou, D., Moretti, I., Kaberi, H., 2007. Late Quaternary basin evolution of the Gulf of Corinth: sequence stratigraphy, sedimentation, fault-slip and subsidence rates. *Tectonophysics* 440, 29-51, doi: 10.1016/j.tecto.2006.11.007.
- Malavieille, J., Konstantinovskaya, E., 2010. Impact of surface processes on the growth of orogenic wedges: insights from analog models and case studies. *Geotectonics* 44 (6), 541-558.
- Maniatis, G., Hampel, A., 2008. Along-strike variations of the slip direction on normal faults: Insight from three-dimensional finite-element models. *Journal of Structural Geology* 30, 21-28.
- Maniatis, G., Kurfeß, D., Hampel, A., Heidbach, O., 2009. Slip acceleration on normal faults due to erosion and sedimentation - results from a new three-dimensional numerical model coupling tectonics and landscape evolution. *Earth and Planetary Science Letters* 284, 570-582, doi: 10.1016/j.epsl.2009.05.024.
- Mansfield, C.S., Cartwright, J.A., 1996. High resolution fault displacement mapping from three-dimensional seismic data: evidence for dip linkage during fault growth. *Journal of Structural Geology* 18, 249-263.

References

- McKenzie, D.P., 1978. Some remarks on the development of sedimentary basins. *Earth and Planetary Science Letters* 40, 25–32.
- McNeill, L.C., Collier, R.E.L., De Martini, P., Pantosti, D., D'Addezio, G. 2005. Recent history of the Eastern Eliki Fault, Gulf of Corinth: Geomorphology, palaeoseismology and impact on palaeoenvironments. *Geophysical Journal International*, 161, 154–166.
- Michetti, A.M., Brunamonte, F., Serva, L., Vittori, E., 1996. Trench investigations of the 1915 Fucino earthquake fault scarps (Abruzzo, Central Italy): geological evidence of large historical events. *Journal of Geophysical Research* 101, 5921–5936.
- Molnar P, England P., 1990. Late Cenozoic uplift of mountain ranges and global climate change: chicken or egg? *Nature*, 346, 29–34.
- Montgomery, D. R., Brandon, M. T., 2002. Topographic controls on erosion rates in tectonically active mountain ranges. *Earth and Planetary Science Letters*, 201(3), 481-489. doi: 10.1016/S0012-821X(02)00725-2.
- Montone, P., Amato, A., Pondrelli, S., 1999. Active stress map of Italy. *Journal of Geophysical Research* 104, 25,595–25,610.
- Moretti, I., Sakellariou, D., Lykousis, V., Micarelli, L., 2003. The Gulf of Corinth: an active half graben? *Journal of Geodynamics* 36, 323–340.
- Morley, C.K., Wescott, W.A., Stone, D.M., Harper, R.M., Wigger, S.T., Karanja, F.M., 1992. Tectonic evolution of the northern Kenyan Rift. *Journal of the Geological Society* 149, 333-348.
- Mugnier, J.L., Baby, P., Colletta, B., Vinour, P., Bale, P., Leturmy, P., 1997. Thrust geometry controlled by erosion and sedimentation: a view from analogue models. *Geology* 25, 427–30.
- Nicol, A., Walsh, J., Berryman, K., Nodder, S., 2005. Growth of a normal fault by the accumulation of slip over millions of years. *Journal of Structural Geology*, 27, 327-342.
- Nicol, A., Walsh, J.J., Watterson, J., Underhill, J., 1997. Displacement rates of normal faults. *Nature* 390, 157-159.
- Niemi, N.A., Wernicke, B.P., Friedrich, A.M., Simons, M., Bennett, R.A., Davis, J.L., 2004. BARGEN continuous GPS data across the eastern Basin and Range province, and implications for fault system dynamics. *Geophysical Journal International* 159, 842-862.
- O'Sullivan, R. B., 1965. *Geology of the Cedar Mesa-Boundary Butte area, San Juan County, Utah*. US Government Printing Office.
- Palumbo, L., Benedetti, L., Bourles, D., Cinque, A., Finkel, R., 2004. Slip history of the Magnola fault (Apennines, Central Italy) from ^{36}Cl surface exposure dating: evidence for strong earthquakes over the Holocene. *Earth and Planetary Science Letters*, 225(1), 163-176.
- Petit, C., Gunnell, Y, Gonga-Saholiariliva, N., Meyer, B., Seguinot, J., 2009. Faceted spurs at normal fault scarps: Insights from numerical modeling. *Journal of*

References

- Geophysical Research., 114, B05403, doi:10.1029/2008JB005955.
- Pratt, T.L., Shaw, J.H., Dolan, J.F., Christofferson, S.A., Williams, R.A., Odum, J.K., Plesch, A., 2002. Shallow seismic imaging of folds above the Puente Hills blind-thrust fault, Los Angeles, California. *Geophysical research letters*, 29(9), 1304. doi:10.1029/2001GL014313.
- Pysklywec, R.N., 2006. Surface erosion control on the evolution of the deep lithosphere.
- Richardson, R.M., Solomon, S.C., Sleep, N.H., 1979. Tectonic stress in the plates, *Reviews of Geophysical and Space sciences*, 17, 5, 981–1019, doi:10.1029/RG017i005p00981.
- Roberts, G.P., 2006. Multi-seismic cycle velocity and strain fields for an active normal fault system, central Italy. *Earth and Planetary Science Letters*, 251(1), 44–51. doi:10.1016/j.epsl.2005.11.066.
- Roberts, G.P., Michetti, A.M., 2004. Spatial and temporal variations in growth rates along active normal fault systems: an example from The Lazio-Abruzzo Apennines, central Italy. *Journal of Structural Geology*, 26 (2) 339 - 376. 10.1016/S0191-8141(03)00103-2.
- Roberts, G., Michetti, A., Cowie, P., Morewood, N., Papanikolaou, I., 2002. Fault slip-rate variations during crustal-scale strain localisation, central Italy, *Geophysical Research Letters*, 29(8), 1168, doi:10.1029/2001GL013529.
- Rohrman, M., van der Beek, P., 1996. Cenozoic postrift domal uplift of North Atlantic margins: An asthenospheric diapirism model. *Geology* 24, 901-904.
- Sachpazi, M., Clement, C.H., Laigle, M., Hirn, A., Roussos, N., 2003. Rift structure, evolution and earthquakes in Gulf of Corinth, from reflection seismic images. *Earth and Planetary Science Letters* 216, 243-257.
- Sakellariou, D., Lykousis, V., Alexandri, S., Kaberi, H., Rousakis, G., Nomikou, P., Georgiou, P., Ballas, D., 2007. Faulting, seismic–stratigraphic architecture and Late Quaternary evolution of the Gulf of Alkyonides basin–East Gulf of Corinth, Central Greece. *Basin Research* 19, 273–295, doi: 10.1111/j.1365-2117.2007.00322.x.
- Schlische, R.W., Young, S.S., Ackermann, R.V., Gupta, A., 1996. Geometry and scaling relations of a population of very small rift-related normal faults. *Geology* 24, 683–686.
- Shaw J.H., Shearer P.M., 1999. An elusive blind-thrust fault beneath metropolitan Los Angeles. *Science*, 283, 1516-1518, doi:10.1126/science.283.5407.1516.
- Shaw, J.H., Suppe, J., 1994. Active faulting and growth folding in the eastern Santa Barbara Channel, California. *Geological Society of America Bulletin*, 106, 607–626, 0148-0227/96/95JB-03453505.00.
- Shaw, J.H., Suppe, J., 1996. Earthquake hazards of active blind-thrust faults under the central Los Angeles basin, California. *Journal of Geophysical Research*, 101(B4), 8623–8642, doi:10.1029/95JB03453.
- Simpson, G., 2004a. A dynamic model to investigate coupling between erosion,

References

- deposition, and three-dimensional (thin-plate) deformation. *Journal of Geophysical Research*, 109 (F02006), doi:10.1029/2003JF000078.
- Skibeli, M., Barnes, K., Straume, T., Syvertsen, S.E., Shanmugam, G., 1995. A sequence stratigraphic study of Lower Cretaceous deposits of the northernmost North Sea. In: Steel, R.J., et al. (ed.) *Sequence stratigraphy on the Northwest European Margin*. Norwegian Petroleum Society (NPF) Special Publication 5, 389-400.
- Smart, K.J., Ferrill, D.A., Morris, A.P., McGinnis, R.N., 2012. Geomechanical modeling of stress and strain evolution during contractional fault-related folding. *Tectonophysics*, 576–577, 171-196, 10.1016/j.tecto.2012.05.024.
- Stein, R.S., Ekström, G., 1992. Seismicity and geometry of a 110-km-long blind thrust fault 2. Synthesis of the 1982–1985 California Earthquake Sequence. *Journal of Geophysical Research*, 97(B4), 4865–4883, doi:10.1029/91JB02847.
- Suppe, J., 1983. Geometry and kinematics of fault-bend folding. *American Journal of science*, 283(7), 684-721.
- Taylor, B., Weiss, J.R., Goodliffe, A.M., Sachpazi, M., Laigle, M., Hirn, A., 2011. The structures, stratigraphy and evolution of the Gulf of Corinth rift, Greece. *Geophysical Journal International*, 185, 1189–1219, doi:10.1111/j.1365246X.2011.05014.x.
- Tomkin, J.H., 2009. Numerically simulating alpine landscapes: The geomorphologic consequences of incorporating glacial erosion in surface process models, *Geomorphology*, 103, 2, (15) 180-188, ISSN 0169-555X, <http://dx.doi.org/10.1016/j.geomorph.2008.04.021>.
- Trudgill, B.D., 2002. Structural controls on drainage development in the Canyonlands grabens of southeast Utah. *AAPG bulletin*, 86 (6), 1095-1112, doi: 10.1306/61EEDC2E-173E-11D7-8645000102C1865D.
- Turpeinen, H., Maniatis, G., Hampel, A., 2012. Fault slip induced by surface processes after the cessation of regional extension. Submitted to *Geomorphology*.
- Twiss, R.J., Moores, E.M., 1992, *Structural geology*. W. H. Freeman, New York.
- Upton, P., Koons, P.O., Craw, D., Henderson, C.M., Enlow, R., 2009. Along-strike differences in the Southern Alps of New Zealand: Consequences of inherited variation in rheology, *Tectonics*, 28, TC2007, doi:10.1029/2008TC002353.
- Walsh, J.J., Nicol, A., Childs, C., 2002. An alternative model for the growth of faults. *Journal of Structural Geology* 24, 1669-1675.
- Ward, D.J., Anderson, R.S., Haeussler, P.J., 2012. Scaling the Teflon Peaks: Rock type and the generation of extreme relief in the glaciated western Alaska Range. *Journal of Geophysical Research*, 117, F01031, doi:10.1029/2011JF002068.
- Wernicke, B., Friedrich, A.M., Niemi, N.A., Bennett, R.A., Davis, J.L., 2000. Dynamics of Plate Boundary Fault Systems from Basin and Range Geodetic Network (BARGEN) and Geologic Data. *GSA Today* 10, 1-7.
- Wernicke, B., Snow, J.K., 1998. Cenozoic tectonism in the central Basin and Range: Motion of the Sierran-Great Valley Block. *International Geology Review* 40, 403-

References

410.

- Wessel, P., Smith, W.H.F., 1998. New, improved version of the Generic Mapping Tools released. *EOS Transactions AGU* 79, 579.
- Westaway, R., Gawthorpe, R., Tozzi, M., 1989. Seismological and field observations of the 1984 Lazio–Abruzzo earthquakes: implications for the active tectonics of Italy. *Geophysical Journal of the Royal Astronomical Society* 98, 489–514.
- Whipple, K.X., Meade, B.J., 2006. Orogen response to changes in climatic and tectonic forcing. *Earth and Planetary Science Letters*, 243, 1, 218–228.
- Willemsse, E.J., 1997. Segmented normal faults: correspondence between three-dimensional mechanical models and field data. *Journal of Geophysical Research*, 102 (B1), 675–692.
- Willemsse, E.J., Pollard, D.D., Aydin, A., 1996. Three-dimensional analyses of slip distributions on normal fault arrays with consequences for fault scaling. *Journal of Structural Geology*, 18 (2), 295–309.
- Willett, S.D., Slingerland, R., Hovius, N., 2001. Uplift, shortening, and steady state topography in active mountain belts. *American journal of Science*, 301 (4–5), 455–485. doi: 10.2475/ajs.301.4-5.455.
- Wilson, L.F., Pazzaglia, F.J., Anastasio, D.J., 2009. A fluvial record of active fault-propagation folding, Salsomaggiore anticline, northern Apennines, Italy. *Journal of Geophysical Research: Solid Earth* (1978–2012), 114 (B8).
- Wobus, C., Heimsath, A., Whipple, K.X., Hodges, K.V., 2005. Active out-of-sequence thrust faulting in the central Nepalese Himalaya, *Nature*, 434, 1008–1011.
- Xu, X., Wen, X., Yu, G., Chen, G., Klinger, Y., Hubbard, J., Shaw, J., 2009. Coseismic reverse- and oblique-slip surface faulting generated by the 2008 M_w 7.9 Wenchuan earthquake. *China Geology*, 37, 515–518, doi:10.1130/G25446A.1.
- Ziegler, P.A., Dèzes, P., 2005. The Rhine rift system: evolution of the lithosphere. *International Journal of Earth Sciences* 94, 594–614.
- Ziony, J.I., 1966. Analysis of Systematic Jointing in Part of Monument Upwarp, Southeastern Utah. California Univ. (Los Angeles) Ph. D. thesis, 152 p.

Appendix

Curriculum Vitae

Heidi Turpeinen

Geboren am 10.2.1978 in Vantaa, Finnland

- 1985 - 1994 Gesamtschule, Finnland
- 2000 Abitur, Finnland
- 1996 - 2000 Berufsausbildung zur Schneiderin (Finnland)
- 2001 - 2007 Bachelor of Science / Master of Science
Geowissenschaften, Ruhr-Universität Bochum
- 2008 - 2010 Geophysikerin
Alfred-Wegener-Institut für Polar- und Meeresforschung,
Bremerhaven / Antarktis
- 2010 - 2013 Promotion
Geowissenschaften
Gottfried Wilhelm Leibniz Universität Hannover